



Veröffentlichungen der DGK

Ausschuss Geodäsie der Bayerischen Akademie der Wissenschaften

Reihe C

Dissertationen

Heft Nr. 823

Thomas Krawinkel

Improved GNSS Navigation with Chip-scale Atomic Clocks

München 2018

Verlag der Bayerischen Akademie der Wissenschaften

ISSN 0065-5325

ISBN 978-3-7696-5235-2

Diese Arbeit ist gleichzeitig veröffentlicht in:
Wissenschaftliche Arbeiten der Fachrichtung Geodäsie und Geoinformatik der Universität Hannover
ISSN 0174-1454, Nr. 343, Hannover 2018



Veröffentlichungen der DGK

Ausschuss Geodäsie der Bayerischen Akademie der Wissenschaften

Reihe C

Dissertationen

Heft Nr. 823

Improved GNSS Navigation with Chip-scale Atomic Clocks

Von der Fakultät für Bauingenieurwesen und Geodäsie
der Gottfried Wilhelm Leibniz Universität Hannover

zur Erlangung des Grades

Doktor-Ingenieur (Dr.-Ing.)

genehmigte Dissertation

Vorgelegt von

M.Sc. Thomas Krawinkel

Geboren am 14.04.1983 in Bad Driburg

München 2018

Verlag der Bayerischen Akademie der Wissenschaften

ISSN 0065-5325

ISBN 978-3-7696-5235-2

Diese Arbeit ist gleichzeitig veröffentlicht in:
Wissenschaftliche Arbeiten der Fachrichtung Geodäsie und Geoinformatik der Universität Hannover
ISSN 0174-1454, Nr. 343, Hannover 2018

Adresse der DGK:



Ausschuss Geodäsie der Bayerischen Akademie der Wissenschaften (DGK)

Alfons-Goppel-Straße 11 • D – 80 539 München
Telefon +49 – 331 – 288 1685 • Telefax +49 – 331 – 288 1759
E-Mail post@dgk.badw.de • <http://www.dgk.badw.de>

Prüfungskommission:

Vorsitzender: Prof. Dr.-Ing. habil. Jürgen Müller

Referent: Prof. Dr.-Ing. Steffen Schön

Korreferenten: Prof. Dr. phil. nat. Urs Hugentobler (TU München)
Prof. Dr.-Ing. Ingo Neumann

Tag der mündlichen Prüfung: 22.08.2018

© 2018 Bayerische Akademie der Wissenschaften, München

Alle Rechte vorbehalten. Ohne Genehmigung der Herausgeber ist es auch nicht gestattet,
die Veröffentlichung oder Teile daraus auf photomechanischem Wege (Photokopie, Mikrokopie) zu vervielfältigen

Für meine Mutter.

Abstract

The determination of position and time as well as navigation by means of a Global Navigation Satellite System (GNSS) is always based on one-way range measurements between satellites and receiver. Synchronization of their time scales is carried out by introducing so-called *clock biases* with respect to GNSS time. Satellite clock corrections are either provided by the system operator via the navigation message or calculated using clock products of the International GNSS Service. On the receiver side, the clock bias has to be corrected by the user. Due to the poor accuracy and limited long-term stability of the built-in quartz oscillator of a GNSS receiver, the clock bias must be estimated together with the coordinates at each measurement epoch. That is why GNSS-based three-dimensional position determination always requires at least four satellites in view. In addition, high mathematical correlations arise between the up-coordinate and clock bias of the receiver as well as other elevation-dependent error sources. As a consequence, the vertical coordinate can only be determined approximately two to three times less precisely than the horizontal coordinates. If the internal oscillator of the receiver is replaced by a more stable external one, the behavior of the latter can be modeled thanks to its higher frequency stability. An epochwise estimation is not necessary anymore. The physically meaningful prediction of the clock behavior is possible over intervals in which the integrated clock noise is smaller than that of the GNSS observations in use. This approach is referred to as *receiver clock modeling* (RCM). The development of so-called chip-scale atomic clocks (CSACs) makes the use of a highly stable oscillator in kinematic GNSS applications possible. Thus, connecting a CSAC to a GNSS receiver enables physically meaningful RCM in GNSS navigation based on code observations.

In this thesis, the requirements regarding the frequency stability of an oscillator for RCM are investigated by means of two different CSACs. The results of the characterization of their individual frequency stability are discussed in detail, and model parameters for RCM in a Kalman filter are derived thereof. Furthermore, a new real-time applicable modeling approach in a sequential least-squares adjustment is proposed, where the receiver clock biases are modeled by means of a piecewise linear polynomial. The evaluation and validation of this approach are carried out based on a kinematic automotive experiment. In data analysis, GPS and GLONASS L1 CA-code and Doppler observations are used. The impact of receiver clock modeling is assessed by means of typical GNSS performance parameters such as precision, reliability, integrity, continuity and availability of the navigation solution. Improvements of the precision of the vertical coordinate and velocity estimates of ca. 80% and 30%, respectively, are achieved. Internal and external reliability as well as integrity are significantly enhanced, which leads to an overall more robust parameter estimation, especially in regard of statistically reliable outlier detection. It is also shown that using a CSAC in combination with clock modeling enables positioning and navigation with only three satellites in view. This is especially beneficial in areas with high shadowing effects and/or signal attenuation, for example in urban canyons. By implementing the RCM algorithm into a software receiver and using it in a pedestrian experiment, the real-time applicability of the proposed approach is successfully proven. Finally, the benefits of using a CSAC for spoofing detection are demonstrated by means of static experiment.

Keywords: GNSS, Allan variance, clock modeling, software receiver, spoofing

Kurzfassung

Die Bestimmung von Position und Zeit sowie die Navigation mittels eines Globalen Navigationssatellitensystems (GNSS) basiert stets auf Einweglaufzeitmessungen zwischen Satelliten und Empfänger. Die Synchronisierung derer Zeitskalen gelingt jeweils durch Einführen sogenannter *Uhrfehler* gegenüber der übergeordneten GNSS-Zeit. Korrekturwerte für den Satellitenuhrfehler werden vom Systembetreiber per Navigationsnachricht bereitgestellt oder können durch Produkte des International GNSS Service berechnet werden. Die Korrektur des Empfängeruhrfehlers hingegen obliegt dem Nutzer. Aufgrund der geringen Genauigkeit und Langzeitstabilität der in GNSS-Empfängern verbauten Quarzoszillatoren, muss der Uhrfehler zusammen mit den Koordinaten zu jeder Messepoche geschätzt werden. Dies führt dazu, dass zur dreidimensionalen Positionsbestimmung stets mindestens vier Satelliten benötigt werden. Außerdem ergeben sich hohe mathematische Korrelationen zwischen Höhenkoordinate und Empfängeruhrfehler sowie anderen elevationsabhängigen Fehlerquellen. Daraus resultiert unter anderem, dass die Genauigkeit der Höhenkoordinate etwa zwei- bis dreimal schlechter als die der Lagekoordinaten ist. Wird der empfängerinterne Oszillator durch einen stabileren externen ersetzt, kann dessen Verhalten dank der deutlich höheren Frequenzstabilität modelliert werden. Eine epochenweise Schätzung ist nicht mehr notwendig. Die physikalisch sinnvolle Prädiktion des Uhrverhaltens ist über Zeitintervalle möglich, in denen das integrierte Rauschen des Oszillators kleiner als das der verwendeten GNSS-Beobachtungen ist. Dies wird als *Empfängeruhrmodellierung* bezeichnet. Die Entwicklung von sogenannten Chip Scale Atomic Clocks (CSACs) ermöglicht den Einsatz hochstabiler Oszillatoren in kinematischen GNSS-Anwendungen. Das Einspeisen des Frequenzsignals einer CSAC in einen GNSS-Empfänger erlaubt folglich die physikalisch sinnvolle Empfängeruhrmodellierung in der auf Code-Beobachtungen basierenden GNSS-Navigation.

In der vorliegenden Arbeit werden daher die Anforderungen hinsichtlich der Frequenzstabilität eines Oszillators für dessen Einsatz in der Empfängeruhrmodellierung anhand zweier CSACs untersucht. Die Ergebnisse der Charakterisierung der individuellen Frequenzstabilität dieser Oszillatoren werden diskutiert sowie Modellparameter für die Uhrmodellierung in einem Kalman-Filter abgeleitet. Darüber hinaus wird ein neuer Modellierungsansatz in einer echtzeitfähigen sequentiellen Ausgleichung nach der Methode der kleinsten Quadrate vorgeschlagen. Die gewählte Parametrisierung des Empfängeruhrfehlers basiert hierbei auf einem stückweise linearen Polynom. Die Evaluierung und Validierung dieses Ansatzes werden anhand eines kinematischen Fahrzeugexperiments durchgeführt, in dessen Datenauswertung Code- und Doppler-Beobachtungen von GPS und GLONASS verwendet werden. Der Einfluss der Empfängeruhrmodellierung wird an den Qualitätsparametern Präzision, Zuverlässigkeit, Integrität, Kontinuität und Verfügbarkeit bemessen. Hierbei können Verbesserungen der Präzision der vertikalen Empfängerkoordinaten und -geschwindigkeiten von ca. 80 % bzw. 30 % erzielt werden. Innere und äußere Zuverlässigkeit sowie die Integrität werden signifikant verbessert, was wiederum zu einer erhöhten Robustheit des gesamten Ausgleichungsmodells führt, speziell im Hinblick auf eine statistisch belastbarere Ausreißersuche. Abschließend kann gezeigt werden, dass die Verwendung einer CSAC in Verbindung mit Uhrmodellierung die Positionsbestimmung mit nur drei Satelliten erlaubt, was insbesondere in Gebieten mit hoher Signalabschattung und/oder -abschwächung, wie z. B. in Häuserschluchten, von großem Nutzen ist. Die Echtzeitfähigkeit des vorgeschlagenen Ansatzes zur Empfängeruhrmodellierung wird anhand der Implementierung des Algorithmus in einen Software-Empfänger und dessen Einsatz in einem Fußgängerexperiment erfolgreich nachgewiesen. Des Weiteren wird gezeigt, dass eine CSAC die Detektion von Spoofing erheblich verbessern kann.

Schlagwörter: GNSS, Allan-Varianz, Uhrmodellierung, Software-Empfänger, Spoofing

Contents

List of Figures	IX
List of Tables	XI
Acronyms	XIII
1 Introduction	1
1.1 Motivation	1
1.2 State of the Art	2
1.3 Objective and Outline	3
2 Basics	5
2.1 Fundamentals of Global Navigation Satellite Systems	5
2.1.1 A System of Systems	5
2.1.2 Observables	6
2.1.3 Principles of Position Determination	10
2.1.4 International GNSS Service	11
2.1.5 The Role of the Receiver Clock	12
2.2 Parameter Estimation	14
2.2.1 Least-squares Adjustment	15
2.2.2 Kalman Filtering	19
2.3 Frequency Standards and Oscillators	22
2.3.1 General	22
2.3.2 Measures of Frequency Stability	22
2.3.3 Crystal Oscillators	26
2.3.4 Microwave and Optical Atomic Frequency Standards	27
2.3.5 Chip-scale Atomic Clocks	30
3 Receiver Clock Modeling	33
3.1 Concept and Requirements	33
3.2 Frequency Stability of Atomic Clocks	35
3.2.1 Introduction and Background	35
3.2.2 Oscillator Comparisons	36
3.3 Implementations in Data Analysis	46
3.3.1 Linearized Kalman Filter	46
3.3.2 Sequential Least-squares Adjustment	48
4 Application Examples and Case Studies	53
4.1 Observation Modeling in Single Point Positioning	53
4.2 Performance Parameters	56
4.2.1 Precision and Accuracy	56
4.2.2 Reliability	57
4.2.3 Integrity	58
4.2.4 Continuity and Availability	58
4.3 Kinematic Single Point Positioning	59
4.3.1 Automotive Experiment	59
4.3.2 Kalman Filter Results	61
4.3.3 Sequential Least-squares Results	68

4.4	Real-time Applicability	78
4.4.1	Software Receiver	78
4.4.2	Pedestrian Experiment	80
4.5	Spoofing Detection	83
4.5.1	Introduction	83
4.5.2	Meaconing Experiment	84
5	Conclusions	87
5.1	Summary	87
5.2	Outlook	89
	Bibliography	91
	Acknowledgments	99
	Curriculum Vitae	101

List of Figures

2.1	Oscillator phase noise of a third-order GPS L1 phase-locked loop	14
2.2	Different kinds and combinations of accuracy and stability of a frequency signal	22
2.3	Power law noise processes depicted as single-sideband phase noise	24
2.4	Time errors of different power law noise types	25
2.5	Overlapping and non-overlapping sampling of the Allan variance	26
2.6	Power law noise processes depicted by means of various measures	27
2.7	Allan deviations of typical oscillators and frequency standards	28
2.8	Basic design of a chip-scale atomic clock	30
3.1	Allan deviations, time prediction errors of exemplary oscillators	35
3.2	Measurement data of clock comparisons with a sampling interval of one second	38
3.3	Measurement data of clock comparisons with a sampling interval of 100 seconds	39
3.4	Single depictions of individual Allan deviations of devices under test	40
3.5	Joint depiction of aligned individual Allan deviations of devices under test	41
3.6	Time prediction errors of devices under test	42
3.7	Power spectral densities of devices under test	44
3.8	Original overlapping Allan deviations and Allan deviations derived from estimated power spectral density coefficients	45
3.9	Schematic concept of piecewise linear modeling with constrained interval boundaries	49
4.1	Stanford integrity diagram	59
4.2	Test track map of kinematic car experiment	60
4.3	Measurement configuration of kinematic car experiment	60
4.4	Measurement equipment of kinematic car experiment	61
4.5	Position, velocity, time solution of receiver driven by its internal oscillator (Kalman filter)	61
4.6	Position, velocity, time solutions with and w/o clock modeling of receivers connected to Jackson Labs OCXO and Jackson Labs CSAC (Kalman filter)	62
4.7	Position, velocity, time solutions with and w/o clock modeling of receivers connected to SRS PRS10 and Microsemi CSAC (Kalman filter)	63
4.8	GPS and GLONASS L1 C/A-code and Doppler residuals with and w/o clock modeling of receiver connected to Jackson Labs CSAC (Kalman filter)	65
4.9	Dilution of precision values and protections levels with and w/o clock modeling of receiver connected to Jackson Labs CSAC (Kalman filter)	66
4.10	GPS and GLONASS L1 C/A-code and Doppler internal reliability with and w/o clock modeling of receiver connected to Jackson Labs CSAC (Kalman filter)	67
4.11	External reliability of coordinate and velocity estimates with and w/o clock modeling of receiver connected to Jackson Labs CSAC (Kalman filter)	68
4.12	Position, velocity, time solutions with and w/o clock modeling of receivers connected to Jackson Labs OCXO and Jackson Labs CSAC (sequential least-squares adjustment)	69
4.13	Position, velocity, time solutions with and w/o clock modeling of receivers connected to SRS PRS10 and Microsemi CSAC (sequential least-squares adjustment)	70
4.14	Position, velocity, time solution with and w/o clock modeling of receivers connected to Jackson Labs CSAC w/o considering clock frequency drift (sequential least-squares adjustment)	71
4.15	GPS and GLONASS L1 C/A-code and Doppler residuals with and w/o clock modeling of receiver connected to Jackson Labs CSAC (sequential least-squares adjustment)	72

4.16 Dilution of precision values and protections levels with and w/o clock modeling of receiver connected to Jackson Labs CSAC (sequential least-squares adjustment)	73
4.17 GPS and GLONASS L1 C/A-code and Doppler internal reliability with and w/o clock modeling of receiver connected to Jackson Labs CSAC (sequential least-squares adjustment)	74
4.18 External reliability of coordinate and velocity estimates with and w/o clock modeling of receiver connected to Jackson Labs CSAC (sequential least-squares adjustment)	75
4.19 Spatial satellite distribution of navigation with three satellites	76
4.20 Position, velocity, time solution with and w/o clock modeling of receiver connected to Microsemi CSAC with periods of clock coasting (sequential least-squares adjustment)	76
4.21 Position, velocity, time solutions with and w/o clock modeling of receiver connected to Jackson Labs CSAC using different sliding window lengths (sequential least-squares adjustment)	78
4.22 Basic architecture of a software-defined radio	79
4.23 Placement of application programming interfaces within IfEN SX3 software receiver	80
4.24 Main parts of measurement configuration of pedestrian experiment	81
4.25 Trajectory of pedestrian experiment	81
4.26 Position, velocity, time solution with and w/o clock modeling of IfEN SX3 software receiver connected to Microsemi CSAC (sequential least-squares adjustment)	82
4.27 Runtime performance of sequential least-squares clock modeling algorithm in IfEN SX3 software receiver	82
4.28 Measurement configuration of meaconing experiment	84

List of Tables

2.1	Power law noise processes and their relationships with the Allan variance	24
3.1	Parameter values for the determination of time errors of exemplary oscillators	35
3.2	Pre-analysis results of clock comparison measurement data	37
3.3	Parameter values for the determination of time errors of atomic clocks under test	42
3.4	Maximum intervals for physically meaningful receiver clock modeling	43
3.5	Power spectral density coefficients of atomic clocks under test	45
4.1	Impact of receiver clock modeling on the precision of vertical coordinate and velocity estimates of receivers connected to external clocks (Kalman filter)	64
4.2	Impact of receiver clock modeling on minimal detectable biases of GPS and GLONASS L1 C/A-code and Doppler observations of receiver connected to Jackson Labs CSAC (Kalman filter)	66
4.3	Impact of receiver clock modeling on the precision of vertical coordinate and velocity estimates of receivers connected to external clocks (sequential least-squares adjustment)	71
4.4	Impact of receiver clock modeling on minimal detectable biases of GPS and GLONASS L1 C/A-code and Doppler observations of receiver connected to Jackson Labs CSAC (sequential least-squares adjustment)	75
4.5	IfEN SX3 software receiver application programming interfaces	80

Acronyms

AC	Analysis Center
ACC	Analysis Center Coordinator
ACES	Atomic Clock Ensemble in Space
ADEV	Allan Deviation
AHM	Active Hydrogen Maser
AL	Alert Limit
AltBOC	Alternative Binary Offset Carrier
API	Application Programming Interface
AS	Anti-Spoofing
ASIC	Application-Specific Integrated Circuit
AVAR	Allan variance
BDS	BeiDou Navigation Satellite System
C/A	Coarse/Acquisition
C/N_0	Carrier-to-Noise-Density Ratio
CDMA	Code Division Multiple Access
CODE	Center for Orbit Determination in Europe
CPU	Central Processing Unit
Cs	Cesium
CS	Commercial Service
CSAC	Chip-Scale Atomic Clock
DARPA	Defense Advanced Research Projects Agency
DCB	Differential Code Bias
DGNSS	Differential GNSS
DLR	German Aerospace Center
DoD	Department of Defense
DOP	Dilution Of Precision
DUT	Device Under Test
ECEF	Earth-Centered, Earth-Fixed
EKF	Extended Kalman Filter
ESA	European Space Agency
ESOC	European Space Operations Centre
FDMA	Frequency Division Multiple Access
FFM	Flicker Frequency Modulation
FFT	Fast Fourier Transform
FLL	Frequency-Locked Loop
FOC	Full Operational Capability
FPGA	Field-Programmable Gate Array
FPM	Flicker Phase Modulation
GEO	Geostationary Orbit

GLONASS	Globalnaja Nawigazionnaja Sputnikowaja Sistema
GMF	Global Mapping Function
GMM	Gauß-Markov Model
GNSS	Global Navigation Satellite System
GPS	Global Positioning System
GPSDO	GPS Disciplined Oscillator
GPT	Global Pressure and Temperature
GPU	Graphics Processing Unit
IAG	International Association of Geodesy
ICAO	International Civil Aviation Organization
ICD	Interface Control Document
IF	Intermediate frequency
IfE	Institut für Erdmessung
IGS	International GNSS Service
IGSO	Inclined Geosynchronous Orbit
IMU	Inertial Measurement Unit
ISB	Inter-System Bias
ISBM	Inter-System Bias Modeling
ISS	International Space Station
ITRF	International Terrestrial Reference Frame
laser	Light amplification by stimulated emission of radiation
LC	Linear Combination
LES	Linear Equation System
LKF	Linearized Kalman Filter
LN	Low Noise
LSA	Least-Squares Adjustment
MAC	Miniature Atomic Clock
maser	Microwave amplification by stimulated emission of radiation
MDB	Minimal Detectable Bias
MEMS	Microelectromechanical System
MEO	Medium Earth Orbit
MGEX	Multi-GNSS Experiment
NAVIC	Navigation with Indian Constellation
NAVSTAR	Navigational Satellite Timing and Ranging
NIST	National Institute of Standards and Technology
NTRIP	Networked Transport of RTCM via Internet Protocol
OCX	Next Generation Operational Control System
OCXO	Oven Controlled Crystal Oscillator
OMC	Observed Minus Computed
OS	Open Service
PA	Precision Approach
PE	Position Error
PHM	Passive Hydrogen Maser

PID	Proportional-Integral-Derivative
PL	Protection Level
PLL	Phase-Locked Loop
PNT	Positioning, Navigation and Timing
PPP	Precise Point Positioning
PRN	Pseudo-Random Noise
PRS	Public Regulated Service
PSD	Power Spectral Density
PTB	Physikalisch-Technische Bundesanstalt
PVT	Position, Velocity and Time
QZSS	Quasi-Zenith Satellite System
Rb	Rubidium
RCM	Receiver Clock Modeling
RINEX	Receiver Independent Exchange
RMS	Root Mean Square
RTCM	Radio Technical Commission for Maritime Services
RTK	Real-Time Kinematic
RTS	Real-Time Service
RWFM	Random Walk Frequency Modulation
SA	Selective Availability
SBAS	Satellite-Based Augmentation System
SD	Standard Deviation
SDR	Software-Defined Radio
SI	International System of Units
SLSA	Sequential Least-Squares Adjustment
SPP	Single Point Positioning
SRS	Stanford Research Systems
SSB	Single-Sideband Modulation
SSR	State Space Representation
TCXO	Temperature Compensated Crystal Oscillator
TDOP	Time Dilution Of Precision
TEC	Total Electron Content
TGD	Timing Group Delay
UAV	Unmanned Aerial Vehicle
US	United States
USB	Universal Serial Bus
USNO	United States Naval Observatory
VCM	Variance-Covariance Matrix
VLBI	Very-Long-Baseline Interferometry
VMF1	Vienna Mapping Function 1
WFM	White Frequency Modulation
WPM	White Phase Modulation
XO	Crystal Oscillator

1

Introduction

1.1 Motivation

Positioning, navigation and timing (PNT) based on Global Navigation Satellite Systems (GNSSs) play an important role in today's interconnected world. Besides classical geodetic applications, like e.g., cadastre and ordnance survey (*positioning*), also financial transactions and telecommunication networks (*timing*) as well as modern fleet management, machine control and increasingly autonomous/assisted driving (*navigation*) rely on GNSS-based services. Within the scope of this thesis, the navigation category is of particular interest.

Inherently, every GNSS, like e.g., the American Global Positioning System (GPS), the Russian Globalnaja Nawigazionnaja Sputnikowaja Sistema (GLONASS) and the European Galileo system, is based on one-way range measurements. This means, on the one hand, that the signals transmitted by each satellite are time-tagged with respect to its respective timescale. On the other hand, the timestamp of the received signal refers to the timescale of the receiver, thus the latter does not measure true ranges but so-called pseudoranges. Compared to two-way measurement systems such as satellite laser ranging, where transmitter and receiver are one and the same, the unsynchronized timescales of the satellites and a receiver must be linked to each other. Usually, this is achieved by introducing so-called clock biases with respect to a third timescale which is typically the timescale of the system operator.

On the part of the satellites, appropriate corrections for their respective time and frequency offsets are provided by the broadcast navigation message transmitted together with the pseudoranges or by orbit and clock products of the International GNSS Service (IGS). Due to the high frequency stability of the atomic clocks on board the satellites, these corrections can be predicted over a certain period of time for real-time applications. On the contrary, this is not possible on the receiver level because of the low accuracy and limited long-term frequency stability of the built-in quartz oscillator of a conventional GNSS receiver. The main reason for using such an oscillator instead of a more stable one are the significantly lower production costs. Since the accuracy and stability provided by a quartz oscillator are still sufficient at first glance, it is also not necessary to use an atomic clock in a GNSS receiver.

However, the poor frequency stability over intervals greater than one second forces the receiver, in general, to estimate its clock bias at each observation epoch. Thus, the *three*-dimensional problem of position determination becomes a *four*-dimensional one. This fundamentally changes the observation geometry, not only because the receiver has to observe at least four satellites simultaneously instead of three. The increased number of unknown parameters also weakens the observation geometry and thereby the overall estimation process. Theoretical considerations by Kuang et al. (1996) have shown that estimating the receiver clock bias degrades the information in the average direction of the observations – which in an isotropic observation geometry usually coincides with the up-coordinate of the receiver –, whereas without estimation, i.e. in case of true ranging, this direction would be the best observed component. Consequently, the up-coordinate would be estimated more precisely than the horizontal ones. Another drawback to the standard approach are the high mathematical correlations

of 83% to 99% that arise between the estimates of receiver clock bias, station height, tropospheric delay and other elevation-dependent error sources, which decreases their separability from one another (Rothacher and Beutler, 1998; Dach et al., 2003). In addition, the station height is always estimated about two to three times less precisely than the horizontal coordinates.

This situation can be improved significantly if more stable receiver clocks are used and the knowledge about their frequency stability is introduced into the estimation process by applying physically meaningful clock models (Sturza, 1983; Misra, 1996). This approach called receiver clock modeling (RCM) is especially beneficial in kinematic GNSS applications (Weinbach, 2013; Krawinkel and Schön, 2016a). Its main goal is to overcome some of the abovementioned disadvantages of epoch-wise clock bias estimation or at least reduce their negative impact on performance parameters, respectively, such as precision, reliability and availability. Furthermore, it enables positioning and navigation with only three satellites in view, which is also known as *clock coasting* (Sturza, 1983; Knable and Kalafus, 1984; Murphy and Skidmore, 1994). Since the applicability of RCM mainly depends on the frequency stability of the clock in use, in high-precision GNSS applications using carrier phase observations, like e.g., precise point positioning (PPP) (Zumberge et al., 1997), RCM is only feasible in case a highly stable atomic clock like an active hydrogen microwave amplification by stimulated emission of radiation (maser) is connected to the receiver. However, until today, almost all of these oscillators are more or less bulky stationary devices and thereby not useable in true kinematic applications. Thanks to the fact that industrial miniaturization towards microelectromechanical systems (MEMSs) did not stop for atomic clocks, the development of so-called chip-scale atomic clocks (CSACs) in the 2000s and, finally, commercial manufacturing since 2011 open up the possibility of using an atomic clock in kinematic GNSS applications without any severe restrictions regarding power consumption and mobility. Frequency stability and accuracy provided by a CSAC are superior to those of a typical quartz oscillator but worse than those of a hydrogen maser, thus physically meaningful RCM is only possible using code observations not carrier phase observations.

In summary, the various drawbacks of epochwise receiver clock estimation and the availability of market-ready CSACs, on the one hand, and the lack of research contributions in the field of receiver clock modeling, on the other hand, provide an excellent opportunity for a detailed scientific investigation when applying such clocks in GNSS-based applications. This does not only cover positioning and navigation but also extends to the detection of signal interference, for example.

1.2 State of the Art

Scientific publications regarding the idea of using a high-precision frequency standard as an additional sensor in GNSS positioning date back to the beginnings of GPS. Sturza (1983) mathematically investigated the possibility of computing a position solution using only three satellites and a precise clock. Although the need for such an approach was mainly due to reasons of continuity and availability – since, at the time, the planned constellation for GPS consisted of only 18 satellites –, the author evaluates its performance in airborne navigation by means of various dilution of precision (DOP) values taking into account the frequency stability of different precise clocks. Shortly after, Knable and Kalafus (1984) defined certain technical requirements regarding the frequency stability of the clock in order to ensure successful coasting through a typical satellite outage. Again, these considerations aimed at more cost-intensive airborne and satellite applications, like e.g., altimetry, rather than at those using less expensive oscillators in a ground vehicle. In the following two decades, only few contributions on using atomic clocks in GNSS applications or clock modeling in general, respectively, can be found (Wübbena, 1991; Misra, 1996; Lichten and Border, 1987). Since the late 2000s, this field of research got a lot more attention from the scientific community. The reasons for this development can be mainly separated into two categories.

On the one hand, the emergence of the IGS GNSS tracking network (Dow et al., 2009) and the increased use of hydrogen masers therein opened up the possibility for RCM using carrier phase observations. Weinbach and Schön (2011) investigated the technical requirements for physically meaningful RCM and validated their approach by means of pseudo-kinematic PPP using simulated data as well as real data of an IGS station. Herein, the receiver clock bias was modeled as a single quadratic polynomial for an observation period of 24 hours. The same approach was then also applied in kinematic orbit determination and co-seismic displacement monitoring (Weinbach and Schön, 2013; Weinbach and Schön, 2015). In all cases, the root mean square (RMS) of the height coordinates is reduced by approximately 70%, thus significantly improving the overall precision of the position solution. Similar results were obtained within the framework of a project funded by the European Space Agency (ESA) on "Satellite and Station Clock Modelling for GNSS," wherein modeling of receiver *and* satellite clocks was investigated (Wang and Rothacher, 2013; Orliac et al., 2016; Wang et al., 2017; Susnik et al., 2017). Applying this approach in real kinematic PPP is part of future work. Although some passive hydrogen masers are already transportable by design, no practical experience and/or publications are yet available on the matter.

On the other hand, the development of commercially available CSACs led to an increased use of these clocks in kinematic GNSS applications. Krawinkel and Schön (2016a) have shown the benefits of receiver clock modeling in code-based GPS-only navigation when using various miniature atomic clocks in terms of precision and reliability. Also positioning with only three satellites in view is possible. In Ma et al. (2016), the authors present a multi-sensor system they developed consisting of a CSAC, a MEMS inertial measurement unit (IMU) and a GNSS receiver. If three or fewer satellites are visible, the CSAC constrains the error divergence of the IMU by means of *clock coasting*, thus improving the positioning accuracy and overall navigation performance compared to a classical GNSS/IMU integration. A similar approach can be found in Ramlall et al. (2011) where a CSAC is used to enhance navigation in harsh environments like an urban canyon. Furthermore, a first attempt to implement a CSAC *into* a GNSS receiver is described by Ucar et al. (2013). In this experimental setup, a CSAC can optionally drive the tracking channels of the receiver. However, besides noticing and coping with the higher phase noise of the CSAC compared to a crystal oscillator, the authors do not incorporate its superior frequency stability into the signal processing of the receiver. A more CSAC-oriented approach is taken by the Geomatics division at the Centre Tecnològic de Telecomunicacions de Catalunya. In Calero et al. (2016) and Fernández et al. (2017b), the authors are focusing on the determination of the temperature sensitivity of a CSAC in order to use the obtained calibration data to enhance the performance of a receiver when connected to that CSAC. However, the authors do not use any kind of clock modeling. This also applies to the group's most recent publication in which a CSAC was used to augment PPP in various rapid and long-term static and kinematic scenarios (Fernández et al., 2017a). In this paper, certain differences in precision and accuracy between a receiver connected to a CSAC and a receiver driven by its internal oscillator are attributed to the clock in use. In the humble opinion of the author of this thesis, however, these differences are more likely due to the individual characteristics of each receiver, especially since no clock modeling was applied during their analysis.

1.3 Objective and Outline

The main focus of this thesis is on the experimental evaluation of the applicability and potential benefits of the use of CSACs in GNSS navigation based on code and Doppler observations in various kinematic scenarios. The full potential of such clocks is exploited by applying receiver clock modeling (RCM) when computing a multi-GNSS position, velocity and time (PVT) solution. The latter includes the assessment of the impact and limitations of RCM in terms of typical GNSS performance parameters like precision and accuracy. Since quality measures for reliability, integrity, continuity and availability

are often much more important in navigation, for example in aviation and other safety-critical applications, they are of particular interest in this thesis. In addition, the benefits of using a CSAC in spoofing detection are also investigated. According to these objectives, this thesis is structured in the following way.

Chapter 2 gives an overview of methods and models applied in this thesis. First, fundamentals of GNSSs regarding their observables, positioning principles and the role of the receiver clock are discussed. Secondly, least-squares estimation and Kalman filtering are reviewed covering all topics relevant to this work. As part of this, a consistent notation is also introduced. Finally, the functionality of crystal oscillators and atomic clocks, especially CSACs, is described, besides investigating measures of their frequency stability.

Chapter 3 is devoted to the concept and requirements of RCM including the individual characterization of various miniature atomic clocks. Furthermore, the practical implementations of RCM in GNSS data analysis by means of a linearized Kalman filter and the proposal of a new approach in a sequential least-squares adjustment are described.

After discussing the theoretical part of this work, chapter 4 extensively evaluates the proposed methods and models mainly using the example of a kinematic automotive experiment. The benefits of RCM are quantified in terms of various GNSS performance parameters such as precision, reliability and integrity. This also includes the computation of a navigation solution with only three satellites in view. In addition, a software receiver is used to evaluate the proposed approach of sequential RCM in regard of its real-time applicability. Lastly, the positive impact of an CSAC in spoofing detection is investigated.

The thesis closes with a summary of the most important results and findings in chapter 5. An outlook reviewing open questions and defining topics for future investigations is also given.

2

Basics

2.1 Fundamentals of Global Navigation Satellite Systems

2.1.1 A System of Systems

Following a directive of the United States (US) Department of Defense (DoD), initial efforts to establish a satellite navigation system for positioning, navigation and timing started in 1973, which ultimately resulted in the buildup of the first Global Navigation Satellite System called Navigational Satellite Timing and Ranging (NAVSTAR) Global Positioning System (GPS) from the late 1970s on. Since the first generation of satellites (Block I) went out of service in the meantime, the current constellation is a mixture of legacy and modernized satellites of the second generation (Block II). All of them are transmitting satellite-specific pseudo-random noise (PRN) codes on the same carrier frequencies L1 and L2 at 1575.42 MHz and 1227.60 MHz, respectively, which is referred to as code division multiple access (CDMA). Starting with the newest satellites (Block IIF) a third frequency L5 at 1176.45 MHz was added. Therefore, besides the civilian code for coarse/acquisition (C/A) transmitted on L1 and the military precise P(Y)-codes transmitted on both L1 and L2, Block IIR-M and Block IIF satellites are transmitting a second and third civilian signal, L2C and L5, respectively. A third generation of satellites (Block III) is currently in production and the first satellite is planned to be launched in later 2018 (GPS World, 2018). Primarily, GPS was designed for military purposes. Besides transmitting several signals only decipherable by military users referred to as anti-spoofing (AS), until May 2000 so-called selective availability (SA) was activated. This technique adds controlled pseudo-random noise to selected signals, thereby limiting the user position accuracy to about 100 meters (Misra and Enge, 2011). The space segment is being controlled by a network of ground stations: a master control station monitors and sends commands to all satellites by means of eleven ground antennas and 16 monitoring sites (GPS.gov, 2018). Deployment of the GPS III satellites dictates an upgrade of the control segment, thus installation of the next generation operational control system (OCX) is currently under way.

During the 1970s, another military GNSS was initiated. The Russian GLONASS was developed by the Academician M. F. Reshetnev's State Unitary Enterprise of Applied Mechanics and multiple subcontractors. Full operational capability (FOC) was declared in the mid 1990s. Due to funding problems, the number of operational satellites decreased rapidly from 24 to fewer than ten until the early 2000s. Today, the space segment consists of 24 operational satellites arranged in three equally-spaced orbital planes. The majority of these satellites belongs to the second generation of satellites which is usually referred to as GLONASS-M. Similar to GPS, the GLONASS space segment is currently being modernized, i.e. a new generation of satellites (GLONASS-K) with enhanced capabilities and new signals is partly in development, partly already in orbit. All satellites are transmitting the same PRN codes on frequencies specific to each satellite gathered around center frequencies L1 and L2 at 1602 MHz and 1246 MHz, respectively, which is referred to as frequency division multiple access (FDMA). Starting with the new GLONASS-K satellites also CDMA signals are transmitted on a third frequency at 1204.704 MHz for better interoperability with other GNSSs. Future satellites (GLONASS-K2) will also

transmit CDMA signals in the L1 and L2 frequency bands (Karutin, 2016). Besides a low-precision civil code also a military precise code is modulated onto the respective carrier phase signal. In contrast to GPS, these precise codes are not encrypted, but they are not officially released either. The control segment consists of a ground control complex including two system control centers, nine reference stations, six uplink stations and three laser ranging stations (Karutin, 2016).

The first civil GNSS named Galileo was jointly initiated by the European Commission, the European GNSS Agency and ESA in the 1990s. The main reasons to develop its own satellite navigation system were motivated by the continued reliance on third country navigation systems such as GPS and GLONASS, and the lack of sovereignty and security thereof – especially in safety-critical applications (European Commission, 1999). After multiple delays for various reasons and technical difficulties in recent years (Steigenberger and Montenbruck, 2017), as of 14 June 2018, 22 satellites are in orbit, 14 of them set as *usable* (GSC, 2018). By the year 2020, FOC shall be available with 30 operational satellites in space and two ground control centers supported by a worldwide network of monitoring and control stations (Chatre, 2017). The whole system will be managed and operated by a public-private partnership for at least 20 years. In contrast to military systems, Galileo will provide an open service (OS) free of charge, and several fee-based services such as a commercial service (CS) and a public regulated service (PRS). The latter two use a dedicated signal called E6 transmitted at 1278.75 MHz. Besides higher accuracy and authentication, these signals will also offer assured levels of reliability, integrity and availability. Since Galileo was planned to be completely independent from but highly compatible with other systems, its satellites are transmitting signals in the same frequency bands. For example, the OS signals use the same carrier frequencies as GPS L1 and L5, although their signal structure is different and more advanced in terms of accuracy and robustness compared to the legacy GPS signals. The Galileo signal equal to GPS L5 called E5a at 1176.45 MHz is complemented by the E5b signal at 1207.14 MHz, forming the wideband signal E5a+b called alternative binary offset carrier (AltBOC) at 1191.795 MHz which, among others, provides better multipath mitigation (Ries et al., 2003).

Since the market for GNSS applications is growing in recent years, other countries felt compelled to develop their own global and regional space-based navigation systems. The Chinese BeiDou Navigation Satellite System (BDS) is the largest one of them in terms of global availability. Compared to GPS, GLONASS and Galileo, its space segment also consists of inclined geosynchronous orbit (IGSO) and geostationary orbit (GEO) satellites besides medium Earth orbit (MEO) satellites. Since the beginning of the 2000s, BDS developed from an experimental three-satellite constellation to a regional system in the early 2010s and is set to become a fully globally available system by the year 2020. In order to make BDS interoperable with other GNSS, its satellites transmit signals in the same frequency bands. This also applies to regional systems like the Quasi-Zenith Satellite System (QZSS) and Navigation with Indian Constellation (NAVIC) as well as various Satellite-Based Augmentation Systems (SBASs). The proper combination of multi-GNSS data leads to new challenges especially in high-precision applications. In order to cope with these problems, the IGS initiated the Multi-GNSS Experiment (MGEX) in 2011, which is today referred to as *IGS Multi-GNSS Pilot Project*. The three main *biases* when processing multi-GNSS data are differential code biases (DCBs), inter-system biases (ISBs) and carrier phase biases (Montenbruck and Hauschild, 2013; Montenbruck et al., 2017). Since this thesis only uses GPS and GLONASS code (and Doppler) observations, only DCBs and ISBs have to be considered.

2.1.2 Observables

Observation Types

The basic measurement in every GNSS-based PNT application is the difference between the time of transmission marked on the signal with respect to the satellite timescale and the time of reception

at a receiver measured with respect to its own timescale. Multiplying this value by the speed of light yields the *code phase* measurement also referred to as pseudorange. Note that for the remainder of this thesis, this observation type is referred to simply as *code* in order to avoid any confusion with the next observable.

The second major observation type is the *carrier phase* which the navigation message and the PRN codes are modulated onto. It represents the difference between a receiver-generated phase signal and the instantaneous phase of a signal measured by the receiver. Consequently, after acquiring a signal, the receiver does not measure the absolute distance but an arbitrary initial phase offset and then continuously adds carrier cycles to that offset during tracking of the signal. The integer number of full cycles between satellite and receiver called *ambiguities* is unknown and has to be determined by the user. In case signal tracking is interrupted – for example by shadowing effects or ionospheric scintillations –, the receiver has to re-acquire the signal and start tracking again. This discontinuities called *cycle slips* and the aforementioned ambiguities make processing of carrier phase measurements somewhat challenging especially in harsh environments. However, due to its much smaller wavelength, carrier phase observations are much more precise than code observations. As a rule of thumb, the precision can be assessed to one percent of the wavelength of the signal in use.

Furthermore, a GNSS receiver continuously measures the *Doppler shift* of the carrier phase of each satellite in view caused by the permanently on-going relative motion between receiver and satellite. This measurement plays an important role in steering the receiver tracking loops during acquisition and subsequent tracking of satellite signals. When computing a PVT solution, either by the receiver itself or in post-processing mode, the Doppler shift can also be used to determine the instantaneous velocity of the receiver.

The fourth basic observation type is the *signal strength* of a received signal usually given as carrier-to-noise-density ratio (C/N₀). In GNSS analysis, signal strength values are primarily used to assess the quality of the observations and sometimes also to weight them (Brunner et al., 1999). They are also used in investigations related to GNSS multipath and reflectometry (Gleason et al., 2005; Larson et al., 2008).

Since code and Doppler observations are the primary observation types applied throughout this thesis, signal strength and carrier phase observables will not be further considered.

Observation Equations

Note that, in this section, the time arguments of certain equation variables – defined by the signal reception time and propagation time – are neglected for reasons of clarity and simplicity.

The Euclidean distance or geometric range, respectively, between receiver *A* and satellite *i* in an Earth-centered, Earth-fixed (ECEF) coordinate system can be written as

$$\rho_A^i = \sqrt{(X^i - X_A)^2 + (Y^i - Y_A)^2 + (Z^i - Z_A)^2} \quad (2.1)$$

with the respective geocentric Cartesian satellite and receiver coordinates *X*, *Y*, *Z*. Therefore, in an ideal case without any signal delays using true range measurements R_A^i with a given noise level $\epsilon_{A,R}^i$, the observation equation reads

$$R_A^i = \rho_A^i + \epsilon_{A,R}^i. \quad (2.2)$$

Since GNSS are always one-way range systems, so-called satellite and receiver clock biases are introduced into Equation (2.2), thus range measurements become pseudorange measurements. Further-

more, the satellite signal is subject to various errors and delays mainly due to atmospheric effects. This leads to the basic observation equation for pseudorange measurements which enables the estimation of the receiver position together with its clock time offset:

$$P_A^i = \rho_A^i + c \left(\delta t_A - \delta t^i \right) + \delta t_{A,rel}^i + \Delta T_A^i + \Delta I_A^i + \epsilon_{A,P}^i \quad (2.3)$$

with

P_A^i	the pseudorange observation in meters,
c	the speed of light in meters per second,
δt_A	the receiver clock <i>time</i> offset in seconds,
δt^i	the satellite clock <i>time</i> offset in seconds,
$\delta t_{A,rel}^i$	the relativistic <i>time</i> offset correction in meters,
ΔT_A^i	the tropospheric correction in meters,
ΔI_A^i	the ionospheric correction in meters,
$\epsilon_{A,P}^i$	the pseudorange measurement noise in meters.

In order to compute the user velocity, pseudorange rate, carrier phase rate or Doppler shift observations can be used. Since only the latter are considered here, the observation equation reads:

$$\lambda D_A^i = \dot{\rho}_A^i + \delta f_A - \delta f^i + \delta f_{A,rel}^i + \Delta T_A^i + \Delta I_A^i + \epsilon_{A,D}^i \quad (2.4)$$

with

λ	the wavelength of the underlying carrier signal in meters,
D_A^i	the Doppler shift observation in hertz,
δf_A	the receiver clock <i>frequency</i> offset in meters per second,
δf^i	the satellite clock <i>frequency</i> offset in meters per second,
$\delta f_{A,rel}^i$	the relativistic <i>frequency</i> offset correction in meters per second,
ΔT_A^i	the tropospheric rate correction in meters per second,
ΔI_A^i	the ionospheric rate correction in meters per second,
$\epsilon_{A,D}^i$	the Doppler shift measurement noise in meters per second.

The geometric change, i.e. the scalar relative velocity between satellite and receiver is denoted by

$$\dot{\rho}_A^i = \begin{pmatrix} V_X^i - V_{X,A} \\ V_Y^i - V_{Y,A} \\ V_Z^i - V_{Z,A} \end{pmatrix}^T \frac{\begin{pmatrix} X^i - X_A \\ Y^i - Y_A \\ Z^i - Z_A \end{pmatrix}}{\left\| \begin{pmatrix} X^i - X_A \\ Y^i - Y_A \\ Z^i - Z_A \end{pmatrix} \right\|} \quad (2.5)$$

with their respective geocentric Cartesian velocities V_X , V_Y , V_Z .

Besides the main error sources listed above, Equations (2.3) and (2.4) can be extended by further satellite-, propagation- and/or receiver-specific effects, like e.g., signal group delays, which is very useful in case best possible accuracy is aimed for. Corrections for effects at the millimeter or centimeter level such as Earth tide or loading effects, are usually only applied in high-precision applications using carrier phase observations. If observation data of different GNSSs are processed together in PVT estimation, additional parameters have to be included accounting for ISBs.

Combination and Differencing of Observations

In order to eliminate or strongly reduce certain GNSS error sources, two major analysis techniques exist by forming linear combinations (LCs) and differences of the original observations.

Linear combinations of code, carrier phase or, less commonly, Doppler observations can be formed if the respective signals are observed on at least two frequencies. The most used LC is the so-called *ionosphere-free* combination S_{IF} which almost completely eliminates the frequency-dependent ionospheric refraction, one of the most dominant error sources in GNSS signals:

$$S_{IF} = S_u \frac{f_u^2}{f_u^2 - f_v^2} - S_v \frac{f_v^2}{f_u^2 - f_v^2}, \quad (2.6)$$

with the original signals/observations S_u and S_v at frequencies f_u and f_v , respectively. Apart from that, this LC comes with two disadvantages: (a) the integer nature of the original ambiguities is destroyed, (b) the noise of S_{IF} is amplified by a factor of approximately three compared to S_u . Further linear combinations are usually applied in ambiguity resolution and cycle slip fixing, like e.g., the so-called *wide-lane* LC

$$S_{WL} = S_u \frac{f_u}{f_u - f_v} - S_v \frac{f_v}{f_u - f_v}, \quad (2.7)$$

and the *Melbourne-Wübbena* LC (Melbourne, 1985; Wübbena, 1985)

$$S_{MW} = \frac{f_u L_u - f_v L_v}{f_u - f_v} - \frac{f_u P_u + f_v P_v}{f_u + f_v}, \quad (2.8)$$

which is basically the difference between the wide-lane LC applied to code observations P and carrier phase observations L , as well as the *geometry-free* LC

$$S_{GF} = S_u - S_v. \quad (2.9)$$

All linear combinations have their own advantages and disadvantages regarding the respective noise levels, wavelengths and ionospheric sensitivity, for example, so that the appropriate method has to be chosen individually according to the application at hand. Starting with GPS L5 and the advent of new GNSS such as Galileo and BDS transmitting signals on three frequencies, new dual-frequency and also triple-frequency linear combinations are possible (Odijk, 2003).

On the other hand, differencing of original or previously linearly combined observations is applied in order to reduce or eliminate error effects that are similar in the undifferenced signals. Note that since only observations of the same frequency are subtracted from one another, explicit frequency indications are omitted in the following. The first stage of forming observation differences are so-called *single differences*

$$S_A^{ij} = S_A^i - S_A^j, \quad (2.10a)$$

$$S_{AB}^i = S_A^i - S_B^i, \quad (2.10b)$$

either computed between signals of two satellites i and j simultaneously observed by a receiver A or signals of a satellite i simultaneously observed by two receivers A and B . In Equation (2.10a), all receiver-specific propagation-related signal delays are eliminated, i.e. first and foremost, the receiver clock bias but also hardware delays and, in case of carrier phase observations, the corresponding initial phase offset. The between-receiver differences of Equation (2.10b) form so-called *baselines* and do not completely eliminate but greatly reduce the satellite clock bias, since the two receivers only virtually receive the satellite signal at the same time but not w.r.t. superior GNSS time. Moreover, the signal

propagation time from the satellite to each receiver differs slightly because of different spatial distances, which is only critical if long baselines are formed. However, the remaining differential satellite clock bias is deemed to be negligible and therefore considered eliminated. In addition, all atmospheric delays are reduced depending on the distance between the two receivers, i.e. the smaller the distance the greater the reduction. The overall observation noise is increased by a factor of $\sqrt{2}$ compared to the original undifferenced observations. Combining the two methods of forming single differences yields so-called *double differences*:

$$S_{AB}^{ij} = S_{AB}^i - S_{AB}^j. \quad (2.11)$$

This eliminates all satellite and receiver clock biases and hardware delays, respectively. The observation noise of S_{AB}^{ij} is amplified by a factor of two. Double differences are the most frequently used observable in relative and differential GNSS analysis, respectively. By subtracting double differences of two consecutive epochs t_1 and t_2 , the so-called *triple-differences* are formed:

$$\Delta S_{AB}^{ij}(t_1, t_2) = S_{AB}^{ij}(t_1) - S_{AB}^{ij}(t_2). \quad (2.12)$$

This observable is mostly applied to detect between-epoch discontinuities, like e.g., cycle slips in carrier phase observations.

Since neither linear combinations nor differencing of observations is applied in this thesis, the reader is referred to standard literature, like e.g., Kleusberg and Teunissen (1996), for further and more in-depth information.

2.1.3 Principles of Position Determination

The most fundamental method of determining a user location, is the the so-called *navigation solution*. Basic information on how to compute such a solution are described by each GNSS operator in a respective interface control document (ICD), for example given by the GPS Directorate (2013) and European Union (2016). The user algorithm is designated for real-time applications using single-frequency code observations only, thereby providing a position accuracy at the meter level of roughly five to 15 meters depending on user equipment and observation geometry, among others. The coordinates, clock bias and timing group delays (TGDs) of each satellite as well as the ionospheric refraction are corrected by means of data contained in the navigation message. Strictly speaking, satellite orbits and clock biases are predicted by coefficients updated every two hours. The ionospheric correction is computed based on daily parameters provided for the Klobuchar model (Klobuchar, 1987). This means that the receiver only has to apply an appropriate troposphere model – accounting for effects of the neutral atmosphere – in order to compute a position solution in real-time.

In case more accurate autonomous positioning is aimed for, the so-called PPP technique can be applied. This requires at least dual-frequency carrier phase observations in order to eliminate the ionospheric refraction since the Klobuchar model only reduces about 50% of this effect. In addition, a more sophisticated troposphere model, models accounting for Earth tides and loading effects as well as the carrier phase wind-up effect are essential in PPP data analysis. Since the accuracies of orbit and clock corrections provided by the navigation message are at the meter and nanosecond level, respectively, they do not match the accuracy of the carrier phase observations in use. Instead IGS orbit and clock products accurate to a few centimeters and some tens of picoseconds, respectively, must be applied. However, these products exhibit latencies of at least a couple of hours. Real-time corrections for the low-accuracy navigation message data are provided by the IGS real-time service (RTS) broadcasting Radio Technical Commission for Maritime Services (RTCM) state space representation (SSR) messages using the networked transport of RTCM via internet protocol (NTRIP). Nevertheless, for the most part,

the PPP technique is applied in post-processing and not real-time. Furthermore, usually ambiguity resolution is not possible in PPP because the undifferenced carrier phase ambiguities are highly correlated with other parameters, like e.g., the receiver clock bias and tropospheric delay. Therefore, on the one hand, ambiguities must be estimated as real numbers which contradicts their integer nature. On the other hand, PPP suffers from a certain convergence time of roughly five to 15 minutes – depending on the observation situation – until the position solution reaches centimeter-level accuracy. In recent years, different methods of reducing this convergence time for example by means of ambiguity fixing have been developed (Laurichesse et al., 2009).

Both aforementioned methods of position determination are based on undifferenced observations of one receiver. Due to the fact that all error sources must be accounted for by appropriate models or estimated as nuisance parameters together with the receiver coordinate and clock parameters, these approaches are referred to as *parameter estimation*. In contrast, if simultaneous observations of two receivers are subtracted from one another, common error sources are eliminated or at least strongly reduced. Therefore, this approach is called *parameter elimination* (Seeber, 2003). The various levels of observation differencing have already been discussed in section 2.1.2.

In differential position determination, usually double differences are the primary observable. In contrast to absolute positioning, only coordinate differences, so-called baselines, are estimated typically between a *base station* and a *rover*. This leads to the fact that a differential approach always suffers from a datum deficiency, which is typically removed by introducing the known coordinates of the base station into the estimation process. Differential position determination of a rover, in general, has the disadvantage of requiring at least one base station with known coordinates. Similar to absolute positioning, it can be distinguished between techniques using code observations and the ones using (also) carrier phase observations. The first-mentioned is referred to as *differential GNSS (DGNSS)* providing a position accuracy of a few decimeters to meters. The last-mentioned is called *real-time kinematic (RTK)* achieving low centimeter-level accuracy once ambiguity resolution is successful, which is usually the case after a few seconds. This almost instantaneous high accuracy is the biggest advantage compared to PPP. Both DGNSS and RTK operate on the classical base-rover concept described above, i.e. the position of a rover is determined relative to one base station. Further developments of this method have led to so-called *network RTK*. This technique involves a network of base stations in which a rover determines its position. In comparison to classical RTK, this approach not only improves the accuracy of the position solution but also its reliability, integrity and availability since it does not rely on a single base station. The presumably most accurate differential technique is called *relative GNSS*. Similar to network RTK it is based on, at least, one rover whose position is determined in a network of base stations, with the main difference being that it is carried out in post-processing and not real-time. Processing all observation data of a rover in one batch enables the application of high-precision final IGS products as well as more sophisticated models and analysis algorithms, for example in troposphere estimation, cycle slip detection and ambiguity resolution, ultimately leading to higher accuracy and reliability of the position solution.

Although differential techniques greatly simplify parameter estimation, one of the side-effects is that the primary parameter of interest in this thesis, the receiver clock bias, is eliminated from parameter estimation. Therefore, only concepts of *parameter estimation* are considered from this point onward (cf. section 2.2). To be exact, an approach similar to the standard navigation solution using multi-GNSS code and Doppler observations is applied. Further information can be found in chapter 3.

2.1.4 International GNSS Service

Considering the entirety of all GNSS receivers in use, especially in today's countless smart devices, GNSS-based PVT is carried out mostly in real-time using pseudoranges and derived Doppler obser-

ventions. In order to compute the satellite positions, velocities and clock biases, data contained in the broadcast navigation message are applied. Given the low accuracy of these data at the meter-level, high-precision applications such as PPP require the use of more accurate corrections, first and foremost regarding satellite orbits and clock biases. Since 1994, the International GNSS Service (IGS), a service of the International Association of Geodesy (IAG), provides exactly such data mostly by means of so-called *products* (Dow et al., 2009). Based on a voluntary federation of over 200 governmental and non-governmental institutions worldwide, the IGS regularly computes high-precision products including GNSS satellite ephemerides, Earth rotation parameters as well as global ionosphere maps and makes them freely available largely for scientific purposes but also for general public use. All products can be obtained via internet from one of the various IGS data centers.

Subordinated by a governing board, the core of the IGS consists of three so-called coordinators of whom the analysis center coordinator (ACC) is the one supervising a total of currently twelve analysis centers (ACs). In a first step, these ACs compute their own individual solutions mainly for satellite orbit and clock correction products using GNSS observation data of (a subset of) a globally distributed network of more than 400 permanent tracking stations. Note that these observation data are also publicly available free-of-charge. In a second step, some of the AC-specific solutions are combined by the ACC yielding the most precise and accurate IGS products at the respective product level. Basically, three of these levels exist mostly defined based on latency of availability and accuracy. In sequence of increasing accuracy, *ultra-rapid* (observed half), *rapid* and *final* products are available after three to nine hours, 17 to 41 hours and twelve to 18 days, respectively (IGS, 2018). Therefore, IGS products are intended for use in post-processing. Real-time products are available within the scope of the IGS RTS (Caissy et al., 2012). However, this combined solution is only available for GPS to date. If a multi-GNSS or single-system solution using observation data other than GPS shall be computed, the AC-specific individual products have to be used. In any case, the user has to make sure that her/his software specifications (processing settings and models, physical constants, etc.) are consistent with the ones applied by the IGS when generating their respective products.

Besides being a valuable and important contributor to the definition and densification of the International Terrestrial Reference Frame (ITRF) (Altamimi et al., 2016), the IGS realizes and maintains its own reference frame and timescale which almost all of its products refer to. This also enables the computation of a consistent multi-GNSS PVT solution without having to cope with the different single-system coordinate frames and timescales.

2.1.5 The Role of the Receiver Clock

It is the very basic principle of determining a distance by measuring transmission and reception time of a signal and multiplying the difference by the speed of light that makes clocks the heart of every GNSS. Each satellite and receiver works on the basis of a fundamental frequency, like e.g., in case of GPS of 10.23 MHz, whose derivative frequencies drive all of its respective signal processing. As already stated in sections 1.1 and 2.1.2, transmission and reception time of a GNSS signal refer to different timescales. Synchronization is achieved with respect to a third, superior timescale, that is GNSS system time, which in case of GPS is realized by an ensemble solution of all satellite and ground control station clocks. On the one hand, satellites are equipped with highly stable rubidium and cesium clocks, and starting with Galileo also with passive hydrogen masers (PHMs). Besides generating accurate signals, these clocks have to be very stable so that their behavior can be predicted over intervals of at least two hours, which is the validity period of the satellite clock corrections contained inside the broadcast ephemeris. On the other hand, using such an expensive atomic clock in a typical GNSS receiver is simply not physically *feasible* – at least not today. It is also not *necessary* since resynchronization with GNSS time is possible at any time in case a low-precision oscillator has lost synchronization due to

its poorer accuracy and stability. Therefore, only oscillators of manageable size and with low power consumption, but at the same time providing lower accuracy and poorer frequency stability, seem to be suitable for use in a receiver. In order to assess the minimum requirements for such an oscillator, a little excursion into GNSS signal tracking is necessary. The following discussion is based on Ward et al. (2006) to which is referred to for further information.

The major error sources affecting tracking performance of a receiver phase-locked loop (PLL) – and frequency-locked loop (FLL) – can be divided into dynamic stress and phase jitter. The latter is composed of thermal noise and oscillator phase noise caused by vibration and frequency instabilities referred to as Allan deviation (ADEV)-induced. Since dynamic stress and thermal noise mainly depend on PLL order and bandwidth as well as signal strength (C/N_0), the minimum requirements an oscillator has to meet are concerning its vibration sensitivity (g -sensitivity) and short-term frequency stability. As a rule of thumb, the phase jitter must not exceed one-twelfth of the pull-in range of the PLL discriminator. In case of GPS L1 with C/A-code modulation, the corresponding phase jitter threshold for successful and stable tracking amounts to 15° or 7.9 mm, respectively. Furthermore, a third-order PLL is assumed – accounting for velocity, acceleration and jerk stress – for the following considerations.

A typical crystal oscillator (XO), like e.g., a temperature compensated crystal oscillator (TCXO) exhibits a g -sensitivity of about $2 \cdot 10^{-10}$ parts per gravitational acceleration unit g . Assuming equally distributed vibrations from 1 Hz to 1000 Hz, vibration-induced phase jitter σ_v for small, medium and high vibration amplitudes of $0.005 g^2/\text{Hz}$, $0.05 g^2/\text{Hz}$ and $0.5 g^2/\text{Hz}$, respectively, can be computed according to Ward et al. (2006, Equation (5.9)):

$$\sigma_v = \frac{360 f_L S_v}{2\pi} \sqrt{\int_{f_{\min}}^{f_{\max}} \frac{P(f_m)}{f_m^2} df_m}, \quad (2.13)$$

where f_L is the L-band input frequency, S_v the oscillator vibration sensitivity and $P(f_m)$ the power spectral density (PSD) of the random vibration modulation frequency.

Furthermore, the signal of such an oscillator must be stable at least over intervals that are reciprocal to the PLL bandwidth B_n also referred to as gate time. Since a third-order PLL requires a noise bandwidth below 18 Hz, the maximum gate time amounts to approximately 56 ms. By applying Equation (5.13) of Ward et al. (2006) the ADEV-induced phase jitter

$$\theta_{A3} = \frac{160 f_L \sigma_y(\tau)}{B_n} \quad (2.14)$$

is calculated for typical short-term frequency stabilities $\sigma_y(\tau = 56 \text{ms})$ of an XO of $1 \cdot 10^{-9}$, $1 \cdot 10^{-10}$ and $1 \cdot 10^{-11}$, respectively. The results for both phase jitter types of an exemplary third-order PLL tracking GPS L1 are depicted in Figure 2.1.

The largest vibration-induced phase jitter is caused by low-frequency vibrations smaller than 10 Hz, which are typically more unlikely to occur and with smaller amplitudes ($< 0.05 g^2/\text{Hz}$) than high-frequency vibrations. In case of the medium amplitude of $0.05 g^2/\text{Hz}$, these vibrations cause phase jitter not greater than 1.3° , which is well below the 15° threshold (cf. Figure 2.1a). In contrast, ADEV-induced phase jitter is much more pronounced when using an XO with a typical frequency stability in the region of $1 \cdot 10^{-9}$. Figure 2.1b shows that oscillators less stable than that are not suitable for reliable signal tracking of a third-order PLL because even at bandwidths of 17 Hz to 18 Hz the generated phase jitter is just below the overall threshold of 15° . However, such oscillators can be used with increased bandwidth ($> 18 \text{Hz}$) in first-order or second-order filter loops. Furthermore, it is clearly visible that only highly stable oscillators are applicable for narrowband PLL configurations. In conclusion, standard low-price crystal oscillators providing a frequency stability of at least $1 \cdot 10^{-9}$ are suitable to be the reference oscillator inside a GNSS receiver. However, the poor accuracy and the significantly

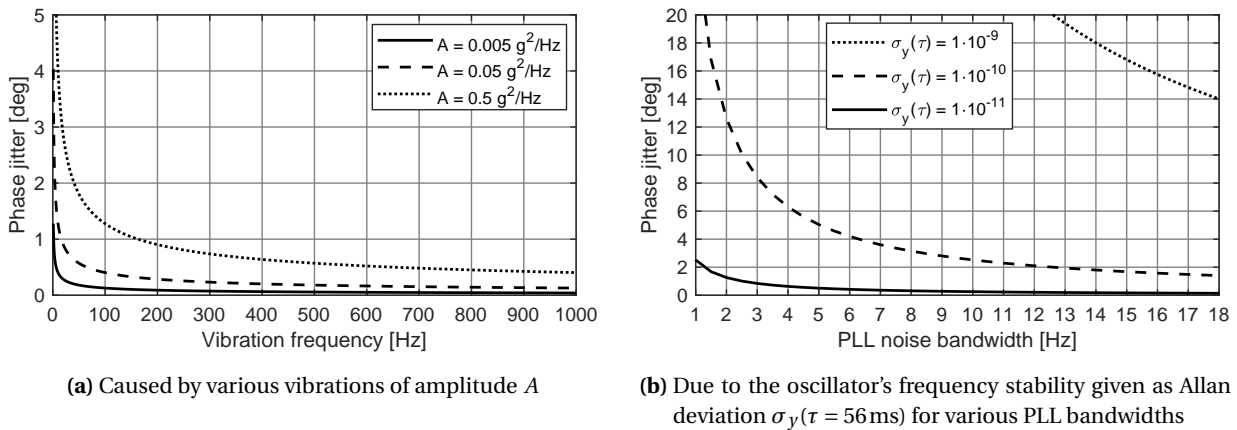


Figure 2.1: Oscillator phase noise of a third-order PLL tracking a GPS L1 carrier phase signal according to Ward et al. (2006). Please note the different scalings of the y-axes.

decreasing frequency stability make the oscillator behavior unpredictable over intervals greater than one second. Therefore, receiver clock corrections must be estimated together with the coordinates (and other parameters if need be) at every measurement epoch.

At this point, it can be stated that there will always be a need to estimate the receiver clock bias from GNSS measurements because synchronization with GNSS system time is simply disproportionately complex and expensive – including the fact that the true clock bias is hardly distinguishable from other instrumental delays of the receiver. As a consequence, since the *absolute* clock bias or initial offset, respectively, always has to be accounted for, only the *relative* changes of the receiver clock, i.e. its frequency stability, is subject to further investigations. If a clock, and thereby its bias, can be predicted over a certain period of time, this behavior can be used advantageously by constraining the temporal variations of the receiver clock bias in a physically meaningful way. This technique is often referred to as *clock aiding* or *clock modeling*. It should presumably decorrelate the receiver clock bias from the vertical coordinate and other parameters as shown by various authors, for example Weinbach (2013), Weinbach and Schön (2013), Krawinkel and Schön (2016c), and Wang (2016). Furthermore, when restoring the initial three-dimensional positioning task, the vertical coordinate should be determined more precisely than the horizontal coordinates (Kuang et al., 1996).

2.2 Parameter Estimation

GNSS data analysis is almost always carried out by means of a least-squares adjustment (LSA) – either in its original form based on measurements only or in association with a dedicated dynamics model, like e.g., in a Kalman filter (Kalman, 1960). The least-squares method can be applied as an epoch-by-epoch algorithm, for example in kinematic data analysis, as well as in batch mode, i.e. processing all observation data of all epochs as a whole, mostly used in static post-processing data analysis. In between these two approaches, sequential LSA operates on an epochwise basis, although it does not estimate a new set of parameters each epoch but updates the parameters estimated an epoch before. Kalman filtering can be regarded as an alteration of the latter method, additionally introducing a dynamics model of the underlying system. Since detailed information and discussions about general and GNSS-related adjustment and filtering theory are provided by a variety of standard textbooks, like e.g., Koch (1999) and Misra and Enge (2011), only a short recapitulation of these topics is presented in the following. More details on the implementation of receiver clock modeling in a linearized Kalman filter (LKF) and sequential least-squares adjustment (SLSA) are described in section 3.3.

2.2.1 Least-squares Adjustment

General Case

Empty and infinite solution sets aside, a linear equation system (LES) consisting of as many observations, i.e. equations, as unknowns, has exactly *one* solution. In case of more observations than unknowns, an LES is called *overdetermined*, ergo there is more than one solution, again neglecting empty and infinite solution sets. In geodesy, overdetermined linear and non-linear equation systems are the usual case, in fact, an overdetermined system is at least desirable, in most cases it is mandatory, for example to enhance the accuracy of the solution and to enable statements about its reliability. Since more than one solution is possible, the optimal one has to be *estimated*. Therefore, the task of parameter estimation is to find the optimal solution of a particular equation system in the sense of the optimization criterion of the applied estimator. In a least-squares adjustment (LSA), this criterion is minimizing the sum of squared observation residuals. Such an approach is most commonly established by means of a Gauß-Markov model (GMM) (Koch, 1999)

$$\tilde{\mathbf{l}} = \mathbf{f}(\tilde{\mathbf{x}}), \quad (2.15)$$

representing the deterministic functional relationship between the *true* values of an $n \times 1$ observation vector $\tilde{\mathbf{l}}$ and a $u \times 1$ unknown parameter vector $\tilde{\mathbf{x}}$. However, these true values are not known. When using *real* observations \mathbf{l} , Equation (2.15) becomes inconsistent. Therefore, so-called residuals \mathbf{v} are introduced for each observation, and $\tilde{\mathbf{x}}$ is replaced by the *unknown* parameters \mathbf{x} :

$$\mathbf{l} + \mathbf{v} = \mathbf{f}(\mathbf{x}). \quad (2.16)$$

In case the relationship described by Equation (2.16) is non-linear, like e.g., in GNSS data analysis using Equation (2.3), Equation (2.16) must be linearized. This requires the presence or knowledge, respectively, of a priori values of the parameters \mathbf{x}_0 , around which linearization then is performed by means of a Taylor series expansion up to the linear segment:

$$\mathbf{l} + \mathbf{v} = \underbrace{\mathbf{f}(\mathbf{x}_0)}_{\mathbf{l}_0} + \underbrace{\frac{\partial \mathbf{f}}{\partial \mathbf{x}} \Big|_{\mathbf{x}=\mathbf{x}_0}}_{\mathbf{A}} \underbrace{(\mathbf{x} - \mathbf{x}_0)}_{\Delta \mathbf{x}}, \quad (2.17)$$

with design matrix \mathbf{A} containing the partial derivatives of the functional model evaluated at the a priori parameters \mathbf{x}_0 , the parameter increments $\Delta \mathbf{x}$ and the a priori observation vector \mathbf{l}_0 . This means that the parameters are not estimated in an absolute sense but as increments to their a priori values:

$$\mathbf{x} = \mathbf{x}_0 + \Delta \mathbf{x}. \quad (2.18)$$

The a priori parameters have to be in the proximity of the true values so that the linearization assumption holds true. Simplifying Equation (2.17) yields the linearized form of the functional model:

$$\Delta \mathbf{l} + \mathbf{v} = \mathbf{A} \Delta \mathbf{x}, \quad (2.19)$$

with the reduced observation vector usually referred to as observed minus computed (OMC) vector:

$$\Delta \mathbf{l} = \mathbf{l} - \mathbf{l}_0. \quad (2.20)$$

Rearranging Equation (2.19) and introducing the least-squares optimum criterion of minimizing the residual sum of squares leads to

$$\mathbf{v}^T \mathbf{v} = (\Delta \mathbf{x}^T \mathbf{A}^T - \Delta \mathbf{l}^T) (\mathbf{A} \Delta \mathbf{x} - \Delta \mathbf{l}). \quad (2.21)$$

The minimum of a function is typically computed by setting its first derivative to zero. Applying this method to Equation (2.21) and solving for the *estimated* parameter increments $\Delta\hat{\mathbf{x}}$ yields (Niemeier, 2008):

$$\Delta\hat{\mathbf{x}} = (\mathbf{A}^T \mathbf{A})^{-1} \mathbf{A}^T \Delta \mathbf{l}. \quad (2.22)$$

In order to account for the random behavior of the observations, a stochastic model is used:

$$\mathbf{C}_{ll} = \sigma_0^2 \mathbf{Q}_{ll} = \sigma_0^2 \mathbf{P}^{-1}, \quad (2.23)$$

comprised of the variance-covariance matrix (VCM) \mathbf{C}_{ll} which is the product of a priori variance factor σ_0^2 and cofactor matrix \mathbf{Q}_{ll} whose inverse is the weight matrix \mathbf{P} . Applying Equation (2.23) to Equation (2.22) yields the standard formula of least-squares parameter estimation:

$$\Delta\hat{\mathbf{x}} = (\mathbf{A}^T \mathbf{P} \mathbf{A})^{-1} \mathbf{A}^T \mathbf{P} \Delta \mathbf{l} = \mathbf{N}^{-1} \mathbf{n}. \quad (2.24)$$

The variances of $\Delta\hat{\mathbf{x}}$ can be computed from the inverse of the normal equation matrix \mathbf{N} called cofactor matrix of the parameters

$$\mathbf{Q}_{\hat{\mathbf{x}}\hat{\mathbf{x}}} = \mathbf{N}^{-1} = (\mathbf{A}^T \mathbf{P} \mathbf{A})^{-1}. \quad (2.25)$$

Furthermore, the estimated residuals and their corresponding cofactor matrix

$$\hat{\mathbf{v}} = \mathbf{A} \Delta\hat{\mathbf{x}} - \Delta \mathbf{l}, \quad (2.26)$$

$$\mathbf{Q}_{\hat{\mathbf{v}}\hat{\mathbf{v}}} = \mathbf{Q}_{ll} - \mathbf{A} \mathbf{Q}_{\hat{\mathbf{x}}\hat{\mathbf{x}}} \mathbf{A}^T \quad (2.27)$$

are an important measure to check if the functional and stochastic model assumptions made are valid and consistent, i.e. if they reflect the actual relationship between observations and parameters. The corresponding one-sided hypothesis test is called *global test* and basically consists of a comparison between the *a priori* variance factor σ_0^2 and (the expectation value of) its *a posteriori* counterpart

$$\hat{\sigma}_0^2 = \frac{\hat{\mathbf{v}}^T \mathbf{P} \hat{\mathbf{v}}}{n - u}. \quad (2.28)$$

Given a certain significance level η – typically in the range of 1% to 5% – and the Fisher distribution, test statistic \mathcal{T} can be computed:

$$\mathcal{T} = \frac{\hat{\sigma}_0^2}{\sigma_0^2} \sim \mathcal{F}_{n-u, \infty, 1-\eta/2}. \quad (2.29)$$

The null and alternative hypothesis H_0 and H_A read

$$H_0: E\{\hat{\sigma}_0^2\} = \sigma_0^2, \quad (2.30)$$

$$H_A: E\{\hat{\sigma}_0^2\} \neq \sigma_0^2. \quad (2.31)$$

If H_0 is rejected based on Equation (2.29), a deficiency in the functional or stochastic model is detected and further investigations are necessary, like e.g., observation outlier detection (Baarda, 1968).

Sequential Approach

In case new observations become available for parameters that have already been estimated according to Equation (2.24), it is computationally inefficient to re-compute the whole LSA again. Therefore, it is

better to simply update the estimated parameters and its VCM. Because observation data accumulates in a sequential manner, this approach is called sequential least-squares adjustment (SLSA). Since the latter will be applied for RCM in chapter 3, its basics are briefly outlined hereinafter.

The original models given by Equations (2.19) and (2.23) are extended based on the additional observations \mathbf{l}_a :

$$\begin{bmatrix} \Delta \mathbf{l} \\ \Delta \mathbf{l}_a \end{bmatrix} + \begin{bmatrix} \mathbf{v} \\ \mathbf{v}_a \end{bmatrix} = \begin{bmatrix} \mathbf{A} \\ \mathbf{A}_a \end{bmatrix} \Delta \mathbf{x}_a, \quad (2.32)$$

$$\mathbf{C}_{ll,a} = \sigma_0^2 \mathbf{Q}_{ll,a} = \sigma_0^2 \mathbf{P}_a^{-1} = \sigma_0^2 \begin{bmatrix} \mathbf{P}^{-1} & \mathbf{0} \\ \mathbf{0} & \mathbf{P}_{aa}^{-1} \end{bmatrix}. \quad (2.33)$$

Considering Equation (2.24), the extended/updated normal equation matrix reads

$$\mathbf{N}_{aa} = \mathbf{N} + \mathbf{A}_a^T \mathbf{P}_{aa} \mathbf{A}_a. \quad (2.34)$$

Hence the updated estimated parameters:

$$\Delta \hat{\mathbf{x}}_a = \mathbf{N}_{aa}^{-1} (\mathbf{n} + \mathbf{A}_a^T \mathbf{P}_{aa} \Delta \mathbf{l}_a), \quad (2.35)$$

$$\mathbf{Q}_{\hat{\mathbf{x}}\hat{\mathbf{x}},a} = \mathbf{N}_{aa}^{-1}. \quad (2.36)$$

Since, in this case, the additional observations are assumed to be uncorrelated with the original ones, their residuals can be computed according to Equations (2.26) and (2.27):

$$\hat{\mathbf{v}}_a = \mathbf{A}_a \Delta \hat{\mathbf{x}}_a - \Delta \mathbf{l}_a, \quad (2.37)$$

$$\mathbf{Q}_{\hat{\mathbf{v}}\hat{\mathbf{v}},a} = \mathbf{Q}_{ll,a} - \mathbf{A}_a \mathbf{Q}_{\hat{\mathbf{x}}\hat{\mathbf{x}},a} \mathbf{A}_a^T. \quad (2.38)$$

Further information, for example on how to compare the updated estimates against the original estimates can be found in Niemeier (2008). Besides a slightly different notation, the mathematics of the global test given by Equations (2.28) to (2.31) stay the same.

Parameter Pre-elimination

One disadvantage of SLSA is the steadily increasing computational demand that accumulates over time with every new epoch of observation data. In the preceding paragraph, it was implicitly assumed that all new observations update all parameters equally. However, if this is not the case, i.e. only a part of the parameters is updated – and also new parameters are estimated –, it is not necessary to keep the parameters that are not of interest anymore. The number of explicitly estimated parameters can be reduced by *parameter pre-elimination*, whereas the impact of the eliminated parameters on the overall solution is preserved implicitly, i.e. the solution is the same as if pre-elimination had not been applied (Heck, 1975; Funcke, 1982). This method is typically used in least-squares batch processing in order to eliminate a potentially large number of epoch-specific parameters that are not of explicit interest for the final solution of the global parameters.

In this thesis, however, parameter pre-elimination will be used to speed-up the proposed approach of sequential RCM described in section 3.3.2, thus also improving its real-time applicability as shown in section 4.4. It is important to note that the understanding or partitioning, respectively, of epoch-specific and global parameters differs from that found in standard textbooks. More details will be outlined in chapter 3. At this point, a slightly different notation is introduced to begin with. Although the following explanations refer to the general case of LSA, they can be transferred to SLSA without any restrictions.

In the case at hand, parameter pre-elimination is achieved by means of *block decomposition*. Therefore, the general case of parameter estimation according to Equation (2.24) can be subdivided into epoch-specific parameters $\hat{\mathbf{x}}_e$ and global parameters $\hat{\mathbf{x}}_g$:

$$\begin{bmatrix} \mathbf{A}_e^T \mathbf{P} \mathbf{A}_e & \mathbf{A}_e^T \mathbf{P} \mathbf{A}_g \\ \mathbf{A}_g^T \mathbf{P} \mathbf{A}_e & \mathbf{A}_g^T \mathbf{P} \mathbf{A}_g \end{bmatrix} \begin{bmatrix} \Delta \hat{\mathbf{x}}_e \\ \Delta \hat{\mathbf{x}}_g \end{bmatrix} = \begin{bmatrix} \mathbf{N}_{ee} & \mathbf{N}_{eg} \\ \mathbf{N}_{ge} & \mathbf{N}_{gg} \end{bmatrix} \begin{bmatrix} \Delta \hat{\mathbf{x}}_e \\ \Delta \hat{\mathbf{x}}_g \end{bmatrix} = \begin{bmatrix} \mathbf{n}_e \\ \mathbf{n}_g \end{bmatrix}. \quad (2.39)$$

According to Funcke (1982) and Niemeier (2008), solving Equation (2.39) for the parameters of interest and their cofactor matrix yields

$$\Delta \hat{\mathbf{x}}_g = \mathbf{Q}_{\hat{\mathbf{x}}_g} (\mathbf{n}_g - \mathbf{N}_{ge} \mathbf{N}_{ee}^{-1} \mathbf{n}_e), \quad (2.40)$$

$$\mathbf{Q}_{\hat{\mathbf{x}}_g} = (\mathbf{N}_{gg} - \mathbf{N}_{ge} \mathbf{N}_{ee}^{-1} \mathbf{N}_{eg})^{-1}, \quad (2.41)$$

and the residuals and their corresponding cofactor matrix read

$$\hat{\mathbf{v}} = \bar{\mathbf{A}} \Delta \hat{\mathbf{x}}_g - (\Delta \mathbf{I} - \mathbf{A}_e \mathbf{N}_{ee}^{-1} \mathbf{n}_e), \quad (2.42)$$

$$\mathbf{Q}_{\hat{\mathbf{v}}} = \bar{\mathbf{A}} \mathbf{Q}_{\hat{\mathbf{x}}_g} \bar{\mathbf{A}}^T + \mathbf{A}_e \mathbf{N}_{ee}^{-1} \mathbf{A}_e^T, \quad (2.43)$$

with the reduced design matrix

$$\bar{\mathbf{A}} = \mathbf{A}_g - \mathbf{A}_e \mathbf{N}_{ee}^{-1} \mathbf{N}_{eg}. \quad (2.44)$$

Since there is no need for back-substitution of the pre-eliminated parameters in this thesis, SLSA will be carried out only by means of Equations (2.40) to (2.44). Furthermore, when applying parameter pre-elimination, the global test of the reduced adjustment model stays unchanged with respect to Equations (2.28) to (2.31).

Constraining of Parameters

Some application cases require the incorporation of a priori knowledge. This may be necessary to compensate certain weaknesses in the observation geometry – which typically leads to a rank deficient LES –, or to account for dependencies between particular parameters. The parameters or their differences, respectively, are constrained to their known a priori values with a given uncertainty. Here, it can be distinguished between absolute and relative constraining, depending on whether a parameter is constrained individually or relative to at least one other parameter, respectively. One way to introduce such information into parameter estimation according to Equations (2.19) and (2.23) is by extending the adjustment model by *pseudo-observations* and their stochastics, whereas the latter determines how tightly or loosely, respectively, the parameters are constrained. In order to account for the usually smooth, only slowly changing behavior of an atomic clock, relative constraining is applied in RCM. More detailed information about the exact implementations can be found in section 3.3.2 and section 4.3. At this point, only the underlying model extension is briefly addressed.

Similar to the handling of additional observations in sequential LSA, pseudo-observations are introduced into the functional and stochastic models by extending Equations (2.19) and (2.23):

$$\begin{bmatrix} \Delta \mathbf{I} \\ \Delta \mathbf{I}_c \end{bmatrix} + \begin{bmatrix} \mathbf{v} \\ \mathbf{v}_c \end{bmatrix} = \begin{bmatrix} \mathbf{A} \\ \mathbf{A}_c \end{bmatrix} \Delta \mathbf{x}_c, \quad (2.45)$$

$$\mathbf{C}_{ll,c} = \sigma_0^2 \mathbf{Q}_{ll,c} = \sigma_0^2 \begin{bmatrix} \mathbf{Q}_{ll} & \mathbf{0} \\ \mathbf{0} & \mathbf{Q}_{cc} \end{bmatrix}, \quad (2.46)$$

with cofactor matrix \mathbf{Q}_{cc} and VCM \mathbf{C}_{cc} of the pseudo-observations \mathbf{I}_c .

A single parameter x_i can be constrained to pseudo-observation $l_{c,k}$ by means of its variance $\sigma_{c,k}^2$:

$$l_{c,k} + v_{c,k} = x_i, \quad (2.47a)$$

$$\mathbf{Q}_{cc,k} = \sigma_{c,k}^2. \quad (2.47b)$$

In order to constrain x_i with respect to another parameter x_j , relative constraining is applied:

$$l_{c,k} + v_{c,k} = x_i - x_j, \quad (2.48a)$$

$$\mathbf{Q}_{cc,k} = \sigma_{c,k}^2. \quad (2.48b)$$

2.2.2 Kalman Filtering

Background

When using one of the least-squares approaches presented in section 2.2.1, the resulting estimates are computed solely based on observations. Besides applying certain constraints, it is not possible to introduce any sophisticated information about the underlying system, like e.g., state and temporal variations of a vehicle, i.e. its dynamics, into the estimation process. Following standard textbooks like Gelb et al. (1974) and Farrell (2008), such a system is represented by a mathematical-physical model based on the inhomogeneous *linear* differential equation

$$\dot{\mathbf{x}}(t) = \mathbf{F}(t)\mathbf{x}(t) + \mathbf{L}(t)\mathbf{u}(t) + \mathbf{G}(t)\mathbf{w}(t) \quad (2.49)$$

with state vector \mathbf{x} , control-input vector \mathbf{u} , process noise vector \mathbf{w} , dynamics matrix \mathbf{F} , control-input matrix \mathbf{L} and noise distribution matrix \mathbf{G} at time instant t . Since the deterministic control-input components are unknown in the majority of cases, which also applies to this thesis, they can be safely neglected from this point on:

$$\dot{\mathbf{x}}(t) = \mathbf{F}(t)\mathbf{x}(t) + \mathbf{G}(t)\mathbf{w}(t). \quad (2.50)$$

Following the superposition principle of linear differential equations, an inhomogeneous differential equation can be solved by adding the general solution of the homogeneous part and one particular solution of the inhomogeneous part. Solving the first homogeneous part of Equation (2.50) by means of a Taylor series expansion up to the linear segment and the matrix exponential yields

$$\mathbf{x}(t) = \mathbf{\Phi}(t, t_0)\mathbf{x}(t_0) \quad (2.51)$$

with the state transition matrix $\mathbf{\Phi}(t, t_0)$. The particular solution of the inhomogeneous part reads

$$\mathbf{x}(t) = \int_{t_0}^t \mathbf{\Phi}(t, t')\mathbf{G}(t')\mathbf{w}(t') dt'. \quad (2.52)$$

Hence, the solution of Equation (2.50) results in

$$\mathbf{x}(t) = \mathbf{\Phi}(t, t_0)\mathbf{x}(t_0) + \int_{t_0}^t \mathbf{\Phi}(t, t')\mathbf{G}(t')\mathbf{w}(t') dt'. \quad (2.53)$$

Since input values for such a system model are usually available at discrete time instants and not in a continuous manner, Equation (2.53) has to be transferred from continuous time to discrete time at epoch k , yielding the so-called *system equation*:

$$\mathbf{x}_k = \mathbf{\Phi}_{k,k-1}\mathbf{x}_{k-1} + \boldsymbol{\omega}_k, \quad (2.54)$$

where process noise ω_k follows a multivariate normal distribution with zero mean:

$$\omega_k = \mathbf{G}_k \mathbf{w}_k \sim \mathcal{N}(\mathbf{0}, \mathbf{Q}_{\omega\omega, k}). \quad (2.55)$$

Up to this point, the system state is solely described by a dynamic model. Therefore, the state is observed – preferably on a regular basis – by external measurements \mathbf{I}_k . In analogy to the linear least-squares functional model given in Equation (2.16), the corresponding *measurement equation* reads

$$\mathbf{I}_k = \mathbf{A}_k \mathbf{x}_k + \mathbf{v}_k. \quad (2.56)$$

Both Equations (2.54) and (2.56) form the basis of the so-called Kalman filter as originally proposed by Kalman (1960). This filter is an optimal estimator in the sense that it optimally combines the time propagated state of a linear system from a previous time instant to the current one and the measurement at the current time instant, depending on the stochastic behavior of the prior system state and the current measurement (Farrell, 2008).

Similar to pure least-squares parameter estimation, this method does only apply for linear systems. In most cases, however, the underlying system is of non-linear nature, either in regard of the system equation or the measurement equation – or even both. In the thesis at hand, only the measurement equation is non-linear because of the GNSS observation equations Equations (2.3) and (2.4). Apart from that, such a non-linear system has to be linearized, again, typically by means of a Taylor series expansion. In contrast to pure least-squares methods, there are two options of *where* to linearize each of these specific equations (Maybeck, 1982):

- *Linearized Kalman filter (LKF)*: Linearization is carried out around a nominal trajectory, like e.g., given approximate coordinates and velocities. This approach is computationally beneficial since all data related to the nominal trajectory such as measurement corrections or design and gain matrices can be computed beforehand. This, however, requires the presence of *good* a priori information. Moreover, in case the nominal trajectory and the actual state estimates differ (over time), the linearization assumption may not be valid anymore.
- *Extended Kalman filter (EKF)*: If there is no prior knowledge available, linearization is computed around the latest state estimates. Although this approach is computationally more demanding, it is better suited for real-time applications where the nominal trajectory is typically not known. However, the complete absence of a priori information leads to a certain convergence time of the filter solution after initialization first.

Therefore, it depends on the application at hand and its requirements which type of linearized filter to use. From a mathematical standpoint, both filters are using the same formulae given below. Due to the fact that, actually, the difference of the state with respect to the point of linearization is estimated and not the state itself, such a filter is also called *error state estimator*.

Computation Procedure

The recursive design of a Kalman filter is subdivided into three steps. Aside from cascaded filters using different update intervals of the state vector and its cofactor matrix, these steps are typically performed every epoch k . Applying a Kalman filter in non-linear GNSS-based PVT estimation, requires the use of an EKF or LKF. Therefore, similar to least-squares estimation, not the total state $\hat{\mathbf{x}}_k$ but only the error state $\Delta \hat{\mathbf{x}}_k$ of the system is estimated. In this case, at the end of each recursion, the total state can be computed as

$$\hat{\mathbf{x}}_k = \bar{\mathbf{x}}_k + \Delta \hat{\mathbf{x}}_k, \quad (2.57)$$

where vector $\bar{\mathbf{x}}_k$ contains either the current nominal state (LKF) or the latest state estimates (EKF), respectively. At initialization, the predicted *a priori* error state $\Delta\hat{\mathbf{x}}_0^-$ is set to zero:

$$\Delta\hat{\mathbf{x}}_0^- = \mathbf{0}, \quad (2.58)$$

$$\mathbf{Q}_{\hat{x}\hat{x},0}^- = \mathbf{Q}_{xx,0}. \quad (2.59)$$

The corresponding initial cofactor matrix $\mathbf{Q}_{xx,0}$ has to account for the relatively high uncertainty of $\Delta\hat{\mathbf{x}}_0^-$. This is especially critical in case of an EKF where the initial state vector $\bar{\mathbf{x}}_0$, around which the whole system is linearized, is unknown, therefore possibly being set to zero.

Apart from initialization, in the first of three steps per recursion, the a priori error state $\Delta\hat{\mathbf{x}}_0^-$ and its cofactor matrix $\mathbf{Q}_{\hat{x}\hat{x},0}^-$ are being *filtered* by means of the so-called *measurement update*:

$$\Delta\hat{\mathbf{x}}_k^+ = \Delta\hat{\mathbf{x}}_k^- + \mathbf{K}_k (\Delta\mathbf{l}_k - \mathbf{A}_k \Delta\hat{\mathbf{x}}_k^-), \quad (2.60)$$

$$\mathbf{Q}_{\hat{x}\hat{x},k}^+ = (\mathbf{I} - \mathbf{K}_k \mathbf{A}_k) \mathbf{Q}_{\hat{x}\hat{x},k}^-, \quad (2.61)$$

with updated error state $\Delta\hat{\mathbf{x}}_k^+$ and its cofactor matrix $\mathbf{Q}_{\hat{x}\hat{x},k}^+$. Design matrix \mathbf{A}_k and OMC vector $\Delta\mathbf{l}_k$ originate from the LSA, cf. Equations (2.17) and (2.20), respectively. The Kalman gain matrix

$$\mathbf{K}_k = \mathbf{Q}_{\hat{x}\hat{x},k}^- \mathbf{A}_k^T (\mathbf{Q}_{ll,k} + \mathbf{A}_k \mathbf{Q}_{\hat{x}\hat{x},k}^- \mathbf{A}_k^T)^{-1} \quad (2.62)$$

is further computed by means of the measurement noise $\mathbf{Q}_{ll,k}$. This matrix weights the information in the measurements against the a priori error state, which is also referred to as *filtering* of the measurements. The smaller the Kalman gain, the smaller the contribution of the measurement to the updated error state. Note that, because $\mathbf{Q}_{\hat{x}\hat{x},k}^+$ in Equation (2.61) is prone to non-symmetry caused by numerical instabilities, like e.g., round-off errors, it is often computed using the *Joseph form* to enforce symmetry of the matrix (Bucy and Joseph, 2005):

$$\mathbf{Q}_{\hat{x}\hat{x},k}^+ = (\mathbf{I} - \mathbf{K}_k \mathbf{A}_k) \mathbf{Q}_{\hat{x}\hat{x},k}^- (\mathbf{I} - \mathbf{K}_k \mathbf{A}_k)^T + \mathbf{K}_k \mathbf{Q}_{ll,k} \mathbf{K}_k^T. \quad (2.63)$$

In a second step, complementary to the least-squares residuals given in Equations (2.26) and (2.27), the so-called observation *innovations* and their cofactor matrix are computed:

$$\mathbf{d}_k = \Delta\mathbf{l}_k - \mathbf{A}_k \Delta\hat{\mathbf{x}}_k^-, \quad (2.64)$$

$$\mathbf{Q}_{dd,k} = \mathbf{Q}_{ll,k} - \mathbf{A}_k \mathbf{Q}_{\hat{x}\hat{x},k}^- \mathbf{A}_k^T. \quad (2.65)$$

Whether the measurement is consistent with the system model, is tested in analogy to the least-squares global test given by Equations (2.28) to (2.31) with

$$\hat{\sigma}_0^2 = \frac{\mathbf{d}_k^T \mathbf{Q}_{dd,k}^{-1} \mathbf{d}_k}{\zeta} \quad (2.66)$$

according to the degrees of freedom ζ of the filter solution. Again, if the test fails, i.e. parts of the measurements are inconsistent with the system model, further action has to be taken in order to identify the cause of the failed test (Salzmann, 1993; Teunissen, 1997).

In a third step called *prediction*, the updated error state is propagated through time:

$$\Delta\hat{\mathbf{x}}_{k+1}^- = \Phi_{k,k+1} \Delta\hat{\mathbf{x}}_k^+ \quad (2.67)$$

$$\mathbf{Q}_{\hat{x}\hat{x},k+1}^- = \Phi_{k,k+1} \mathbf{Q}_{\hat{x}\hat{x},k}^+ \Phi_{k,k+1}^T + \mathbf{Q}_{\omega\omega,k}, \quad (2.68)$$

with state transition matrix $\Phi_{k,k+1}$ and process noise matrix $\mathbf{Q}_{\omega\omega,k}$, yielding the new a priori error state and its cofactor matrix for recursion in the next epoch. The crucial point of prediction is the process noise which represents the inherent noise of the system model. If it is small compared to the measurement noise, the updated error state is dominated by the system model and vice versa. Therefore, in this thesis, GNSS receiver clock modeling in a Kalman filter is carried out by applying an appropriate model for the clock process noise taking into account the stochastic behavior of the oscillator in use. More details on the exact implementations are outlined in section 3.3.1.

2.3 Frequency Standards and Oscillators

2.3.1 General

Because frequency is the most accurate measurement quantity of all, a clock is always derived from a frequency source. A device that generates a continuous frequency signal is called an oscillator. Only if its frequency has been measured by comparison with a source derived from a primary standard (ITU, 1997), it can be called a *frequency standard* (Riehle, 2004). Apart from that, the following descriptions and discussions are based on further standard literature like Allan (1987) and Barnes et al. (1971), which are referred to for extended information and derivations.

The accuracy of an oscillator denotes how much its actual frequency deviates from the nominal value. The corresponding measure is usually given with respect to that nominal frequency. Stability, on the other hand, describes how closely the oscillator frequency stays at a certain frequency over time, thereby stability is solely driven by the random/stochastic behavior of the frequency signal. Short-term stability is often given as *phase noise*, whereas mid-term and long-term stability is typically characterized by means of the so-called *Allan deviation (ADEV)*. A comprehensive overview about the different meanings of accuracy and stability is shown in Figure 2.2. Accuracy and stability of an oscillator can only be determined by comparing it to a frequency reference of at least one order of magnitude higher accuracy and stability, respectively. This reference can either be an external frequency source like a frequency standard or the internal oscillator of a frequency counter or phase comparator. Since frequency stability is the prime measure of interest in this thesis, only its corresponding measures are briefly discussed in the following.

2.3.2 Measures of Frequency Stability

Signal Description

The output signal of an ideal harmonic sinusoidal oscillator at a certain point in time t reads

$$x_0(t) = A_0 \sin(2\pi\nu_0 t), \quad (2.69)$$

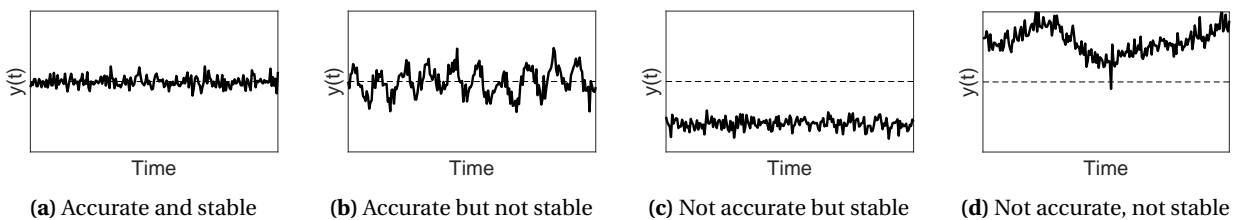


Figure 2.2: Different kinds and combinations of accuracy and stability of a frequency signal $y(t)$ relative to its nominal frequency (dashed line)

with error-free and time-invariant nominal amplitude A_0 and frequency ν_0 . However, even the most advanced oscillators are subject to deviations from these constant values:

$$x(t) = (A_0 + \epsilon(t)) \sin(2\pi\nu_0 t + \phi(t)). \quad (2.70)$$

Since amplitude fluctuations $\epsilon(t)$ are assumed to be very small, they can be safely neglected from this point on. The phase fluctuations $\phi(t)$, on the other hand, lead to deviations of the instantaneous frequency $\nu(t)$ from its nominal value described as

$$\nu(t) = \nu_0 + \frac{\dot{\phi}(t)}{2\pi} = \nu_0 + \frac{1}{2\pi} \frac{\partial\phi(t)}{\partial t}, \quad (2.71)$$

with instantaneous phase time derivative $\dot{\phi}(t)$. In order to enable comparisons between oscillators independent of their nominal frequency, the instantaneous fractional frequency deviations

$$y(t) = \frac{\dot{\phi}(t)}{2\pi\nu_0} = \frac{\partial x(t)}{\partial t} = \dot{x}(t) \quad (2.72)$$

are the basis for determining the stability of an oscillator.

The corresponding time errors $x(t)$ can be computed either by integrating fractional frequency deviations or directly from phase fluctuations:

$$x(t) = \int_{t_0}^t y(t') dt' = \frac{\phi(t)}{2\pi\nu_0}. \quad (2.73)$$

Frequency Domain

The short-term frequency stability of an oscillator is most commonly described by the single-sideband modulation (SSB) phase noise $\mathcal{L}(f)$ (Riley, 2008), which is the logarithmic representation of the PSD of the phase fluctuations $S_\phi(f)$:

$$\mathcal{L}(f) = 10 \log \left(\frac{1}{2} S_\phi(f) \right), \quad (2.74)$$

with the Fourier frequency f . Phase noise describes the signal-to-carrier power ratio at a particular offset frequency from the carrier. By plotting phase noise along a logarithmic scale, its power law noise processes result in distinct slopes each as depicted in Figure 2.3. The PSD of instantaneous fractional frequency deviations $S_y(f)$ is defined as the time derivative of $S_\phi(f)$:

$$S_y(f) = \left(\frac{f}{\nu_0} \right)^2 S_\phi(f). \quad (2.75)$$

It can further be described or reasonably approximated, respectively, by the superposition of various independent power law noise processes (Barnes et al., 1971; Rutman, 1978):

$$S_y(f) = \sum_{\alpha=-2}^2 h_\alpha f^\alpha, \quad (2.76)$$

with intensity coefficient h_α of the specific noise types denoted by power law exponent α .

The five most common used power law noise processes – white phase modulation (WPM), flicker phase modulation (FPM), white frequency modulation (WFM), flicker frequency modulation (FFM), random walk frequency modulation (RWFm) – are summarized in Table 2.1. Furthermore, the relationships between the PSD h_α -coefficients and the corresponding ADEV are listed here as given by

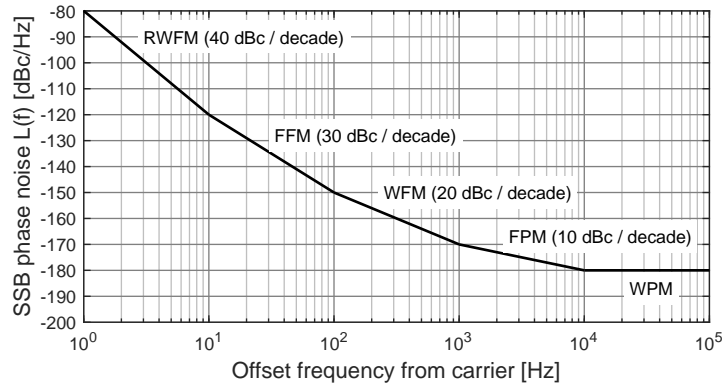


Figure 2.3: Power law noise processes depicted as single-sideband (SSB) phase noise: white phase modulation (WPM), flicker phase modulation (FPM), white frequency modulation (WFM), flicker frequency modulation (FFM), random walk frequency modulation (RWFM)

Barnes et al. (1971). These formulae are used to convert between both types of stability measures from the frequency domain to time domain and vice versa. In this thesis, they are applied within the scope of individual clock characterizations in section 3.2.2. Additionally, the characteristic slopes of these five power law noise processes in terms of the standard ADEV and the modified ADEV in a double-logarithmic representation are also given in Table 2.1. More information on this topic follows in the next paragraph on time-domain stability measures. The corresponding time errors caused by the five noise processes are shown exemplarily in Figure 2.4.

In this thesis, the PSD coefficients h_α will be used for receiver clock modeling in an LKF in order to introduce the individual frequency stabilities of various oscillators into the estimation process. For more details it is referred to section 3.3.1.

Time Domain

Frequency stability in the time domain can be more intuitive, especially if its long-term behavior, i.e. longer than a couple of seconds, is of interest. The standard measure for this is the Allan variance (AVAR) (Allan, 1987), or its square root the Allan deviation (ADEV), respectively, and a variety of other versions derived from it. Its basis is a sequence of fractional frequency deviations $y(t)$ which, in reality,

Table 2.1: Power law noise processes and their relationships with Allan variance (AVAR) as a function of averaging time τ and under the assumption that the high-frequency cutoff $f_h \gg (2\pi\tau)^{-1}$, as well as the respective slopes of standard Allan deviation (ADEV) and modified Allan deviation (M-ADEV) in a double-logarithmic plot

Noise process	Power law exponent α	AVAR	ADEV slope	M-ADEV slope
White phase modulation (WPM)	2	$\frac{3f_h}{4\pi^2\tau^2} h_2$	-1	-3/2
Flicker phase modulation (FPM)	1	$\frac{3\ln(2\pi f_h\tau)}{4\pi^2\tau^2} h_1$	-1	-1
White frequency modulation (WFM)	0	$\frac{1}{2\tau} h_0$	-1/2	-1/2
Flicker frequency modulation (FFM)	-1	$2\ln(2)h_{-1}$	0	0
Random walk frequency modulation (RWFM)	-2	$\frac{2\pi^2\tau}{3} h_{-2}$	1/2	1/2

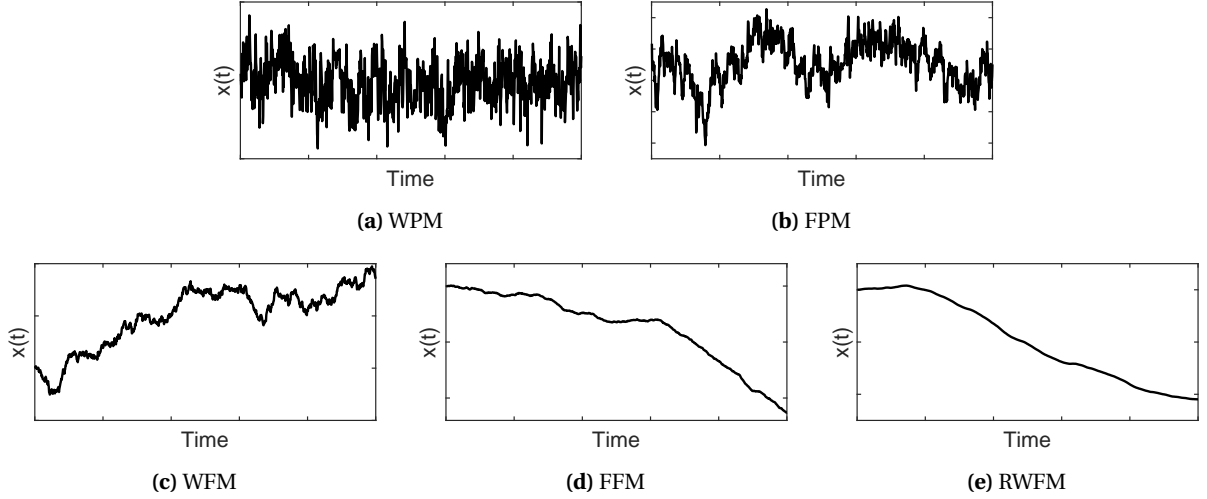


Figure 2.4: Time errors $x(t)$ of different power law noise types: white phase modulation (WPM), flicker phase modulation (FPM), white frequency modulation (WFM), flicker frequency modulation (FFM), random walk frequency modulation (RWFM)

is averaged over a certain period called *averaging time* τ either by means of a frequency counter or derived from discrete adjacent time error measurements x_i of a phase comparator:

$$\bar{y}_i = \frac{1}{\tau} \int_{t_i}^{t_i+\tau} y(t) dt = \frac{x_{i+1} - x_i}{\tau}. \quad (2.77)$$

The underlying stochastic process of finite sequence \bar{y} cannot be described by typical statistical measures like mean value and standard deviation, because the samples y_i are correlated in time and therefore do not represent a stationary process. In fact, estimates for standard statistical measures will not converge over time in that case. Consequently, time-domain frequency stability is calculated from a finite number of samples N of \bar{y}_i , averaging time τ and the time between consecutive samples τ' which may differ from τ (Riehle, 2004). The result is called N -sample variance:

$$\sigma^2(N, \tau', \tau) = \frac{1}{N-1} \sum_{i=1}^N \left(\bar{y}_i - \frac{1}{N} \sum_{j=1}^N \bar{y}_j \right)^2. \quad (2.78)$$

As recommended by Barnes et al. (1971), using two samples ($N = 2$) and assuming no dead time between the measurements ($\tau' - \tau = 0$) yields the *standard Allan variance* $\sigma_y^2(2, \tau, \tau)$, usually given by short notation $\sigma_y^2(\tau)$:

$$\sigma_y^2(\tau) = \frac{1}{2(M-1)} \sum_{i=1}^{M-1} (\bar{y}_{i+1} - \bar{y}_i)^2 = \frac{1}{2(N-2)\tau^2} \sum_{i=1}^{N-2} (x_{i+2} - 2x_{i+1} - x_i)^2, \quad (2.79)$$

computed based on adjacent fractional frequency deviations \bar{y}_i of sample size M or by means of N time error measurements x_i , with $N = M + 1$.

Since the standard AVAR exhibits a relatively low confidence level, the so-called *overlapping Allan variance* is the preferred measure of frequency stability in the time domain instead:

$$\begin{aligned} \bar{\sigma}_y^2(\tau) &= \frac{1}{2m^2(M-2m+1)} \sum_{j=1}^{M-2m+1} \left(\sum_{i=j}^{j+m-1} (y_{i+m} - y_i) \right)^2 \\ &= \frac{1}{2(N-2m)} \sum_{i=1}^{N-2m} (x_{i+2m} - 2x_{i+m} + x_i)^2. \end{aligned} \quad (2.80)$$

Compared to Equation (2.79), the overlapping AVAR applies an additional averaging factor m , thereby making use of all possible combinations of samples of the data set for a specific averaging time τ . This significantly increases the confidence level of the overlapping AVAR, but also causes certain correlations between the respective estimates of $\bar{\sigma}_y^2(\tau)$ depending on τ . However, as stated in Riley (2008), the overlapping AVAR is *the* measure of choice and will therefore be used in section 3.2 for determining the frequency stability of various oscillators. The basic concept of overlapping and non-overlapping samples is depicted in Figure 2.5.

The standard and overlapping AVAR cannot distinguish between WPM ($\alpha = 2$) and FPM ($\alpha = 1$) noise, because AVAR estimates get ambiguous for $\alpha \geq 1$ (Allan, 1966; Barnes et al., 1971). For a clear distinction, the so-called *modified Allan variance* $\bar{\sigma}_y^2(\tau)$ can be calculated. The basic idea behind this is, since both WPM and FPM noise depend on the measurement bandwidth, they can be distinguished by changing the bandwidth. This can be done either in the hardware, which is more laborious, or during stability analysis in the software (Allan and Barnes, 1981). Mathematically speaking, this leads to an additional phase averaging by factor m of the measurement samples:

$$\begin{aligned}\bar{\sigma}_y^2(\tau) &= \frac{1}{2m^4(M-3m+2)} \sum_{j=1}^{M-3m+2} \left(\sum_{i=j}^{j+m-1} \left(\sum_{k=i}^{i+m-1} (y_{k+m} - y_k) \right) \right)^2 \\ &= \frac{1}{2m^2\tau^2(N-3m+1)} \sum_{j=1}^{N-3m+1} \left(\sum_{i=j}^{j+m-1} (x_{i+2m} - 2x_{i+m} + x_i) \right)^2,\end{aligned}\quad (2.81)$$

with $\tau = m\tau_0$ and basic sampling interval τ_0 of a finite data set with, again, length $N = M + 1$. The estimates of $\bar{\sigma}_y^2(\tau)$ result in different slopes regarding WPM noise and FPM noise when plotted along double-logarithmic axes, thereby allowing for a precise distinction between these two noise processes. In general, power law noise processes present in an oscillator can be easily identified this way as described by Table 2.1 and depicted in Figure 2.6, since each noise type shows a distinct slope.

Although measures for frequency-domain and time-domain are usually applied for different kinds of frequency stability, i.e. short term and mid/long term, respectively, it is possible to convert between them. The corresponding conversion formulae were established by Barnes et al. (1971) and create relationships between the PSD coefficients h_α and the Allan variance. These formulae will also be used in section 3.2 to derive the spectral coefficients for application in Kalman filtering.

2.3.3 Crystal Oscillators

Apart from very low-precision voltage frequency oscillators and voltage controlled oscillators, the most widely used frequency standards are crystal oscillators (XOs). The signal of such an instrument is generated from the oscillation of a solid, vibrating crystal, in most cases quartz, excited to its resonance frequency by an electric voltage that depends on the material properties, e.g. shape and size, of the crystal in use. In addition to their small size of a couple millimeters, low power consumption

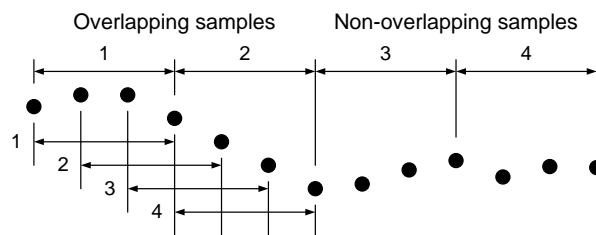


Figure 2.5: Overlapping and non-overlapping sampling of the Allan variance with an averaging factor $m = 3$ according to Riley (2008)

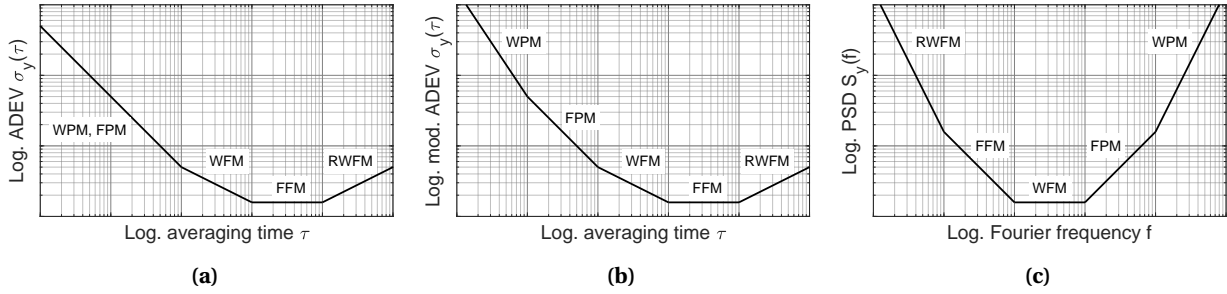


Figure 2.6: Power law noise processes depicted by (a) standard Allan deviation (ADEV), (b) modified ADEV and (c) power spectral density (PSD) of fractional frequency deviations on double-logarithmic (log) scales: white phase modulation (WPM), flicker phase modulation (FPM), white frequency modulation (WFM), flicker frequency modulation (FFM), random walk frequency modulation (RWFM)

and technical simplicity – what makes their commercial production very inexpensive –, XOs show the required accuracy and stability for application in a wide range of electronic devices, like e.g., televisions, smartphones, personal computers and, of course, GNSS receivers. However, XOs suffer from environmental influences, like e.g., temperature changes, magnetic and electrical fields as well as external vibrations, significantly degrading their frequency stability. Due to the fact that standard XOs are not designed with regard to long-term stability beyond one second, their stability is, if any, given as phase noise. Most often it is only characterized by its accuracy. Random frequency fluctuations induced by these sensitivities cause FFM noise to be the predominant noise in an XO signal. This makes the signal behavior very unpredictable even over short intervals of a few seconds.

In order to reduce the environmental sensitivities, further components are added to the oscillator circuit. Devices either compensating for temperature variations or avoiding them by keeping the crystal in an oven at a constant temperature are called temperature compensated crystal oscillator (TCXO) or oven controlled crystal oscillator (OCXO), respectively. These instruments provide typical frequency stabilities in the range of $\sigma_y(\tau) = 1 \cdot 10^{-9}$ (TCXO) to $\sigma_y(\tau) = 1 \cdot 10^{-12}$ (OCXO) at one second averaging time (Riehle, 2004), which decrease with increasing averaging time. However, OCXOs still provide stabilities better than $\sigma_y(\tau) = 1 \cdot 10^{-10}$ at 100 seconds averaging time (cf. Figure 2.7). Furthermore, hyperstable quartz oscillators show stabilities better than $\sigma_y(\tau) = 1 \cdot 10^{-13}$ for $0.3 \text{ s} \leq \tau \leq 500 \text{ s}$ according to Besson et al. (1999). Taking into account the considerations of section 2.1.5, a GNSS receiver is typically equipped with a TCXO.

2.3.4 Microwave and Optical Atomic Frequency Standards

Since the signal generated by an XO depends on the physical quantities of the crystal in use, such an oscillator is also called *macroscopic oscillator*. On the contrary, the operating principle of atomic frequency sources is based on electromagnetic transitions of free atoms or molecules. That is why they are also called *microscopic oscillators* (Riehle, 2004). The overall quality measure of such an oscillator is denoted by its so-called *Q factor*, which is the ratio between the oscillator (resonance) frequency and its bandwidth (*full width at half maximum*). Therefore, accuracy and stability of an oscillator can be improved by increasing the resonance frequency and/or decreasing its bandwidth.

The fundamental principle of generating a stable signal in a microscopic oscillator is based on the fact that atoms emit and absorb electromagnetic radiation at distinct frequencies, when they transition from one discrete energy level/state to another. This frequency depends on the atomic species in use, where typically elements like hydrogen, rubidium (Rb) or cesium (Cs) are applied. Apart from that, since their respective transition frequencies of roughly 1.4 GHz, 6.8 GHz and 9.2 GHz range in

the microwave domain, the corresponding instruments are called microwave oscillators or clocks, respectively. Although the physical and technical realizations of all three clock types differ, they share the same basic architecture consisting of, besides some sort of control electronics, a source containing the respective atomic species, magnetic state selectors, a (cavity) resonator and an output signal generating quartz oscillator tuned to the transition frequency. It can be further distinguished between two types of technical implementations of such a clock.

Active microwave atomic clocks directly use the frequency of the electromagnetic radiation to generate their output signal. Today, the most popular and widespread representative of this category is a clock following the concept of microwave amplification by stimulated emission of radiation (maser), known as hydrogen maser. Inside such an instrument, hydrogen atoms are pumped from the source through a vacuum with a magnetic state selector in it, where only the atoms of the desired higher energy level are passed on to the storage bulb located inside a cavity resonator. The transition frequency emitted by the atoms in this bulb is then used to steer or tune, respectively, the frequency of a quartz oscillator, which subsequently generates the output signal. Note that the longer the atoms interact in the bulb the better the transition frequency can be detected. To this day, hydrogen masers provide the best frequency stability of any *commercially* available frequency standard (cf. Figure 2.7). This applies to both short-term and long-term stability of $\sigma_y(\tau) \approx 2 \cdot 10^{-13}$ at $\tau = 1$ s and a flicker floor of $\sigma_y(\tau) \approx 2 \cdot 10^{-15}$ after one hour averaging time.

Apart from that, most of today's microwave atomic clocks – including Rb and Cs clocks – are *passive* instruments though. In the context of hydrogen masers, which, as described, are referred to as active

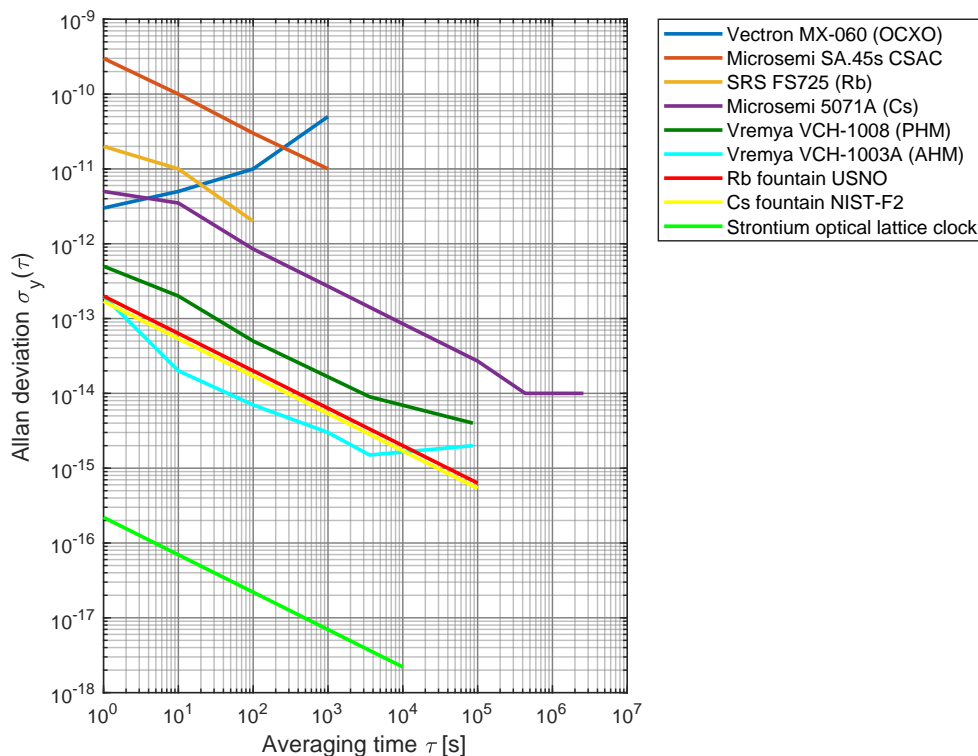


Figure 2.7: Allan deviations of typical oscillators and frequency standards: Vectron MX-060 oven controlled crystal oscillator (OCXO) (Vectron, 2018), Microsemi SA.45s chip-scale atomic clock (CSAC) (Microsemi, 2018b), Stanford Research Systems (SRS) FS725 rubidium (Rb) standard (SRS, 2018a), Microsemi 5071A cesium (Cs) standard (Microsemi, 2018a), Vremya VCH-1008 passive hydrogen maser (PHM) (Vremya-CH, 2018b), Vremya VCH-1003A active hydrogen maser (AHM) (Vremya-CH, 2018a), United States Naval Observatory (USNO) rubidium fountain (Peil et al., 2016), National Institute of Standards and Technology (NIST) cesium fountain (Heavner et al., 2014), strontium-87 optical lattice clock (Nicholson et al., 2015)

hydrogen masers (AHMs), their passive counterparts are, strictly speaking, not masers, because their output signal is not generated directly from the self-sustained oscillations of the hydrogen atoms. Instead the cavity of a PHM is coupled with the signal of an external generator, mostly a quartz oscillator, that coincides with the transition frequency of the atoms, thus resonating with it. The generator signal is then tuned by interrogating the amplified signal of the maser and subsequently correcting the output signal. Compared to an AHM, this makes a PHM less complex and less expensive to build, whilst still providing a decent frequency stability that is only approximately about one order of magnitude lower than that of an AHM – as can be seen exemplarily from Figure 2.7. For example, all Galileo FOC satellites are equipped, among others, with PHMs since they should provide enhanced accuracy and stability compared to typical spaceborne Rb clocks (Steigenberger and Montenbruck, 2017).

The next most stable, especially in the long term, microwave atomic clocks are Cs clocks, subdivided into two types: *beams* and *fountains*; the main difference being that fountains allow for extended interrogation times in their cavity resonator (Heavner et al., 2014). Their large physical dimensions, however, are the reason why fountains are almost exclusively used in laboratories, although a cesium fountain is part of the ESA atomic clock ensemble in space (ACES) experiment on board the International Space Station (ISS) (Cacciapuoti and Salomon, 2011; Meynadier et al., 2018). In fact, cesium clocks play an important role in the definition and realization of the International System of Units (SI): the hyperfine structure level transition of ^{133}Cs is the basis of the official definition of the SI second (Terrien, 1968). The frequency stability of Cs fountains can be assessed to $\sigma_y(\tau) \approx 2 \cdot 10^{-13} \tau^{-\frac{1}{2}}$ for averaging times of one second to 10,000 seconds (Heavner et al., 2014), thus providing a better long-term stability than an AHM. Cesium beams, on the other hand, are smaller in size, ranging from laboratory devices to more compact commercial frequency standards. The latter provide a typical frequency stability of $\sigma_y(\tau) = 1 \cdot 10^{-11} \tau^{-\frac{1}{2}}$ and better for $1 \text{ s} \leq \tau \leq 10,000 \text{ s}$ (Microsemi, 2018a).

The most widespread used atomic clocks are Rb frequency standards because of their rather compact and inexpensive construction and manufacturing. Thanks to a fortuitous overlap of transitions between the two isotopes ^{87}Rb and ^{85}Rb , a rubidium clock can be manufactured very simply by means of a discharge lamp, an isotopic filter and a vapor cell resonator interrogated with the rubidium resonance frequency generated by an XO. However, an Rb clock provides lower frequency stability than a Cs clock and a hydrogen maser as depicted in Figure 2.7. At this point, it is worth mentioning that also rubidium fountains have been developed in recent years, for example at the United States Naval Observatory (USNO) providing frequency stabilities similar to cesium fountains (Peil et al., 2016).

The newest generation of atomic clocks work in the optical domain applying atomic species whose transition frequencies range in the terahertz band. The groundwork for the first concept of a *single-ion clock* goes back to the second half of the 20th century, when the so-called *Paul trap* was invented (Paul and Steinwedel, 1956; March, 1997). Since the start of the new millennium, a second concept called *optical lattice clock* emerged and advanced as a more and more legit alternative implementation over the years. Typical atomic species used in an optical clock – regardless of concept – are strontium, ytterbium, magnesium and aluminum. Because of their approximately 50,000 times higher transition frequencies of ca. 429 THz, optical clocks theoretically can provide levels of accuracy and stability tremendously higher than microwave atomic clocks working between 1.4 GHz and 9.2 GHz (Ido, 2012). The basic functional principle is the same for both concepts: the atomic state transition is excited through a light amplification by stimulated emission of radiation (laser) at the resonance frequency of the atom species in use, the difference between laser and transition frequency is measured by a spectrometer and fed back in order to tune the laser frequency accordingly. The kind of transition applied by either a single isolated ion in a Paul trap or many neutral atoms trapped in an optical lattice, defines the type of such an optical clock. Today, the best instruments of both types provide a frequency stability better than $\sigma_y(\tau) = 3 \cdot 10^{-16} \tau^{-\frac{1}{2}}$ for averaging times up to at least 1000 seconds (Nicholson et al., 2015; Huntemann et al., 2016), thereby being almost 100 times more stable than the best cesium clocks. However, due to their complexity, these clocks are still restricted to laboratory applications.

2.3.5 Chip-scale Atomic Clocks

Besides steadily developing atomic clocks with improved stability and accuracy, the second direction of development is towards ever *smaller* precision oscillators. The most prominent one is the so-called *chip-scale atomic clock (CSAC)*, which started as a research project of the US DoD Defense Advanced Research Projects Agency (DARPA) in 2001. The main goal was to develop and manufacture an atomic clock with the size of a microchip that even soldiers can be easily equipped with, thus enabling (better) position determination in harsh environment or yet in the absence of GPS. One might argue that already highly stable crystal oscillators and small-sized rubidium clocks exist. However, on the one hand, XOs are too sensitive against environmental influences and thereby prone to severe frequency drifts and, on the other hand, rubidium clocks consume too much power ($> 10\text{ W}$) to be run on batteries. In addition, both clock types are still too large for the targeted applications.

The groundwork towards a microchip-sized atomic clock was laid by the group of John Kitching at the US National Institute of Standards and Technology (NIST) until the mid 2000s. The initial design concept of such a clock is shown in Figure 2.8a. The biggest challenges were the reduction of the size of the vapor cell as well as building a cavity that is much smaller than it usually has to be in order to excite the atoms in it to resonance by means of conventional techniques (Kitching et al., 2002). Furthermore, the atomic species in use, like e.g., rubidium or cesium, are typically vaporized by a discharge lamp, but this consumes too much power to be applied in a CSAC. Therefore, in order to overcome these problems, the authors proposed an all-optical design approach in combination with MEMS components: (i) the discharge lamp is replaced by a diode laser; (ii) the cavity size is reduced by means of coherent population trapping (Arimondo, 1996) making it independent of the microwave radiation wavelength; (iii) a MEMS photo detector is used. In conclusion, Kitching et al. (2002) also gave a first, purely analytical estimate for the fundamental limit of the achievable frequency stability of such a clock as $\sigma_y(\tau) = 3 \cdot 10^{-11}$ at one second averaging time.

By the year 2004, a first micro-fabricated physics package with the size of less than 10 mm^3 and a maximum power consumption of 75 mW was developed as depicted in Figure 2.8b. It basically consists of a vertical-cavity surface-emitting laser, a cesium vapor cell and a silicon positive intrinsic negative photodiode. For more detailed information, it is referred to Knappe et al. (2004). The frequency stability of this clock was assessed to $\sigma_y(\tau) = 2.4 \cdot 10^{-10} \tau^{-\frac{1}{2}}$ for $1\text{ s} \leq \tau \leq 100\text{ s}$. Furthermore, the authors pointed out the possibility of simple and relatively inexpensive mass production of such a physics package because all components could be fabricated on a single large wafer and subsequently assembled together. They also concluded that construction of a complete clock by adding a local oscillator and control electronics appears feasible – with a projected frequency stability of $\sigma_y(\tau) < 1 \cdot 10^{-11}$ at one hour averaging time.

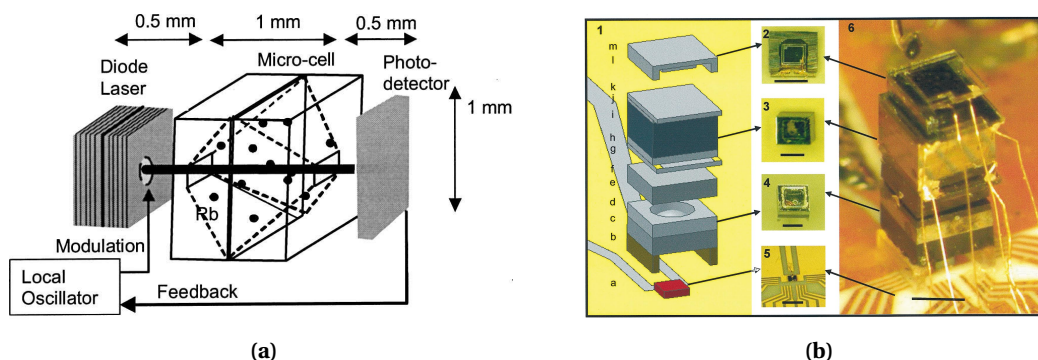


Figure 2.8: (a) Basic design of a chip-scale atomic clock (Kitching et al., 2002, p. 553) and (b) the first technical realization of its physics package with black lines indicating 1 mm (Knappe et al., 2004, p. 1461)

After years of development, the first commercial CSAC was launched in the year 2011 by the company *Symmetricon Inc.* – shortly after acquired by the *Microsemi Corporation* – with a frequency stability of $\sigma_y(\tau) \approx 3 \cdot 10^{-10} \tau^{-\frac{1}{2}}$ for $1 \text{ s} \leq \tau \leq 1000 \text{ s}$. Its overall volume and power consumption amount to 17 cm^3 and less than 120 mW , respectively. In the years to follow, other manufacturers released oscillators under license based on the Symmetricon/Microsemi product, like e.g., the *Jackson Labs LN CSAC*. To this day, the *Microsemi SA.45s CSAC* is still, however, the only commercially available CSAC module. Nevertheless, further developments towards an even smaller and less power consuming version (1 cm^3 , $< 30 \text{ mW}$) are underway (Lutwak, 2011). In 2016, Microsemi released a thermally-improved version of its CSAC with a wider operating temperature range, now spanning from -10°C to $+70^\circ\text{C}$. Prior to that, the upper operating temperature was restricted to $+35^\circ\text{C}$. This improvement comes without compromising either reliability or overall performance (Microsemi, 2018c).

Today, CSACs find widespread use in time synchronization and time keeping applications, GNSS navigation as well as in secure communication and automobile collision avoidance systems (Lutwak, 2011). Furthermore, they are also applied in ocean bottom seismography to synchronize various underwater sensors at the millisecond level or better over at least one year (Gardner and Collins, 2012).

In conclusion, its small form factor and ability to be run on customary batteries make a CSAC very suitable for mobile GNSS applications. Connecting it to a GNSS receiver, thus replacing the less stable and less accurate internal quartz oscillator, should enable physically meaningful receiver clock modeling. Therefore, the requirements for this approach are discussed and various small-sized atomic clocks – including two CSACs – are investigated regarding their frequency stability in the next two chapters.

3

Receiver Clock Modeling

3.1 Concept and Requirements

The basic idea of receiver clock modeling (RCM) can be traced back to some 20 years ago (Misra, 1996). Instead of estimating the receiver clock biases independently on an epoch-by-epoch basis, they are modeled over multiple epochs – depending on the frequency stability of the oscillator in use. This approach reduces both the correlations between clock parameters and other elevation-dependent parameters and, at least in classical least-squares parameter estimation, the overall number of parameters. In addition, the more epochs contribute to a common modeling parameter the closer overall parameter estimation gets to the case of true ranging, where receiver clock biases are completely absent (Weinbach, 2013). However, the clock model of choice has to represent the clock behavior in a physically meaningful way. This means that, on the one hand, it has to appropriately account for the deterministic (offset, drift, aging) and stochastic (random frequency deviations) character of the oscillator in use. As a result of that, on the other hand, the reduction of the number of parameters must not be too strong since this under-representation or under-parametrization, respectively, can distort the parameter estimates (Koch, 1999). The underlying concept and prerequisites for physically meaningful RCM in this thesis are based on the work of Weinbach (2013), from which the following three most important findings are drawn.

First and foremost, the integrated frequency noise of the oscillator in use has to be smaller than the receiver noise. The latter is mainly driven by the noise of the applied observation type(s), which, in the case at hand, are GPS and GLONASS L1 C/A-code and Doppler observations. Thus, the random frequency fluctuations of the oscillator cannot be resolved by the GNSS observations in PVT estimation. The oscillator noise is typically assessed by its frequency stability in terms of the Allan variance and the time prediction error derived thereof. On the other hand, the observation noise typically amounts to white phase noise of one percent of the signal wavelength. If an elevation-dependent weighting scheme is applied, this value has to be multiplied with the smallest possible time dilution of precision (TDOP) value at the user location. On a global scale, this value has been assessed to approximately 1.6 by Weinbach (2013).

Secondly, an analytical comparison between static positioning with and without RCM showed, that the latter does not improve the precision of the position solution – provided that the average direction of observations does not change significantly over time.

Thirdly, since the *estimated* receiver clock bias also includes or absorbs, respectively, the receiver hardware delays, they have to be accounted for in some way if receiver clock *modeling* is applied. Variations in these receiver-specific hardware delays – including GNSS antenna, antenna cable, signal splitter and the receiver itself – are almost exclusively induced by temperature changes and range on the centimeter level per degree Celsius for code observations (Ray and Senior, 2005). Fonville et al. (2007) reported values of less than 60 mm/°C for single-frequency GPS P-code measurements, where Zhang and Lombardi (2010) determined maximum variations of 45 mm/°C for the ionosphere-free LC

of GPS L1 and L2 P-code observations. Assuming similar effects for L1 C/A-code observations, this means that even temperature variations of 5°C within a clock modeling interval will lead to maximum delay changes of 0.3 m, which is still below the typical pseudorange observation noise. Furthermore, such temperature changes usually increase slowly and do not occur abruptly. This ultimately leads to a different drift behavior of the clock time bias, which is no limitation for clock modeling.

In conclusion, RCM will solely be applied in *kinematic* GNSS applications throughout this thesis. Furthermore, since only geodetic receivers are used, the observation noise is assessed to values distinctly smaller than one percent of the signal wavelength. For example, the latter amounts to a value of approximately three meters in case of GPS L1 C/A-code observations, but manufacturers of such receivers usually specify sub-meter values down to ten centimeters (JAVAD GNSS, 2018). Therefore, rather cautious values of one meter for GPS and GLONASS L1 C/A-code – and 3 cm/s for L1 Doppler – observations are used in the following. Multiplied by the TDOP value of 1.6 yields the lower bound observation noise values depicted in Figure 3.1 when modeled as WPM and WFM noise, respectively, over time. These values can be considered lower bounds because, in reality, GNSS observation noise is further degraded by a variety of environmental influences such as atmospheric and multipath effects. Figure 3.1a shows these lower bounds for GPS L1 C/A-code and Doppler observations together with typical ADEV frequency stabilities of oscillators comparable to those applied in this thesis later on.

The oscillator noise is assessed by means of its frequency stability which is usually provided by the manufacturer in terms of Allan deviations for a few averaging times. By converting these values to so-called *time prediction errors*, the evolution of the time deviation of an oscillator can be computed for prediction intervals up to the length of the data set (Allan and Hellwig, 1978):

$$x(\tau_p) = \tau_p \sqrt{\frac{a^2}{3\tau_p^2} + \frac{b^2}{\tau_p} + 1.4c^2 + \sigma_y^2(\tau_L) \left[0.4 + 1.5 \left(\frac{\tau_p}{\tau_L} \right)^\mu + 0.003 \left(\frac{\tau_p}{\tau_L} \right)^2 \right]}, \quad (3.1)$$

with

- $x(\tau_p)$ the time prediction error,
- τ_p the prediction interval,
- τ_L the maximum averaging time (typically 10% of the total data length T) and
- $\sigma_y(\tau_L)$ the Allan deviation at τ_L ,
- a, b, c the values of $\sigma_y(\tau)$ at $\tau = 1$ s for the independent noise processes WPM/FPM (τ^{-1}), WFM ($\tau^{-1/2}$) and FFM (τ^0), respectively,
- μ the power law noise slope coefficient.

Typically, the latter is assessed to $\mu = 1$ (RWFM) for $\tau_p < \tau_L$. In case of $\tau_p \geq \tau_L$, values for WFM ($\mu = -1$) or FFM ($\mu = 0$) could be chosen. However, due to the factor of 1.5 in the square bracket the assumption of RWFM still ensures that the actual time error is well within 1σ (68%) of a normal distribution (Allan and Hellwig, 1978).

The Allan deviations as given by the manufacturers of three exemplary oscillators are depicted in Figure 3.1a. The corresponding time errors shown in Figure 3.1b are computed based on the parameters listed in Table 3.1. Note that deterministic effects such as offset, drift and aging are excluded for these theoretical considerations since they strongly depend on the respective application, but do not restrict clock modeling because the receiver clock biases are estimated and not predicted based on past time errors (Weinbach, 2013). Physically meaningful RCM is possible for intervals in which the predicted time error of the clock $x(\tau_{\text{RCM}})$ is smaller than the receiver noise σ_{rx} , that is $x(\tau_{\text{RCM}}) < \sigma_{\text{rx}}$. In the exemplary case of the Microsemi CSAC, the maximum clock modeling interval amounts to approximately 100 seconds when using GPS L1 C/A-code observations. With regard to GPS L1 Doppler observations, physically meaningful RCM is not possible since the integrated clock noise is approximately two times higher than the receiver/observation noise.

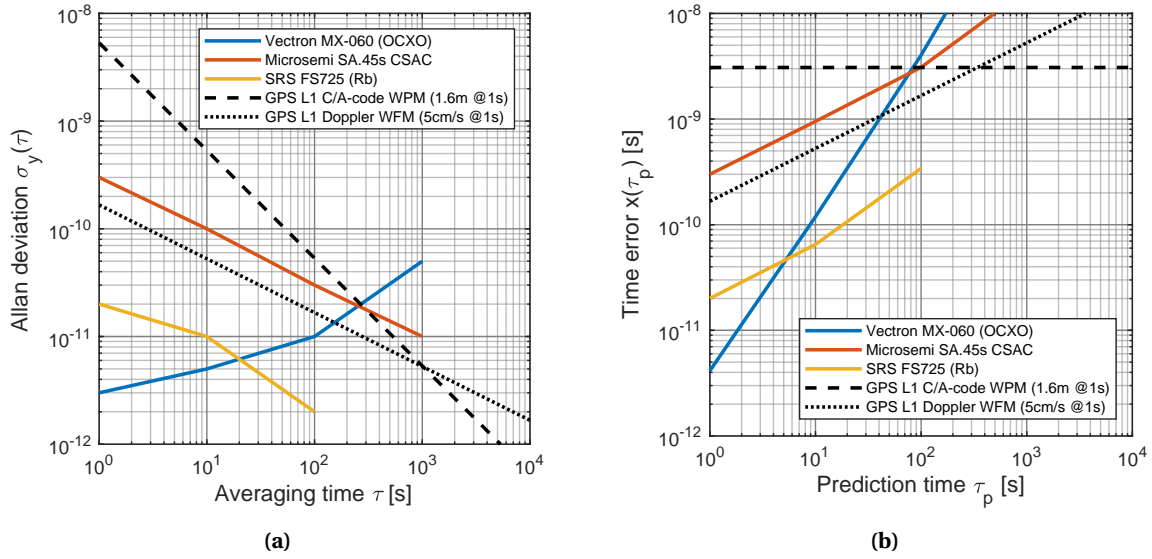


Figure 3.1: (a) Allan deviations and (b) time prediction errors of exemplary oscillators Vectron MX-060 oven controlled crystal oscillator (OCXO) (Vectron, 2018), Microsemi SA.45s chip-scale atomic clock (CSAC) (Microsemi, 2018b), Stanford Research Systems (SRS) FS725 rubidium (Rb) standard (SRS, 2018a), as well as GPS observation noise of L1 C/A-code modeled as white phase modulation (WPM) noise and L1 Doppler modeled as white frequency modulation (WFM) noise

After defining and reviewing the requirements for reasonable receiver clock modeling in GNSS navigation, the resultant conclusions have to be transferred to appropriate models that can be applied in data analysis. The specific implementations are discussed in detail in section 3.3. In order to derive individual clock models and maximum modeling intervals, first various miniature atomic clocks (MACs) that are going to be used in kinematic GNSS applications in chapter 4 are characterized in terms of their individual frequency stability.

3.2 Frequency Stability of Atomic Clocks

3.2.1 Introduction and Background

The stochastic behavior of a given oscillator, further also referred to as device under test (DUT), can be determined by comparing it against another oscillator of at least one order of magnitude higher stability and accuracy. The corresponding values in terms of phase noise or Allan deviations are usually provided by the manufacturer. For the purposes of this thesis, however, individual characterization of three MACs are carried out because manufacturer's data are (a) often only available for few averaging times and (b) not specific for one instrument but for a whole product series.

Table 3.1: Manually assessed parameter values for the determination of time prediction errors of *exemplary* oscillators: upper limit of averaging times τ_L with sufficiently significant Allan deviation $\sigma_y(\tau_L)$, power law noise slope coefficient μ , values a , b , c of $\sigma_y(\tau = 1\text{ s})$ for white/flicker phase noise, white frequency noise and flicker frequency noise, respectively

Oscillator	τ_L [s]	$\sigma_y(\tau_L)$	a	b	c	μ
Vectron MX-060 OCXO	1	$3 \cdot 10^{-12}$	0	0	0	1
Microsemi SA.45s CSAC	1000	$1 \cdot 10^{-11}$	0	$3 \cdot 10^{-10}$	0	1
Stanford Research Systems (SRS) PRS10	100	$2 \cdot 10^{-12}$	0	$2 \cdot 10^{-11}$	0	1

The underlying measurements were carried out from December 2013 until January 2014 at Physikalisch-Technische Bundesanstalt (PTB), Braunschweig, Germany's national metrology institute (Krawinkel and Schön, 2014). In so doing, the 10 MHz output signals of the DUTs were compared to the phase of an AHM of the type *Vremya VCH-1003A* by means of a *TimeTech* multi-channel phase comparator. Two different sampling intervals were applied for these comparisons: short-term and mid-term frequency stability is assessed by means of a measurement sampling interval of one second lasting for a couple of hours, the long-term stability is characterized based on measurements each 100 seconds over the course of roughly one week. By analyzing the measurement data, frequency stability measures are computed in the time domain in terms of overlapping ADEV and in the frequency domain by means of PSD estimates of fractional frequency deviations. Based on the latter, intensity coefficients to be applied for receiver clock modeling in a Kalman filter are derived. Alternatively, a clock can also be characterized by means of wavelet analysis (Percival, 2003), which is not applied in this thesis.

The following three miniature atomic clocks were tested. The *Microsemi SA.45s* CSAC was the first commercially available CSAC introduced in the year 2011 as described in section 2.3.5. Its small-sized volume and weight combined with a very low power consumption set it apart from any other oscillator providing a comparable frequency stability (cf. Figure 3.1). Based on the Microsemi CSAC module, other manufacturers released their own products. One of those is the *Jackson Labs LN CSAC* (Jackson Labs, 2018). Besides the raw CSAC signal, this clock also provides a second, low noise (LN) signal with enhanced short-term stability generated by an OCXO post-filter replacing the built-in TCXO of the CSAC module. Therefore, it is distinguished between the CSAC and the OCXO signal for the remainder of this thesis, denoted as *Jackson Labs CSAC* and *Jackson Labs OCXO*, respectively. In addition, a *u-blox* GPS chip (UBX-G6010-ST-TM) is integrated into the instrument, thereby enabling the clock to operate as a GPS disciplined oscillator (GPSDO), which improves its long-term stability by means of the GPS timescale. Furthermore, a legacy rubidium clock, the *SRS PRS10*, is also tested together with the CSACs. Although it is relatively small in size measuring about 390 cm³ and weighing 600 g, the PRS10 consumes much more power, at least 50 W during warm-up and ca. 14 W in normal operation (SRS, 2018b).

3.2.2 Oscillator Comparisons

Raw Data Analysis

Frequency stability analysis always requires a thorough pre-analysis or pre-processing, respectively, of the raw data time series, that is fractional frequency deviations or – in the case at hand – phase deviations. Such an analysis includes converting phase to frequency data and vice versa, closing of data gaps, removing of outliers and any deterministic effects like offset, drift and aging, as well as combining multiple time series for a longer averaging time (Riley, 2008). To be exact, the pre-analysis at hand consists of the following processing steps:

1. Conversion of phase data to frequency data.
2. Detection of data gaps, where thresholds for small and big gaps are defined manually:
 - Small gaps (less than or equal ten epochs) are closed by linear interpolation. Since only few gaps are detected with respect to the overall sample size (cf. Table 3.2), the low-pass-filter-like effect associated with this approach is considered to be negligible small.
 - In case big gaps (more than ten epochs) occur, the original data is split into separate time series, which are treated individually in further pre-processing steps.
3. Removing of outliers by means of a rejection threshold that is defined as the product of a manually defined multiplication factor and the median of the underlying time series.

All this is necessary to fully explore the stochastic behavior of the DUTs since the deterministic effects depend on the test environment and would lead to falsified stability measures if they were not reduced from the original time series. Of course, also the stochastic behavior can vary on a case-by-case basis (Allan and Hellwig, 1978), for example if the clocks are exposed to vibrations in kinematic application. The results of the raw data analysis of the three tested clocks are discussed in the following and a short summary is given by Table 3.2.

The Jackson Labs CSAC signal shown in Figures 3.2a and 3.3a exhibits a relative frequency offset of $-16 \cdot 10^{-12}$ in both the one-second and 100-second data. The frequency drift of $-3 \cdot 10^{-12}$ per day in the 100-second data cannot be detected in the one-second data simply because of the much shorter measuring time. After removing offset and drift, the fractional frequency deviations are in the range of $\pm 0.2 \cdot 10^{-9}$ with zero mean.

As expected, the negative long-term drift of the CSAC signal is also present in the OCXO post-filter signal. An apparent issue in regard of steering the OCXO towards the CSAC module was encountered not until the one-second measurements were finished and the 100-second measurements were already started for about one and a half days. In fact, the default PLL settings between the OCXO and the CSAC module were not properly configured. By adjusting the *phase correction parameter* of the proportional-integral-derivative (PID) loop, the OCXO overshoots when steered to the CSAC module were reduced, as far as possible. Since these adjustments were applied during the ongoing measurements, the effects can be seen in Figure 3.3b after approximately 2.2 days. From that point on, the course of the fractional frequency deviations becomes a little smoother compared to before. The one-second measurements depicted in Figure 3.2b show distinct residual systematics and varying short-term frequency drifts typical for an OCXO. The frequency offset in both data sets amounts to approximately $-10 \cdot 10^{-12}$. Overall, the fractional frequency deviations are about ten times smaller than the ones of the CSAC signal.

The phase data of the Microsemi CSAC shown in Figures 3.2c and 3.3c exhibit some gaps which are due to manual interruptions. In frequency stability computations, the separate time series before and after a big gap are concatenated to one overall time series. This is a valid approach since all deterministic effects and outliers are removed after data pre-processing. Alternatively, frequency stability can be computed considering these data gaps as proposed by Sesia and Tavella (2008) which, however, comes with certain drawbacks: (a) time-domain ADEVs cannot be estimated for averaging times that refer to the timestamps of these data gaps, (b) spectral analysis can get complicated since methods based on a fast Fourier transform (FFT) require evenly-spaced, gapless data. In case of the long-term data (Figure 3.3c), a significant frequency drift is present in the range of $5 \cdot 10^{-12}$ per day, which cannot be seen in the short-term measurements of Figure 3.2c. This drift leads to jumps in the phase deviations when they become greater than $10 \mu\text{s}$. The initial frequency offsets in both time series amount to ca. $36 \cdot 10^{-12}$. It can also be stated that the scattering of the reduced measurement samples is only half as large as that of the corresponding time series of the Jackson Labs CSAC (cf. Figures 3.2a and 3.3a).

Table 3.2: Pre-analysis results of clock comparison measurement data: small gaps (less than or equal ten epochs) include previously rejected outliers; numbers in parenthesis indicate how many of each preceding number are due to resets/jumps of the phase comparator

Oscillator	# samples		# outliers		# small gaps		# big gaps	
	1 s	100 s	1 s	100 s	1 s	100 s	1 s	100 s
Jackson Labs CSAC	32,291	4833	0	0	4	0	0	0
Jackson Labs OCXO	32,291	4833	0	17 (0)	4 (0)	7 (0)	0	0
SRS PRS10	68,399	12,094	0	12 (12)	3 (0)	13 (12)	0	0
Microsemi CSAC	15,862	4442	0	5 (4)	4 (0)	5 (4)	1	3

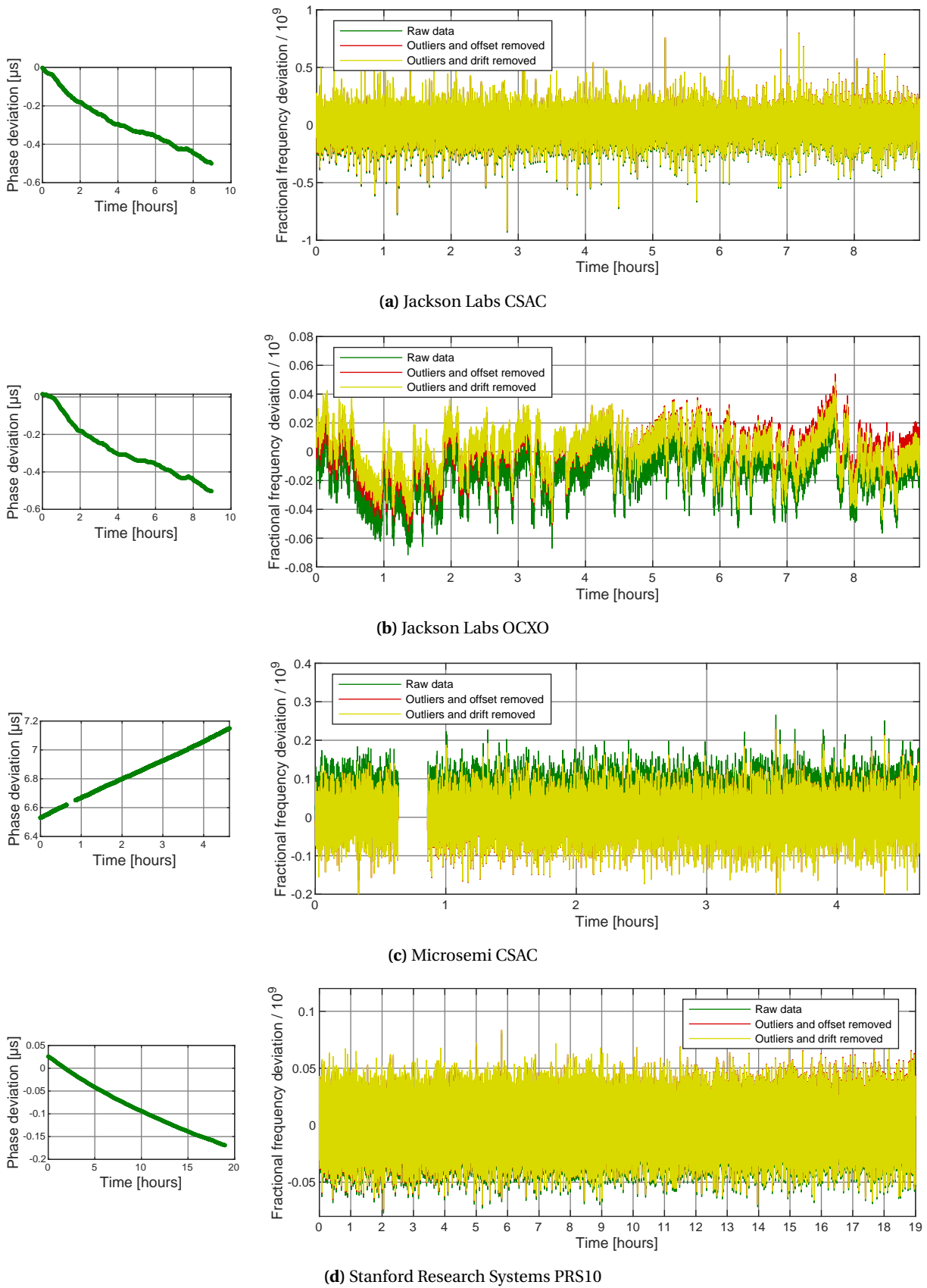


Figure 3.2: Measurement data of clock comparisons with a sampling interval of one second: raw phase deviations is converted to fractional frequency deviations, thereof removed from outliers, offsets and drifts. Please note the different scalings of the y-axes.

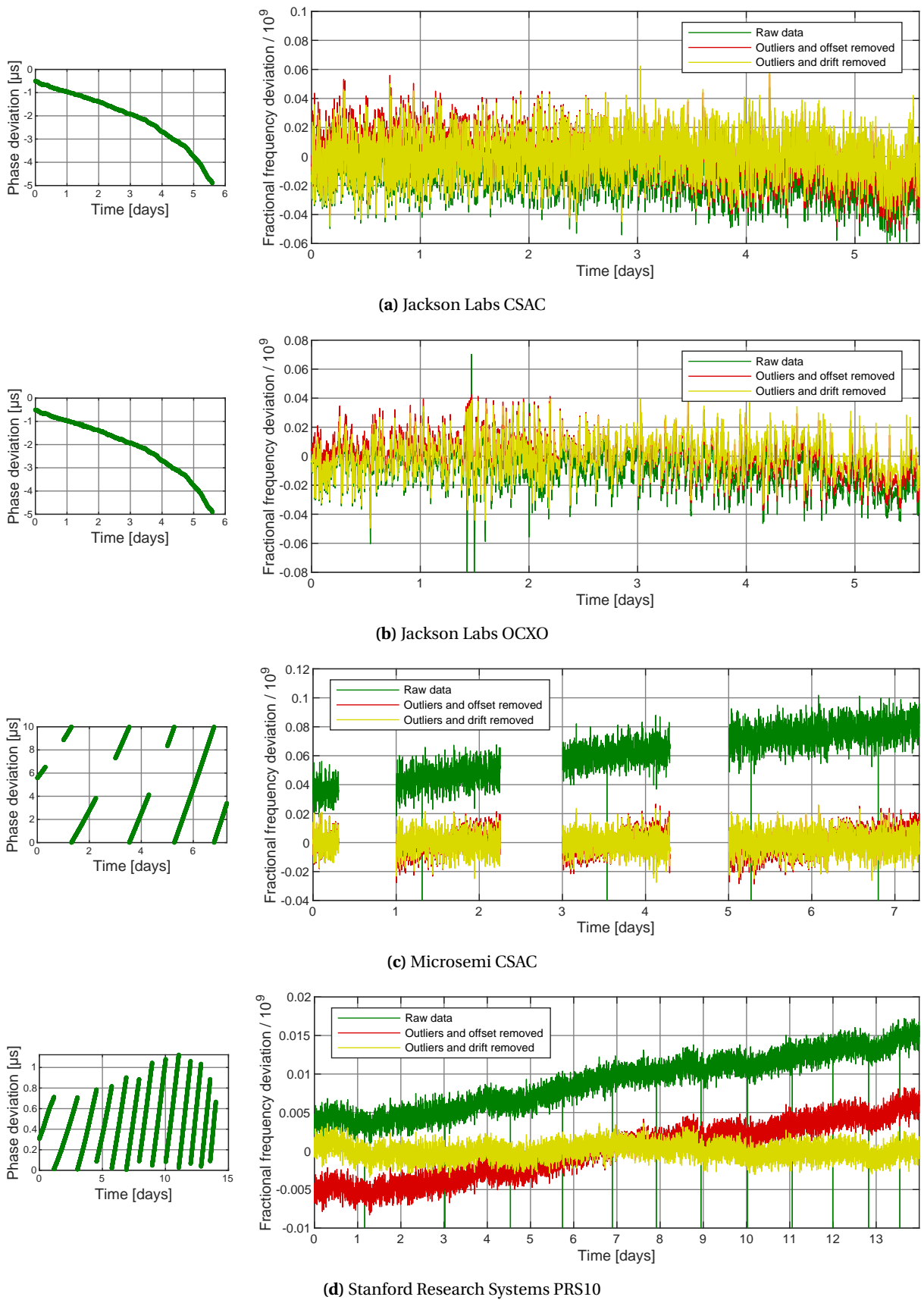


Figure 3.3: Measurement data with a sampling interval of 100 seconds: raw phase deviations is converted to fractional frequency deviations, thereof removed from outliers, offsets and drifts. Please note the different scalings of the y-axes.

The most precise behavior of all DUTs shows in case of the SRS PRS10 rubidium standard. The one-second data does exhibit a marginal frequency offset of $-4 \cdot 10^{-12}$ and a negligible frequency drift (cf. Figure 3.2d). The reduced data then scatters around zero with $\pm 25 \cdot 10^{-12}$ very homogeneously. Long-term offset and drift depicted in Figure 3.3d amount to $9 \cdot 10^{-12}$ and $1 \cdot 10^{-12}$ per day, respectively.

Time-domain Frequency Stability

After pre-processing, the reduced time series shown in Figures 3.2 and 3.3 are the basis for the computation of overlapping ADEV according to Equation (2.80), which are the most common measure of time-domain frequency stability due to the increased statistical confidence of its estimates (Riley, 2008). These values are determined for maximum averaging times that are a tenth of the overall data length of the (concatenated) reduced time series. Figure 3.4 and Figure 3.5a show the resulting overlapping ADEV estimates for averaging times from one second to ca. 14.5 hours (51,200 s). The double-sided confidence intervals $s_{\bar{\sigma}_y}(\tau)$ are computed based on the overlapping ADEV itself, the noise process type identified by the lag 1 autocorrelation (Riley and Greenhall, 2004), the number of data samples N_τ , averaging factor m and the χ^2 -distributed degrees of freedom ζ (Howe et al., 1981):

$$\bar{\sigma}_y(\tau) \left(1 - \sqrt{\frac{\zeta(\alpha, N_\tau, m)}{\chi_{\zeta, 1-\eta/2}^2}} \right) \leq s_{\bar{\sigma}_y}(\tau) \leq \bar{\sigma}_y(\tau) \left(\sqrt{\frac{\zeta(\alpha, N_\tau, m)}{\chi_{\zeta, \eta/2}^2}} - 1 \right), \quad (3.2)$$

with a given significance level of $\eta = 0.05$, in the case at hand. Due to the large sample size, the 95%-confidence intervals are very small for averaging times up to 3200 s each.

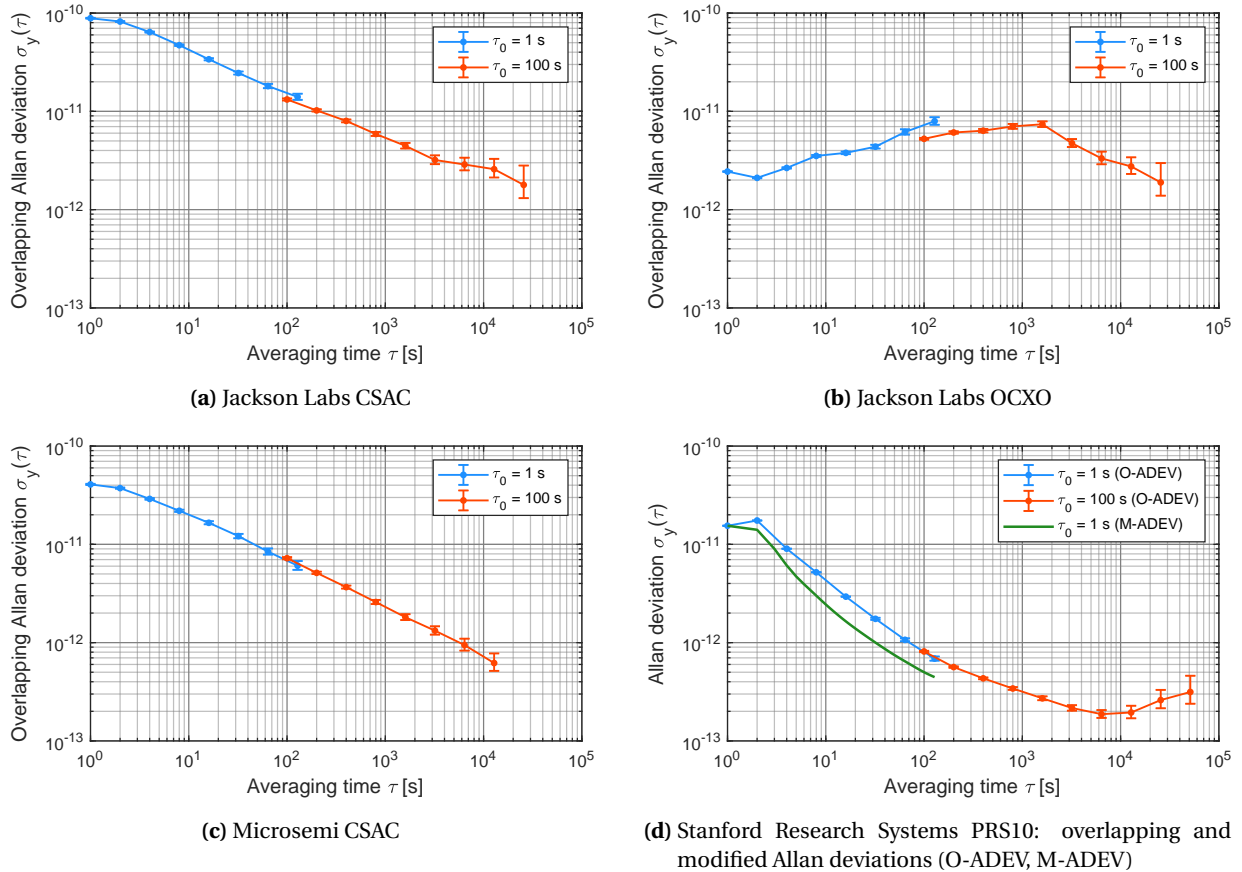


Figure 3.4: Individual Allan deviations with 95%-confidence intervals of devices under test computed from two different sampling intervals τ_0

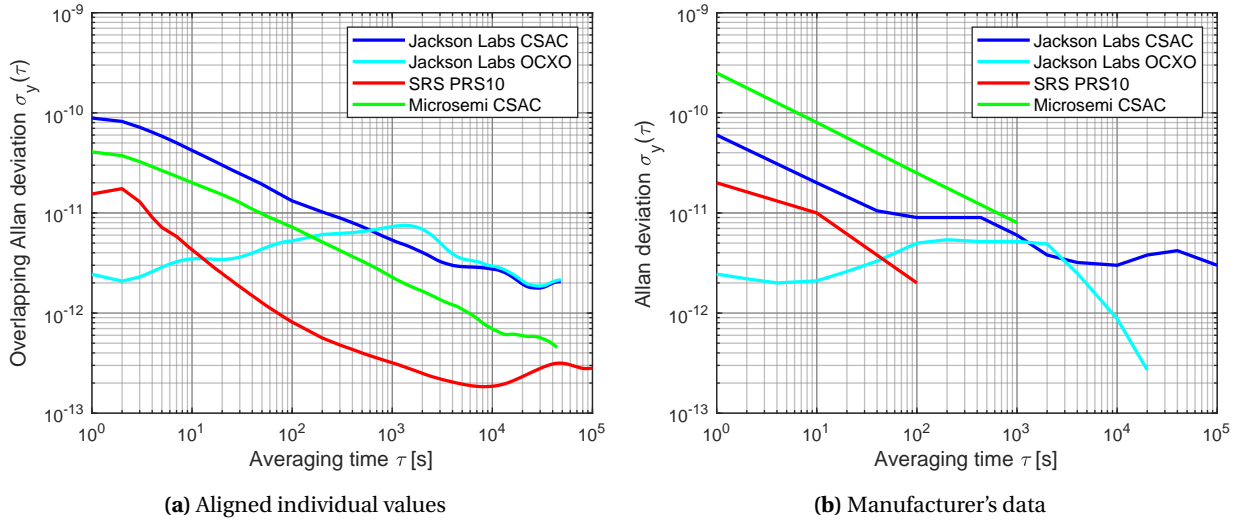


Figure 3.5: Joint depiction of aligned individual Allan deviations of devices under test

In order to concatenate the ADEV curves computed from the one-second and the 100-second data, the one-second curves are proportionally aligned to the 100-second curves. There are two reasons for that: (a) the 100-second curves exhibit smaller confidence intervals at the tie point ($\tau = 100$ s) than the one-second data, (b) the resulting changes in the one-second ADEVs at this tie point lie well within the confidence intervals of the 100-second curves there. Since the latter reason does not apply to the Jackson Labs OCXO shown in Figure 3.4b, a short explanation is necessary. As mentioned in the discussion of raw data analysis before, this particular oscillator was partly working with non-optimal PLL parameters between the OCXO and the CSAC module. Whereas all of the one-second data was recorded with the manufacturer's default settings, the 100-second data contains measurements with both the default and the improved PLL settings (cf. Figure 3.3b). These improved measurements lead to an enhanced frequency stability at $\tau = 100$ s of $\sigma_y(\tau) = 5.2 \cdot 10^{-12}$. Computing the same value without the improved measurements yields $\sigma_y(\tau) = 6.2 \cdot 10^{-12}$. Therefore, it can be assumed that the improved oscillator settings would theoretically lead to a better ADEV estimate at $\tau = 100$ s for the one-second measurements and thus aligning of the one-second data to the 100-second data is justified in this particular case. The aligned ADEV curves are depicted in Figure 3.5a. For comparison reasons, the manufacturer's values are also shown right next to them in Figure 3.5b. Note that these final values are computed for all possible averaging times, in contrast to the ones shown in Figure 3.4 which are only given for certain intervals of $2^n \tau_0$ seconds with $n = \{0, 1, \dots, 9\}$. Since the confidence intervals stay the same as depicted in Figure 3.4, they are neglected in Figure 3.5a.

The Jackson Labs CSAC exhibits WFM noise up to approximately one hour averaging time which is about 1.5 times less stable than the manufacturer's data indicate. It then subsequently transitions into FFM noise. The OCXO post-filter signal shows high short-term stability typical for such an oscillator. Its overall performance is comparable to the manufacturer's data. Furthermore, steering and adjusting of the OCXO to the CSAC module is visible after approximately 30 minutes. The Microsemi CSAC shows noise types similar to the Jackson Labs CSAC, but the WFM noise is smaller by about $5 \cdot 10^{-11}$. The flicker floor (FFM) begins after roughly three hours. Besides that, the performance is more than five times better than indicated by the manufacturer. The SRS PRS10 shows fluent transitions of the four different noise types starting with WPM/FPM noise up to approximately 20 s, then transitioning into WFM noise. Since the overlapping ADEV cannot distinguish between WPM and FPM noise, the modified ADEV is also depicted in Figure 3.4d. By taking a closer look at averaging times ranging from 1 s to 20 s, it can be seen that this interval consists of WPM noise up to 5 s and FPM thereafter with ADEV slopes of -1.5 and -1 , respectively. After approximately one hour averaging time, WFM noise is followed by a mixture

Table 3.3: Parameter values for the determination of time prediction errors of *atomic clocks under test*: upper limit of averaging times τ_L with sufficiently significant Allan deviation $\sigma_y(\tau_L)$, power law noise slope coefficient μ , values a , b , c of $\sigma_y(\tau = 1\text{ s})$ for white/flicker phase noise, white frequency noise and flicker frequency noise, respectively

Oscillator	τ_L [s]	$\sigma_y(\tau_L)$	a	b	c	μ
Jackson Labs CSAC	48,400	$2.056 \cdot 10^{-12}$	0	$8.867 \cdot 10^{-11}$	$2.380 \cdot 10^{-12}$	1
Jackson Labs OCXO	48,400	$2.137 \cdot 10^{-12}$	0	0	$2.441 \cdot 10^{-12}$	1
SRS PRS10	121,100	$2.917 \cdot 10^{-13}$	$1.547 \cdot 10^{-11}$	$2.481 \cdot 10^{-12}$	$2.500 \cdot 10^{-13}$	1
Microsemi CSAC	44,500	$4.547 \cdot 10^{-13}$	0	$4.074 \cdot 10^{-11}$	$5.949 \cdot 10^{-13}$	1

of FFM and RWFM noise, whereas the latter are not clearly separable from one another in a statistical sense because of the significantly increased confidence intervals for $\tau > 10^4$ s (cf. Figure 3.4d). All in all, it can be stated that the individual values agree well with the manufacturer's data.

By taking the GNSS observation noise from Figure 3.1 into account, maximum intervals for physically meaningful receiver clock modeling can be derived by means of the time prediction error according to Equation (3.1) using the values listed in Table 3.3. The corresponding time error curves are shown in Figure 3.6, individual values for maximum clock modeling intervals are given in Table 3.4. Thus, RCM is assumed to be feasible for intervals ranging from eleven minutes (Jackson Labs CSAC) to 2.36 hours (SRS PRS10) when using GPS L1 C/A-code observations. In case of L1 Doppler observations, even longer modeling periods of 33 minutes and more than a day are justified for the same respective oscillators. Due to the combined use of both observation types within the clock models of this thesis, the lower bounds defined by the code observations are used from this point on.

Fourier Analysis

The spectral characteristics of a clock can be investigated by means of a Fourier analysis of the frequency deviations. Here, the PSDs of the fractional frequency deviations $S_y(f)$ are computed based on *Welch's method* (Welch, 1967) using different window functions with varying lengths. More precisely, the one-second data are filtered by a Hamming window (Hamming, 1983) and the 100-second data by a Kaiser window (Kaiser, 1974) because of its decreased attenuation of the side lobes, i.e. lower Fourier

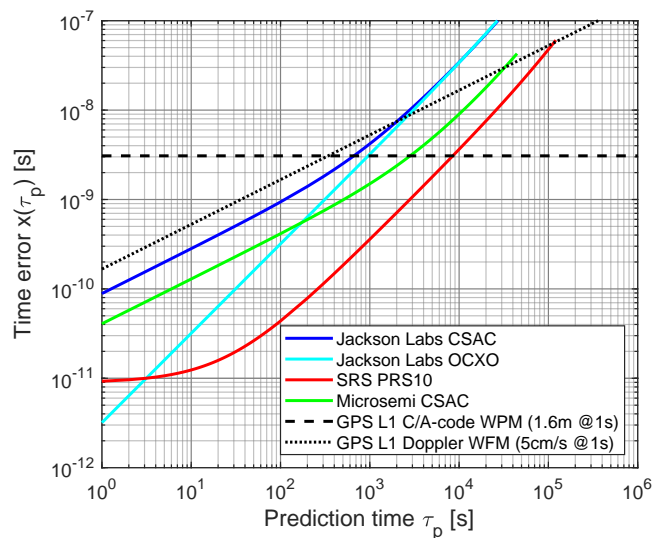


Figure 3.6: Time prediction errors of devices under test as well as GPS L1 C/A-code and Doppler observation noise modeled as white phase modulation and white frequency modulation noise, respectively

Table 3.4: Approximate maximum intervals for physically meaningful receiver clock modeling (RCM) of devices under test when using GPS L1 C/A-code and Doppler observations

Oscillator	Max. RCM interval with GPS L1	
	C/A-code [s]	Doppler [s]
Jackson Labs CSAC	660	2000
Jackson Labs OCXO	960	2600
SRS PRS10	8500	114,500
Microsemi CSAC	2800	32,460

frequencies. Similar to the ADEV curves shown in Figure 3.5a, the underlying noise process types can be directly derived from the PSD curves shown in Figure 3.7 by means of Figure 2.6c. Therefore, different window lengths are applied in order to identify these noise processes by their distinct slopes more clearly. However, care has to be taken not to smooth or deform the PSD estimates in a way that leads to misinterpretations of the spectral clock behavior. The measurement intervals of 1 s and 100 s of the fractional frequency deviations yield cut-off Fourier frequencies of 0.5 Hz and 0.005 Hz, respectively. The noise process types derived from the individual ADEV curves are visible especially distinct inside the strongly filtered PSDs depicted by dark colors in Figure 3.7.

Again, both CSAC signals show almost exclusively WFM noise. The jump in frequency stability around $\tau = 100$ s of the Jackson Labs OCXO already discussed based on Figure 3.4b reflects in the range of the 10^{-3} Hz frequencies of the PSD estimates. Furthermore, FFM and RWFM noise are clearly visible by their characteristic slopes of -1 and -2 , respectively, whereas WFM noise only appears for low Fourier frequencies of 0.1 Hz to 0.5 Hz. The predominant noise process in the SRS PRS10 data is WFM noise which corresponds to the mid-term frequency stability present in the ADEV curves (cf. Figure 3.4d). However, its short-term stability, i.e. high Fourier frequencies, also shows behavior of WPM and FPM noise with slopes of 2 and 1, respectively, in addition to long-term FFM noise, that is low Fourier frequencies,. In summary, the spectral analysis results confirm the ones from time-domain analysis.

In order to use this information as adequate input data in a Kalman filter, the h_α -coefficients are estimated by means of an unweighted least-squares adjustment from the PSD estimates of the fractional frequency deviations $S_y(f)$ according to Equation (2.76), based on the functional relationship

$$S_y(f) = h_{-2}f^{-2} + h_{-1}f^{-1} + h_0 + h_1f + h_2f^2. \quad (3.3)$$

Due to the fact that the h_α -coefficients are very small – in the range of 10^{-20} to 10^{-30} – the parameters are scaled by the nominal frequency of the oscillators ν_0 for reasons of numerical stability: $\bar{h}_\alpha = \nu_0 h_\alpha$. Thus, parameter vector

$$\mathbf{x} = [\bar{h}_{-2} \quad \bar{h}_{-1} \quad \bar{h}_0 \quad \bar{h}_1 \quad \bar{h}_2]^T \quad (3.4)$$

is estimated with its cofactor matrix

$$\hat{\mathbf{x}} = \mathbf{Q}_{\hat{\mathbf{x}}\hat{\mathbf{x}}} \mathbf{A}^T \mathbf{1}, \quad (3.5)$$

$$\mathbf{Q}_{\hat{\mathbf{x}}\hat{\mathbf{x}}} = (\mathbf{A}^T \mathbf{A})^{-1}, \quad (3.6)$$

and design matrix

$$\mathbf{A} = \nu_0^{-1} \begin{bmatrix} f_1^{-2} & f_1^{-1} & 1 & f_1 & f_1^2 \\ \vdots & \vdots & \vdots & \vdots & \vdots \\ f_n^{-2} & f_n^{-1} & 1 & f_n & f_n^2 \end{bmatrix}, \quad (3.7)$$

containing n Fourier frequencies f , and observation vector

$$\mathbf{I} = \left[S_y(f_1) \quad \dots \quad S_y(f_n) \right]^T. \quad (3.8)$$

More precisely, the strongly filtered values of $S_y(f)$ are used because of their significantly reduced noise characteristics as can be seen from Figure 3.7. The a posteriori parameter standard deviations s_{h_α} are given with respect to Equation (2.28) by the VCM of the estimated parameters

$$\mathbf{C}_{\hat{x}\hat{x}} = \hat{\sigma}_0^2 \mathbf{Q}_{\hat{x}\hat{x}} = \begin{bmatrix} s_{h_{-2}}^2 & \dots & s_{h_{-2}h_2} \\ \vdots & \ddots & \vdots \\ s_{h_2h_{-2}} & \dots & s_{h_2}^2 \end{bmatrix}. \quad (3.9)$$

Both \hat{x} and $\mathbf{C}_{\hat{x}\hat{x}}$ must be scaled by v_0 and v_0^2 , respectively, to obtain the values as listed in Table 3.5.

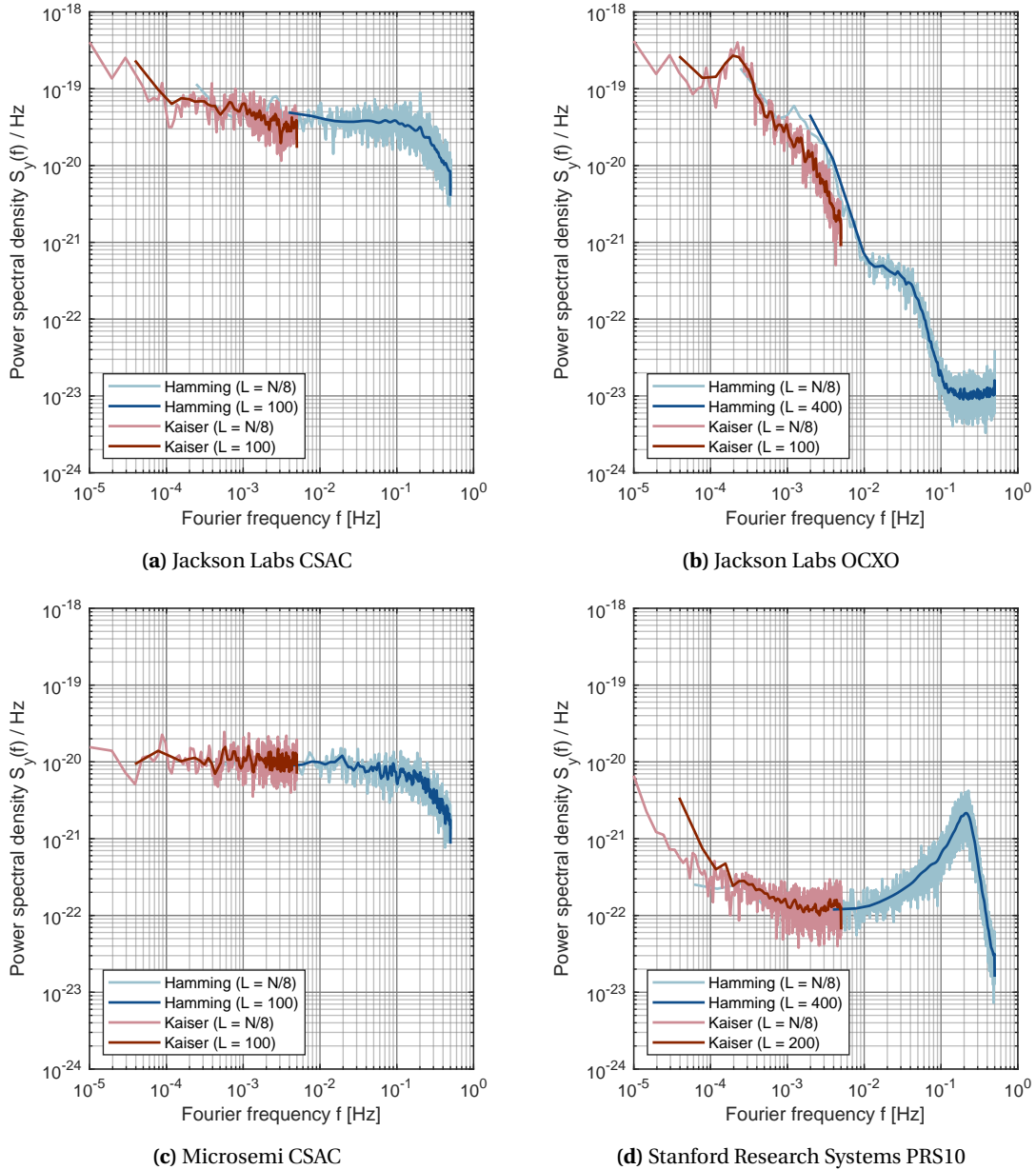


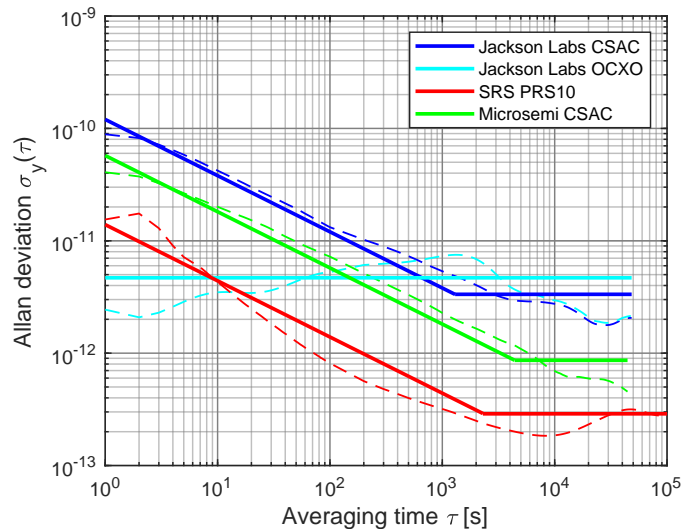
Figure 3.7: Power spectral densities of devices under test of 1 s (blue) and 100 s (red) data of fractional frequency deviations (no. of samples N) and different windows (Hamming, Kaiser) and window length L

Table 3.5: Power spectral density coefficients h_α and standard deviations (1σ) of atomic clocks under test

Oscillator	h_0 [s]	s_{h_0} [s]	h_{-1} [-]	$s_{h_{-1}}$ [-]
Jackson Labs CSAC	$2.888 \cdot 10^{-20}$	$0.075 \cdot 10^{-20}$	$8.046 \cdot 10^{-24}$	$0.368 \cdot 10^{-24}$
Jackson Labs OCXO	–	–	$1.584 \cdot 10^{-23}$	$0.063 \cdot 10^{-23}$
SRS PRS10	$3.877 \cdot 10^{-22}$	$0.367 \cdot 10^{-22}$	$6.010 \cdot 10^{-26}$	$1.792 \cdot 10^{-26}$
Microsemi CSAC	$6.582 \cdot 10^{-21}$	$0.175 \cdot 10^{-21}$	$5.386 \cdot 10^{-25}$	$1.048 \cdot 10^{-25}$

In order to avoid over-parametrization of the adjustment model, not all coefficients are estimated for each oscillator, but only the ones identified visually as discussed in the preceding paragraph. Note that in case of the SRS PRS10, besides the FFM coefficient only the one for WFM is estimated for two reasons: (a) WFM, WPM and FPM coefficients cannot be separated properly from each other, (b) WFM noise is the predominant short-term and mid-term noise process in this case, which is typical for a rubidium frequency standard (Riehle, 2004). This also applies to the Jackson Labs OCXO in a sense that FFM and RWFM noise are not completely distinguishable from one another, as shown in Figures 3.4 and 3.7. In addition, steering towards the CSAC signal leads to WFM-like noise contributions for $\tau \geq 2,000$ s. Therefore, only the FFM coefficient is estimable.

The resulting PSD coefficients are converted to Allan deviations according to the equations given in Table 2.1, and depicted together with the original overlapping ADEVs in Figure 3.8. A good agreement between the original and the PSD-derived curves is clearly visible. Furthermore, since the standard deviations of all estimated h_0 -coefficients (WFM) are at least one order of magnitude smaller than the respective parameter, the latter can be considered significant. In case of the h_{-1} -coefficients (FFM) this solely applies to both Jackson Labs oscillators. The uncertainties of the SRS PRS10 and the Microsemi CSAC are only about four to five times smaller than the respective parameter estimate. There are two reasons for this: (a) the Microsemi CSAC does not show that a distinct FFM noise behavior than both Jackson Labs oscillators, especially the OCXO (cf. Figure 3.7); (b) the different noise processes inside the SRS PRS10 signal at hand are, in general, not as clearly separable as in case of the other oscillators, thus their estimability becomes more difficult. However, assuming that these values are normally distributed, they can still be considered significant according to the *three-sigma rule of thumb* associated with a confidence level of 99.7%.

**Figure 3.8:** Original overlapping Allan deviations (dashed lines) and Allan deviations derived from estimated power spectral density coefficients h_α (solid lines) of devices under test

3.3 Implementations in Data Analysis

The different concepts of receiver clock modeling are implemented inside an LKF and an SLSA sharing the same *MATLAB* source code developed by the author of this thesis. This algorithm uses multi-GNSS code and Doppler observations. Further information on the software can be found in section 4.1. In this section, the Kalman filter implementations are discussed in section 3.3.1 first. Additionally, and more importantly, a new real-time applicable approach of RCM based on a sequential least-squares adjustment is proposed in section 3.3.2, where the receiver clock biases are modeled by means of a piecewise linear polynomial. Extensive practical evaluations and validations of these concepts will follow in chapter 4. Note that, since only receiver-related parameters are estimated, subscripts i and A used in section 2.1.2 are omitted in the following.

3.3.1 Linearized Kalman Filter

An extended or linearized Kalman filter is typically applied in kinematic GNSS analysis because of its computationally efficient combination of GNSS measurements and a system dynamics model on an epoch-by-epoch basis. These epochs can be coupled or augmented, respectively, by means of appropriate process noise models. Therefore, in order to introduce the knowledge about the oscillator frequency stability, RCM is applied by using a proper model for the clock-related process noise. With this in mind, the overall filter design in this thesis is introduced first, followed by a more detailed description of the clock model.

The state vector in multi-GNSS PVT estimation at a given epoch $k = \{1, 2, \dots, p\} \in \mathbb{N}$ reads

$$\mathbf{x}_k = \begin{bmatrix} \mathbf{x}_{cv,k} \\ \mathbf{x}_{isb,k} \\ \mathbf{x}_{clk,k} \end{bmatrix}, \quad (3.10)$$

with geocentric Cartesian coordinates and velocities

$$\mathbf{x}_{cv,k} = \begin{bmatrix} X & V_X & Y & V_Y & Z & V_Z \end{bmatrix}^T, \quad (3.11)$$

ISB time and frequency offset

$$\mathbf{x}_{isb,k} = \begin{bmatrix} \delta_{ISBT} & \delta_{ISBF} \end{bmatrix}^T, \quad (3.12)$$

and receiver clock biases accounting for time and frequency offset

$$\mathbf{x}_{clk,k} = \begin{bmatrix} \delta t & \delta f \end{bmatrix}^T. \quad (3.13)$$

During the prediction step of each filter recursion, the current system state and its cofactor matrix are propagated to the next epoch according to Equations (2.67) and (2.68) by state transition matrix

$$\Phi_{k,k+1} = \mathbf{I}_{[5 \times 5]} \otimes \begin{bmatrix} 1 & \Delta t \\ 0 & 1 \end{bmatrix}, \quad (3.14)$$

where \otimes denotes the Kronecker product (Steeb, 1991) and $\Delta t = t_{k+1} - t_k$ is the time interval between two consecutive epochs – which typically but not necessarily coincides with the GNSS observation sampling interval. In kinematic applications, sampling interval Δt typically ranges between 0.05 s (20 Hz) and 1 s depending on the underlying system dynamics. Due to the shape of state transition

matrix Φ , each coordinate-velocity as well as ISB and clock time-frequency offset pair, respectively, is modeled as a *random ramp* process (Gelb et al., 1974):

$$x_{1,k+1} = x_{1,k} + x_{2,k} \Delta t + \omega_{1,k}, \quad (3.15a)$$

$$x_{2,k+1} = x_{2,k} + \omega_{2,k}, \quad (3.15b)$$

which basically reflects the linear dependence of two states x_1 , x_2 when propagated from epoch k to epoch $k + 1$ and their respective uncertainties within the limits of uncorrelated noise ω_1 , ω_2 , that is process noise. To be exact, Equation (3.15a) represents the random ramp processes of the respective coordinate, ISB and clock time offset states. Equation (3.15b) denotes the *random walk* processes of the respective velocity, ISB and clock frequency offset states. The reason for this is that both coordinates and time offsets are modeled as integrated velocities and frequency offsets, respectively. Hence, a two-state clock model should be applied in GNSS PVT estimation to appropriately account for the frequency stability of the oscillator in use.

The growth of the uncertainty of state vector \mathbf{x}_k is reflected and bounded by process noise matrix

$$\mathbf{Q}_{\omega\omega} = \begin{bmatrix} \mathbf{Q}_{\omega\omega,cv} & 0 & 0 \\ 0 & \mathbf{Q}_{\omega\omega,clk} & 0 \\ 0 & 0 & \mathbf{Q}_{\omega\omega,isb} \end{bmatrix}, \quad (3.16)$$

composed of three submatrices for coordinates and velocities $\mathbf{Q}_{\omega\omega,cv}$, originally defined in a local north-east-up (NEU) frame – and subsequently converted to geocentric Cartesian values –,

$$\mathbf{Q}_{\omega\omega,cv,NEU} = \text{diag}(50 \text{ m}, 25 \text{ m/s}, 50 \text{ m}, 25 \text{ m/s}, 5 \text{ m}, 2.5 \text{ m/s})^2, \quad (3.17)$$

as well as inter-system biases

$$\mathbf{Q}_{\omega\omega,isb} = \begin{bmatrix} 300 \text{ m} & 0 \\ 0 & 30 \text{ m/s} \end{bmatrix}^2 \approx \begin{bmatrix} 1 \mu\text{s} & 0 \\ 0 & 0.1 \mu\text{s/s} \end{bmatrix}^2 \quad (3.18)$$

and receiver clock biases

$$\mathbf{Q}_{\omega\omega,clk} = \begin{bmatrix} 3,000 \text{ m} & 0 \\ 0 & 300 \text{ m/s} \end{bmatrix}^2 \approx \begin{bmatrix} 10 \mu\text{s} & 0 \\ 0 & 1 \mu\text{s/s} \end{bmatrix}^2. \quad (3.19)$$

Matrices $\mathbf{Q}_{\omega\omega,cv}$, $\mathbf{Q}_{\omega\omega,isb}$ and $\mathbf{Q}_{\omega\omega,clk}$ contain rather relaxed values so that the respective predicted states have a negligible impact on the filtered solution during the measurement update step as described in section 2.2.2. Moreover, Equation (3.19) represents the cases in this thesis in which *no receiver clock modeling* is applied. The main reason for this is that differences between the filter solutions with and without RCM shall be solely attributable to the different clock process noise models applied. Thus, the LKF solution applying Equations (3.17) and (3.19) is virtually equivalent to a pure least-squares solution based on (GNSS) measurements only. Note that if a so-called *millisecond clock jump* is detected the same large amount of noise is added by $\mathbf{Q}_{\omega\omega,clk}$ as during filter initialization.

With this in mind, physically meaningful receiver clock modeling in a Kalman filter can be applied by defining $\mathbf{Q}_{\omega\omega,clk}$ with the spectral amplitudes S_t and S_f of the respective time/phase and frequency deviations of the clock in use. Integrated over a certain time period Δt with respect to the laws of error propagation, the time-discrete clock process noise can generally be described as

$$\mathbf{Q}_{\omega\omega,clk} = \begin{bmatrix} S_t \Delta t + S_f \frac{\Delta t^3}{3} & S_f \frac{\Delta t^2}{2} \\ S_f \frac{\Delta t^2}{2} & S_f \Delta t \end{bmatrix} \quad (3.20)$$

according to Brown and Hwang (1997), who also give approximations for the determination of the spectral amplitudes that depend on the PSD h_α -coefficients described in the preceding section:

$$S_t = \frac{h_0}{2}, \quad (3.21)$$

$$S_f = 2\pi^2 h_{-2}. \quad (3.22)$$

Obviously, this clock model does only account for WFM and RWFM noise but not for a FFM noise component in the oscillator. The major problem with flicker noise is that it cannot be modeled exactly by a finite-order state model, thus it is either completely neglected, as in the case of Equations (3.21) and (3.22), or approximated, like e.g., by the model of Dierendonck et al. (1984):

$$\mathbf{Q}_{\omega\omega, \text{clk}} = \begin{bmatrix} h_0 \frac{\Delta t}{2} + h_{-1} 2\Delta t^2 + h_{-2} \frac{2\pi^2 \Delta t^3}{3} & h_{-1} \Delta t + h_{-2} \pi^2 \Delta t^2 \\ h_{-1} \Delta t + h_{-2} \pi^2 \Delta t^2 & h_0 \frac{1}{2\Delta t} + 4h_{-1} + h_{-2} \frac{8\pi^2 \Delta t}{3} \end{bmatrix}. \quad (3.23)$$

Note that the model given in the original paper by Dierendonck et al. (1984) has some flawed terms that were corrected by Brown and Hwang (1997). Therefore, Equation (3.23) contains the improved terms according to the latter reference.

Since the oscillators investigated in this thesis exhibit distinct FFM noise but no RWFM components (cf. section 3.2.2), the model according to Equation (3.23) is used in kinematic GNSS data analysis later on. It is derived by the authors analytically from the impulse responses $h(t)$ of the respective WFM, FFM and RWFM noise processes. The model uses an approximation for FFM noise by bounding it to a certain frequency range since $h(t)$ is infinite for $t = 0$ in this particular case. In the absence of a RWFM coefficient h_{-2} (cf. Table 3.5), Equation (3.23) becomes

$$\mathbf{Q}_{\omega\omega, \text{clk}} = \begin{bmatrix} h_0 \frac{\Delta t}{2} + h_{-1} 2\Delta t^2 & h_{-1} \Delta t \\ h_{-1} \Delta t & h_0 \frac{1}{2\Delta t} + 4h_{-1} \end{bmatrix}. \quad (3.24)$$

Conclusively, it is worth mentioning that white and flicker phase noise (h_2, h_1) are not accounted for by the presented clock process noise model since this is taken care of by means of the measurement noise model in a Kalman filter (Dierendonck et al., 1984).

3.3.2 Sequential Least-squares Adjustment

Modeling Approach

The basic idea of least-squares clock modeling originates from very-long-baseline interferometry (VLBI), where observation data of remote hydrogen masers are typically synchronized by means of a second-order polynomial in 24-hour batch processing (Felli and Spencer, 1989). This concept was adopted by Weinbach (2013), extended to a flexible piecewise linear approach in order to account for sub-daily clock variations in high-precision GPS data analysis, and successfully applied to IGS stations equipped with a hydrogen maser in static and pseudo-kinematic PPP. Therefore, this approach is chosen for the purposes of this thesis, that is the application and proper modeling of the behavior of miniature atomic clocks in GNSS navigation. This requires a real-time applicable implementation of a piecewise linear polynomial because the observation data cannot be processed in one batch since they arise in a sequential way. Thus, processing of such data is typically referred to as *sequential least-squares adjustment (SLSA)*.

In comparison to a pure epoch-by-epoch solution, observations of a new epoch are added to the already existing adjustment model from previous epochs. Such an approach increases the redundancy of the estimation process and strengthens its accuracy and reliability since the parameter vector stays

unchanged. Therefore, classical SLSA is usually not applicable in navigation applications because of the ever-changing nature of the parameter vector, for example in regards to the coordinate and velocity estimates. That is why a mixture of an epochwise and a sequential approach is proposed to enable RCM in a least-squares adjustment. To be exact, epoch-specific parameters such as coordinates and velocities are estimated epoch-by-epoch, whereas clock parameters are estimated by means of an epoch-spanning piecewise linear polynomial bounded by the clock-specific maximum modeling interval. Thus, the coefficients of the polynomial are updated by the GNSS observations of each new epoch instead of being estimated completely anew.

Due to the sequential part of the proposed approach, *one* overall parameter vector can be designated for the whole adjustment process with regard to Equations (3.11) and (3.12):

$$\mathbf{x} = \begin{bmatrix} \mathbf{x}_{\text{cvi},1} \\ \mathbf{x}_{\text{cvi},2} \\ \vdots \\ \mathbf{x}_{\text{cvi},r-1} \\ \mathbf{x}_{\text{cvi},r} \\ \mathbf{b} \end{bmatrix}, \quad (3.25)$$

where coordinate, velocity and ISB parameters of epoch k are summarized in

$$\mathbf{x}_{\text{cvi},k} = \begin{bmatrix} \mathbf{x}_{\text{cv},k} \\ \mathbf{x}_{\text{isb},k} \end{bmatrix}. \quad (3.26)$$

The receiver clock time and frequency offsets δt_k , δf_k of the current epoch t_k are modeled by means of piecewise linear clock segments:

$$\delta t_{k,m} = b_0 + \left(\sum_{i=1}^{m-1} b_i \Delta t_{\text{rcm}} \right) + b_m (t_k - t_{0,m}), \quad (3.27a)$$

$$\delta f_{k,m} = b_m, \quad (3.27b)$$

with segment index $m = \lfloor t_k / \Delta t_{\text{rcm}} \rfloor + 1$, clock modeling interval Δt_{rcm} , initial time offset b_0 , frequency offsets b_i of the previous segments with $i = \{1, 2, \dots, m-1\} \in \mathbb{N}$, and segment starting time

$$t_{0,m} = \begin{cases} 0 & \text{if } t_k \leq \Delta t_{\text{rcm}}, \\ (m-1) \Delta t_{\text{rcm}} & \text{if } t_k > \Delta t_{\text{rcm}}. \end{cases} \quad (3.28)$$

All clock coefficients b_m are assembled in vector \mathbf{b} in Equation (3.25). Since these clock parameters are estimated in a cumulative way, the number of clock parameters increases with each new modeling segment, as can be seen from Equations (3.27a) and (3.27b) as well as Figure 3.9. Although this is a computationally rather demanding approach, it is the only real-time applicable one. In order to

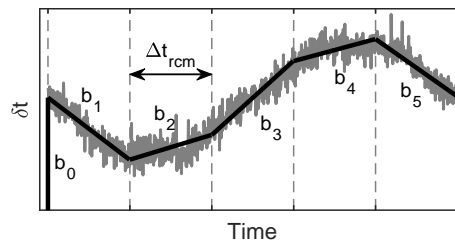


Figure 3.9: Schematic concept of piecewise linear modeling with constrained interval boundaries using the example of clock bias δt and clock modeling interval Δt_{rcm} over time t

account for a quadratic term, i.e. frequency drift, two options are available: (a) the clock modeling interval is reduced and/or (b) constraints on the slopes of consecutive clock segments are imposed.

This approach of clock modeling can also be applied to the ISB estimates since their temporal behavior. In the context of this thesis, this is referred to as inter-system bias modeling (ISBM). On the one hand, system-specific corrections for ISB offset and drift are typically provided by the GNSS operator for the duration of one day, e.g. via satellite navigation message (Montenbruck and Hauschild, 2013). On the other hand, receiver-specific ISBs should be very stable over time (Gioia and Borio, 2016).

Constraining of Clock Parameters

In order to avoid jumps or too loose transitions at the boundaries of consecutive clock segments, their respective slopes b_m can be constrained with respect to the frequency stability of the oscillator in use. The underlying pseudo-observation is defined according to Equations (2.48a) and (2.48b) as

$$0 + v_{\text{clk}} = b_{i+1} - b_i, \quad (3.29a)$$

$$\mathbf{Q}_{\text{clk}} = \sigma_{\text{clk}}^2, \quad (3.29b)$$

with $i = \{1, \dots, m-1\} \in \mathbb{N}$ and σ_{clk} being derived from the temporal stability of the oscillator in use, in this case according to the values shown in Figure 3.6. More precisely, the *tightness* or strength, respectively, of the constraint is computed based on the time prediction error $x(\tau_p)$ evaluated at the length of the clock modeling interval $\tau_p = \Delta t_{\text{rcm}}$:

$$\sigma_{\text{clk}} = \frac{x(\Delta t_{\text{rcm}})}{\sqrt{\Delta t_{\text{rcm}}}}, \quad (3.30)$$

where modeling interval Δt_{rcm} can either be fixed to the theoretical maximum value or determined adaptively as will be discussed in the next paragraph.

Clock Modeling Hypothesis Test

Another problem when applying a piecewise linear clock polynomial is the fact that it cannot appropriately account for quadratic behavior, i.e. frequency drifts. Therefore, a conventional single-epoch snapshot solution is computed in parallel to the sequential parameter estimation. Due to the fact that the SLSA piecewise linear clock polynomial follows these independent clock estimates, the latter can be used to decide if and when a new clock segment has to be started. In order to do so, the snapshot estimates are tested for a quadratic term each epoch by means of regression analysis. Based on the (centered) independent clock biases δt_k corresponding to clock modeling segment m , a quadratic polynomial

$$\delta t_k = a_0 + a_1 (t_k - t_{0,m}) + a_2 (t_k - t_{0,m})^2 \quad (3.31)$$

with coefficients a_0 , a_1 , a_2 for time offset, frequency offset and frequency drift, respectively, is estimated as described in section 2.2.1 according to Equation (2.24). At this point, the weight matrix is defined using the independent epochwise variances of δt_k in order to account for changes in the observation geometry. Subsequently, the estimated quadratic coefficient \hat{a}_2 is tested for significance against its standard deviation $\hat{\sigma}_{\hat{a}_2}$ by means of a two-sided hypothesis test. Given a certain significance level η and the Student's t -distribution, test statistic \mathcal{T} can be computed:

$$\mathcal{T} = \frac{\hat{a}_2}{\hat{\sigma}_{\hat{a}_2}} \sim t_{n-3, 1-\eta/2}, \quad (3.32)$$

with the number of independent clock bias estimates n . The null and alternative hypotheses H_0 and H_A , respectively, read

$$H_0: E\{\hat{a}_2\} = 0, \quad (3.33)$$

$$H_A: E\{\hat{a}_2\} \neq 0. \quad (3.34)$$

If H_0 is rejected, a new clock segment is started, because a significant frequency drift has been detected. Due to a certain convergence time of the polynomial coefficients at the beginning of each modeling segment, this hypothesis test is first applied after a given latency time of 30 seconds. This waiting time is also justified due to the fact that an atomic clock typically does not suffer from such a severe frequency drift that makes the start of new clock segments necessary earlier than those 30 seconds.

Thanks to this approach, piecewise linear clock modeling can adapt to a potential oscillator frequency drift and variations of it, for example due to changes of ambient temperature. This is especially beneficial if such a drift occurs well before the maximum modeling interval. Without the proposed hypothesis test, mismodeling of the clock behavior would ultimately lead to biased estimates of vertical coordinates and velocities as will be shown in section 4.3. Nevertheless, a maximum interval should still be defined so that clock modeling is not applied beyond physical meaningfulness.

Parameter Pre-elimination

Since only the parameters of the current epoch are of interest in a real-time application, parameter vector \mathbf{x} as defined by Equation (3.25) is split into parameters to be pre-eliminated \mathbf{x}_e , i.e. estimated implicitly, and parameters of interest \mathbf{x}_g that are estimated explicitly:

$$\mathbf{x}_e = \begin{bmatrix} \mathbf{x}_{cvi,1} \\ \vdots \\ \mathbf{x}_{cvi,r-1} \end{bmatrix}, \quad (3.35)$$

$$\mathbf{x}_g = \begin{bmatrix} \mathbf{x}_{cvi,r} \\ \vdots \\ \mathbf{b} \end{bmatrix}. \quad (3.36)$$

Thus, the coordinate, velocity and ISB estimates are pre-eliminated and the clock parameters are kept for explicit estimation. Accordingly, the full design matrix of epoch $k = \{1, 2, \dots, r', \dots, r\} \in \mathbb{N}$ and modeling segment $m = \{1, 2, \dots, q\} \in \mathbb{N}$ is composed of submatrices \mathbf{A}_e and \mathbf{A}_g :

$$\mathbf{A}_{k,m} = \begin{bmatrix} \mathbf{A}_{cvi,1,1} & \mathbf{0} & \dots & \mathbf{0} & \mathbf{0} & \dots & \mathbf{0} & \mathbf{0} & \mathbf{A}_{clk,1,1} \\ \mathbf{0} & \mathbf{A}_{cvi,2,1} & \dots & \mathbf{0} & \mathbf{0} & \dots & \mathbf{0} & \mathbf{0} & \mathbf{A}_{clk,2,1} \\ \vdots & \vdots & \ddots & \vdots & \vdots & \ddots & \vdots & \vdots & \vdots \\ \mathbf{0} & \mathbf{0} & \dots & \mathbf{A}_{cvi,r',1} & \mathbf{0} & \dots & \mathbf{0} & \mathbf{0} & \mathbf{A}_{clk,r',1} \\ \mathbf{0} & \mathbf{0} & \dots & \mathbf{0} & \mathbf{A}_{cvi,r'+1,2} & \dots & \mathbf{0} & \mathbf{0} & \mathbf{A}_{clk,r'+1,2} \\ \vdots & \vdots & \ddots & \vdots & \vdots & \ddots & \vdots & \vdots & \vdots \\ \mathbf{0} & \mathbf{0} & \dots & \mathbf{0} & \mathbf{0} & \dots & \mathbf{A}_{cvi,r-1,q} & \mathbf{0} & \mathbf{A}_{clk,r-1,q} \\ \mathbf{0} & \mathbf{0} & \dots & \mathbf{0} & \mathbf{0} & \dots & \mathbf{0} & \mathbf{A}_{cvi,r,q} & \mathbf{A}_{clk,r,q} \end{bmatrix}. \quad (3.37)$$

$\underbrace{\hspace{15em}}_{\mathbf{A}_e} \quad \underbrace{\hspace{10em}}_{\mathbf{A}_g}$

For reasons of clarity, epoch identifier k and clock segment identifier m are colored in red and blue, respectively. All further formulae can be found in section 2.2.1 given by Equations (2.40) to (2.44).

Sliding Window

Due to the fact that the computational demand increases over time in an SLSA, even though parameter pre-elimination is applied, the maximum "memory length" of the estimator can be safely restricted to the theoretical maximum clock modeling interval. This can be done by means of a sliding window so that only a certain number of epochs preceding the current epoch are kept in the estimation process. However, if the temporal length of the sliding window has to be set shorter than the intended clock modeling interval, the latter is automatically restricted to the window length. This is, for example, the case in section 4.4, where the real-time applicability of the approach of RCM proposed in this section is investigated by means of a software-defined radio (SDR).

4

Application Examples and Case Studies

This chapter is dedicated to the practical evaluation and validation of the proposed concepts of receiver clock modeling by means of various kinematic case studies. The core of these investigations is a series of vehicle test drives reviewed in section 4.3, where the impact and limitations of clock modeling are discussed. The real-time applicability of the proposed approach of RCM in an SLSA is demonstrated in section 4.4. A potential application of a CSAC in a spoofing detection scheme is presented in section 4.5. Note that parts of these practical applications are based on the author's contributions Krawinkel and Schön (2015) and Krawinkel and Schön (2016b). In order to evaluate the performance of RCM, typical GNSS quality parameters are introduced in section 4.2. However, first, the software module developed within the scope of this thesis is reviewed.

4.1 Observation Modeling in Single Point Positioning

All GNSS data analysis in this chapter, that is PVT estimation using GPS and GLONASS L1 C/A-code and Doppler observations, is based on a single point positioning (SPP) algorithm, which is implemented inside a post-processing *GNSS MATLAB Toolbox* developed by the Institut für Erdmessung (IfE) since the late 2000s. This enables full control over the whole data processing chain. Although the SPP routine is designed similarly to the conventional GPS navigation solution (GPS Directorate, 2006), IGS final orbit products are applied instead of broadcast ephemeris (cf. section 2.1.4). The main reason for this is the fact that the latter do not account for inter-system biases, which makes multi-GNSS much more challenging. Thus, products provided by the IGS analysis center European Space Operations Centre (ESOC) located at ESA in Darmstadt, Germany are used in the following if not indicated otherwise. This approach consequently leads to further adaptations of data processing in order to stay consistent with the ESOC analysis strategy (ESOC, 2018). Therefore, the models applied are briefly discussed hereinafter. For further information it is referred to the literature as referenced.

GNSS *satellite orbit and clock corrections* are made available by the IGS and its analysis centers. It can be distinguished between orbit products comprising satellite positions *and* clock corrections as well as clock products solely containing clock corrections but being fully consistent with the aforementioned orbits. Orbit products typically have a temporal spacing of 15 minutes, whereas clock products are mostly given for intervals of 30 seconds or less. The main reason for this is the reduction of interpolation errors for the user, which is mostly critical in high-precision applications (Montenbruck et al., 2005; Bock et al., 2009). Therefore, only orbit products are used in this thesis since centimeter-accuracy of the satellite clock corrections is not required. The accuracies of the most precise final orbit and clock products amount to approximately 25 mm and 75 ps RMS (IGS, 2018). The ACs typically provide a consistent product for GPS and at least one more satellite system, in most cases GLONASS, whereas a combination of these individual AC products is only computed for GPS. One product comprising all currently available systems is generated by the *Multi-GNSS Pilot Project*. However, since systems like BDS, Galileo and QZSS are not fully established yet and due to the lack of a convention on how to

consistently handle inter-system and intra-system biases, these products do not have the same level of maturity and sophistication as the GPS+GLONASS products (Montenbruck et al., 2017).

Interpolation of satellite positions, velocities and clock corrections between the given orbit intervals can be carried out by means of a polynomial or numerical integration. Due to daily boundary jumps of the orbit products, numerical integration is the preferred method. This is admittedly more consistent with the AC analysis strategy, but only as long as the integrator applies the same models as the AC. In case a polynomial interpolation approach is used, for example based on Lagrange or Newton polynomials, orbits of the preceding and subsequent day also have to be applied if observation data of a whole day are being processed. Thereby, the increased interpolation errors at the start and the end of the polynomial are shifted out of the observation period. This, however, has the disadvantage of interpolating across daily boundary jumps. For the purposes of this thesis and the SPP routine in general, it is sufficient to use a polynomial approach using a Newton polynomial of ninth degree. Since also receiver velocities shall be estimated in data analysis, the necessary satellite velocities are derived by temporal first-order central differencing of interpolated satellite positions. Note that the satellite coordinates of the IGS orbits are given for the center of mass of each space vehicle, but the satellite signals as recorded by a receiver refer to the satellite antenna phase center. These offsets are accounted for by the values given in the official IGS antenna file currently valid (Rothacher and Schmid, 2010).

The ranging signals transmitted by each GNSS satellite are generated by different circuits on board the space vehicle, thus they suffer from different delays which also slowly vary over time. Correction of these delays is crucial in pseudorange-based PVT and ionospheric modeling (Hernández-Pajares et al., 1999). Since all IGS orbits for GPS and GLONASS refer to the ionosphere-free LC of the precise codes on L1 and L2 frequencies (P1, P2), the user has to either apply the same observation type or correct the chosen one. If a receiver provides only C/A-code (C1) and no P1 observations – mainly because the latter are encrypted and only sophisticated geodetic receivers can track them –, the difference of P1-C1 has to be accounted for. Furthermore, in single-frequency PVT also the difference of P1-P2 has to be considered. These delays can only be determined in an absolute sense by calibration, which is not possible for in-orbit satellites. Therefore, they have to be estimated relative to each other, which is why they are called *differential code biases (DCBs)*. This singularity can be removed by applying e.g. a zero-mean condition in DCB determination. In consistence with the ESOC analysis strategy, the monthly DCB estimates of the Center for Orbit Determination in Europe (CODE) are applied in the SPP algorithm. The correction typically amounts to maximum/minimum values of ± 30 ns (9 m). Note that in the advent of new GNSS and the modernization of GPS and GLONASS, new signal modulations are introduced, which already was accounted for by introducing a new receiver independent exchange (RINEX) format version 3 (Gurtner and Estey, 2007). Since this leads to more DCBs, new methods for the determination of the already existing ones together with the new ones are developed in the MGEX framework. Two different DCB products are presently provided by the German Aerospace Center (DLR) and the Institute of Geodesy and Geophysics of the Chinese Academy of Sciences in Wuhan, China (Montenbruck et al., 2014; Wang et al., 2016).

GNSS signals received by a Earth-bound user are always subject to the effects of special and general relativity (Einstein, 1905b; Einstein, 1905a; Einstein, 1916) because they (a) move at high velocity relative to each other, and (b) are located at different levels of (the Earth's) gravitational potential. Although both effects counteract each other, the impact of general relativity is larger than that of special relativity. The corresponding effect on GNSS signals is accounted for by means of two components. A constant relative frequency offset is already applied to the fundamental frequency on board a satellite, which in case of GPS amounts to $-4.4647 \cdot 10^{-10}$. Since GNSS satellites move in slightly different non-circular orbits, a periodic correction must be applied that amounts to a maximum of ca. 23 ns for an orbit eccentricity of 0.01 (Ashby, 2003). In case of GPS, this has to be done by the user, whereas for GLONASS it is already incorporated into the broadcast satellite clock correction. The conventional GPS *relativistic correction* (GPS Directorate, 2006) was adopted by the IGS for *all* GNSSs and is therefore

applied in the SPP algorithm at hand. Note that, since a satellite does not circle the Earth in a perfect elliptic orbit, the conventional correction induces a periodic error in the range of the precision of current IGS satellite clock corrections of less than 1 ns RMS (IGS, 2018). This can be accounted for by an additional improved relativistic correction (Kouba, 2004). However, since the latter is not yet adopted by the IGS and its analysis centers, it should not be applied by the user of IGS products, especially in case of high-precision and/or clock modeling applications. The secondary relativistic effect also known as *Shapiro effect*, is neglected in this thesis regarding its maximum induced range error of less than 20 mm (Hofmann-Wellenhof et al., 2008).

The *ionospheric refraction* is caused by free electrons, that is the total electron content (TEC), in the upper atmosphere layers approximately 50 km to 1000 km above ground. The corresponding signal delay – or advance in case of phase observations – mainly depends on the time of day, the Earth's magnetic field, the solar activity and can amount to more than 100 m at times of high ionospheric activity. Apart from that, the ionosphere is a dispersive medium for GNSS signals, which means that the magnitude of the delay depends on the signal frequency. Thus, the effects can be corrected almost completely by forming the ionosphere-free linear combination according to Equation (2.6) if dual-frequency observation data are available. Higher-order effects must be compensated by additional models (Brunner and Gu, 1991). In single-frequency applications such as the one at hand, an appropriate model must be applied. For example a single-layer model like the Klobuchar model (Seeber, 2003; Klobuchar, 1987), which was specially designed for the purposes of GPS. Its coefficients are broadcast with the navigation message and can therefore be applied in real-time by a user receiver. Since this model only accounts for a maximum of 50% of the overall effect, alternative models are required if enhanced PVT precision and accuracy are aimed for. Furthermore, using the Klobuchar model is not consistent with applying DCBs. Thus, IGS global ionosphere TEC maps (Schaer et al., 1998) must be used in a single-frequency case such as the one at hand. Since these maps are estimated together with DCBs (Hernández-Pajares et al., 1999), it is more consistent and accurate to use the maps as provided by CODE instead of ESOC, because their DCB corrections are also applied in the SPP algorithm.

The signal delays caused by the lower atmosphere ranging up to ca. 50 km above ground are comprised as *tropospheric refraction* in GNSS data analysis. In contrast to the ionospheric refraction, it cannot be eliminated or reduced by forming a linear combination of different signals. The size of this effect increases with the length of the signal path through the troposphere, i.e. it is higher in low elevation angles than in zenith direction at the user location, ranging from ca. 24 m to 2 m, respectively (Brunner and Welsch, 1992; Bevis et al., 1992). Thus, the tropospheric refraction is typically determined in zenith direction and then mapped to the respective elevation angle – where azimuthal symmetry is assumed. Furthermore, the total zenith path delay can be separated into two components. The spatially and temporally relatively stable hydrostatic/dry part which represents roughly about 90% of the total effect and is usually accounted for by an a priori model, for example according to Saastamoinen (1973), Niell (1996) or the more recent Vienna Mapping Function 1 (VMF1) and Global Mapping Function (GMF) as proposed by Böhm et al. (2006b) and Böhm et al. (2006a), respectively. On the other hand, the so-called wet part varies in a fairly unpredictable way in space and time due to the highly variable water vapor content in the neutral atmosphere. Thus, it cannot be assessed by a given model to the extent of millimeter accuracy required in high-precision GNSS applications using undifferenced observation data. In that case, additional troposphere parameters are typically estimated in data analysis. Since this does not apply to the SPP algorithm at hand, both hydrostatic and wet tropospheric delay are modeled by the Global Pressure and Temperature (GPT) atmosphere model (Böhm et al., 2007), the a priori model of Saastamoinen (1973) and the GMF, in accordance with the ESOC analysis strategy.

Tidal effects due to solid Earth (pole) and ocean (pole) tides as well as ocean and atmospheric *loading effects* are not considered. This is because they only amount to few centimeters maximum (Petit and Luzum, 2010), which is well below the measurement noise of the observations in use. Moreover, some of these effects, like e.g., atmospheric loading, are not yet adopted by the IGS analysis centers.

4.2 Performance Parameters

The performance of GNSS-based PNT is typically assessed by means of certain quality measures, that is primarily *precision* and *accuracy*. However, in safety-critical applications such as aviation, seafaring and rail traffic, other parameters are of much higher importance, especially in the context of the definition of a certain service. Above all, *integrity* has to be mentioned at this point, besides *reliability*, *availability* and *continuity*. Since these quality measures are used in this chapter in order to evaluate the impact of receiver clock modeling, they are briefly reviewed in this section based on Baarda (1968), Teunissen (1990), Salzmann (1991), Hofmann-Wellenhof et al. (2008), and Gleason and Gebre-Egziabher (2009). Note that coordinate and velocity parameters are estimated in a geocentric Cartesian reference frame as described in section 3.3, but receiver clock modeling almost exclusively affects the vertical components (Weinbach, 2013). Therefore, these parameters and the corresponding performance parameters presented in this section are converted to topocentric values for further evaluation.

4.2.1 Precision and Accuracy

Precision and accuracy of a given time series can be described by its respective empirical standard deviation (SD) and root mean square (RMS):

$$SD = \sqrt{\frac{1}{n-1} \sum_{i=1}^n (\bar{x} - x_i)^2}, \quad (4.1)$$

$$RMS = \sqrt{\frac{1}{n} \sum_{i=1}^n x_i^2}, \quad (4.2)$$

from a finite number of n observations of x_i with $i = \{1, 2, \dots, n\} \in \mathbb{N}$ and their corresponding mean \bar{x} . In contrast to the SD representing only the scattering, i.e. precision of the time series around its mean, the RMS is not reduced by the mean of the time series, thereby measuring its accuracy. Note that since the focus in the following will be on the comparison of coordinate and velocity time series *with* and *without* RCM, it is not necessary to compute any confidence intervals.

This approach, however, is only valid if the underlying time series is stationary, i.e. its mean and variance are constant over time and the autocovariance between two observations only depends on the temporal distance between them. These three types of stationarity are also referred to as *mean stationarity*, *variance stationarity* and *covariance stationarity*, respectively. Weak-sense stationarity can be assumed in case mean stationarity and covariance stationarity are present, where the latter also automatically includes variance stationarity (Niemeier, 2008). Here, covariance stationarity is more important since mean stationarity can easily be achieved by removing certain trends inside the data, for example through regression analysis.

It can be assumed that the coordinate and velocity estimates computed with RCM are not covariance stationary due to the temporal correlations introduced by the chosen clock models, that is a random ramp process in the LKF and an epoch-spanning polynomial in the SLSA. Therefore, the coordinate and velocity time series are reduced by the result of a moving average filter with a window length of five epochs. This removes the temporal correlations to an extent that stationarity can be assumed, which was successfully tested and verified during data analysis presented later in this chapter. On the one hand, this approach justifies the use of the standard deviation as a measure of precision. On the other hand, it also removes the mean value(s) from the time series, thus the RMS cannot be used as a measure of accuracy anymore.

However, there is a reason as to why the computation of such accuracy measures is neglected at all in this chapter. The RMS strongly depends on the mean and will therefore be very similar with and without RCM. Since this mean value is mainly determined by remaining systematic effects such as satellite orbit/clock errors and ionospheric delays, it can amount to relatively arbitrary values that are also not attributable to RCM. Furthermore, the mean is also not constant when RCM is applied. The RMS could be computed based on the results of the moving average filter, but since they are not representative for the impact of RCM, this computation is omitted for the remainder of this chapter.

4.2.2 Reliability

The concept of reliability was introduced by Baarda (1967) and Baarda (1968) for the purposes of statistically profound error detection in geodetic measurements. This basically requires redundant measurements in order to detect potential faulty ones in a statistically significant sense. Furthermore, these additional measurements must originate from different geometric configurations than the minimally necessary ones. Speaking in terms of GNSS-based positioning, four satellites must be observed simultaneously to compute a solution. If five satellites are available, statistical measures like variances of and covariances between the estimates can be calculated. This also enables *controllability* of the coordinates. However, in order to detect which of the measurements is erroneous, at least one more independent measurement is necessary, i.e. six satellites in view. Only this minimum of redundancy allows the *separability* of outliers and unbiased measurements (Niemeier, 2008). Such a position solution using at least six satellites can be referred to as *reliable*. This basic concept of outlier detection, identification and rejection can be implemented in various ways, for example by means of the so-called *data snooping* proposed by Baarda (1968). This method is also applied in the SPP routine described in section 4.1.

Internal reliability addresses the detectability of potential outliers in the measurement data. Since the corresponding measures can be computed prior to actual measurements, internal reliability is usually a design tool in order to determine the best possible measurement configuration. The most common measure is the minimal detectable bias (MDB) (Baarda, 1967):

$$\nabla l_i = \sigma_{l_i} \sqrt{\frac{\lambda_0}{r_i}}, \quad (4.3)$$

with the fixed non-centrality parameter λ_0 depending on the (user-defined) significance level η (probability of type-I error: false alarm) and detection power γ (one minus probability of type-II error: missed detection), the standard deviation σ_{l_i} of observation l_i as well as the redundancy number

$$r_i = \sigma_{\hat{v}_i \hat{v}_i}^2 p_i, \quad (4.4)$$

where $\sigma_{\hat{v}_i \hat{v}_i}$ is the standard deviation of the observation residual as described by Equation (2.27) and p_i denotes the corresponding element of the weight matrix, cf. Equation (2.23). Since Equation (4.4) is only valid for a least-squares adjustment, residuals v_i are substituted by innovations d_i and the redundancy numbers are derived from the redundancy matrix \mathbf{R} in a Kalman filter:

$$\mathbf{R} = \begin{bmatrix} \mathbf{KA} & -\mathbf{K} \\ -\mathbf{Q}_{ll} \mathbf{Q}_{dd}^{-1} \mathbf{A} & \mathbf{Q}_{ll} \mathbf{Q}_{dd}^{-1} \end{bmatrix}, \quad (4.5)$$

with Kalman gain matrix \mathbf{K} , design matrix \mathbf{A} and the cofactor matrices \mathbf{Q}_{ll} and \mathbf{Q}_{dd} of the observations and innovations, respectively. Minimal detectable biases determine the minimum size of an observation bias that can be detected by a one-dimensional hypothesis test (Salzmann, 1991). This means that a small(er) MDB enables the detection of a potential small(er) bias in the corresponding observation.

The result of transferring the MDBs from the observation domain to the parameter domain is referred to as *external reliability*. The distortion of the parameter vector \mathbf{x} due to an undetected bias can be described according to Equation (2.24) as

$$\nabla \mathbf{x}_i = (\mathbf{A}^T \mathbf{P} \mathbf{A})^{-1} \mathbf{A}^T \mathbf{P} \mathbf{h}_i \nabla l_i, \quad (4.6)$$

where \mathbf{h}_i is an $n \times 1$ -vector of zeros with a one entry corresponding to the respective single bias ∇l_i , e.g. in case of observation $i = 3$ with a total of $n = 7$:

$$\mathbf{h}_3 = \begin{bmatrix} 0 & 0 & 1 & 0 & 0 & 0 & 0 \end{bmatrix}^T. \quad (4.7)$$

This means that a single undetected bias impacts all parameters, whereas the user typically is only interested in the maximum distortions, for example to compare them to the VCM of the parameters.

4.2.3 Integrity

The integrity of a navigation system refers to its ability to inform the user with a timely alert and declare the system as unavailable in case of a large navigation error. Integrity is typically characterized by means of an *integrity risk* which is the probability with which such a large error occurs without being detected and issuing the alert (Gleason and Gebre-Egziabher, 2009). This can also be referred to as missed detection, thus illustrating the connection of integrity and reliability. Compared to typical accuracy significance levels of 0.1% to 5%, integrity risk values are very small and usually range from 10^{-7} to 10^{-9} . This is due to the much higher safety requirements, especially in aviation. From this integrity risk, so-called *protection levels (PLs)*, e.g. for horizontal and vertical coordinates, can be derived. In general, a PL represents a bound below which the probability of a *position error (PE)* is smaller than the integrity risk. An integrity alert is issued if the PL exceeds a predefined *alert limit (AL)*, which for example amounts to 40 m horizontally and 10–15 m vertically in category I precision landing approaches in aviation (ICAO, 2006). The relationships between PE, PL and AL with regard to system availability are depicted in the so-called Stanford diagram (Tossaint et al., 2006) shown in Figure 4.1.

Protection levels can be computed in various ways often dependent on the intended purpose. One method is based on the normally distributed parameter cofactor matrix $\mathbf{Q}_{\hat{\mathbf{x}}\hat{\mathbf{x}}}$, for example as defined by the International Civil Aviation Organization (ICAO):

$$\text{HPL} = \kappa_H \sigma_0 \sqrt{\frac{q_{nn} + q_{ee}}{2} + \sqrt{\left(\frac{q_{nn} - q_{ee}}{2}\right)^2 + q_{ne}^2}}, \quad (4.8)$$

$$\text{VPL} = \kappa_V \sigma_0 \sqrt{q_{uu}}, \quad (4.9)$$

with the elements q_{nn} , q_{ee} , q_{uu} and q_{ne} corresponding to the variances of the north, east, up coordinates and the covariance between the north and east coordinate, respectively. Note that $\mathbf{Q}_{\hat{\mathbf{x}}\hat{\mathbf{x}}}$ has to be converted into a topocentric local coordinate system beforehand. The a priori variance factor σ_0 as well as κ_H and κ_V act as scaling factors, where the latter are chosen depending on the application and probability distribution (integrity risk). According to ICAO (2006), in precision approaches (PAs) and approaches with vertical guidance, these values amount to $\kappa_{H,PA} = 6.0$ and $\kappa_{V,PA} = 5.33$, for example.

4.2.4 Continuity and Availability

By definition, *continuity* describes the ability and capability of a navigation system to perform or provide, respectively, a certain function without unscheduled interruptions throughout the intended

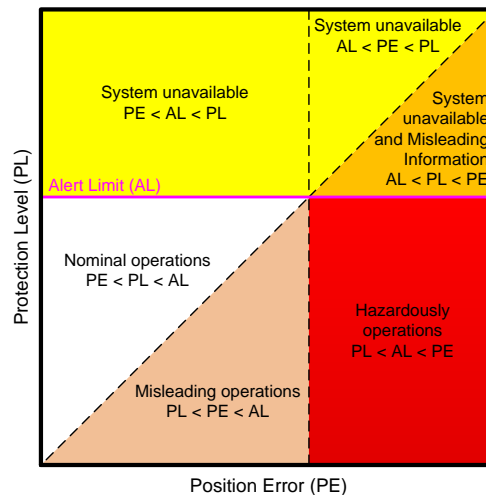


Figure 4.1: The Stanford integrity diagram

operation. Such an interruption can be caused by an *integrity alert*. In a numerical sense, continuity is associated with a particular probability with which the system maintains its performance during operation. This probability is typically defined by the complementary so-called *continuity risk*, which in aviation, for example, ranges from $1 \cdot 10^{-4}$ per hour en-route to $1 \cdot 10^{-6}$ per 15 s in precision landing approaches (ICAO, 2006). Therefore, continuity can be measured by the percentage of time during which the system performs without unscheduled interruptions. In case the requirements for accuracy, integrity and continuity of a specific service provided by a navigation system are ensured within its coverage area, it can be designated available. Thus, *availability* summarizes the most important GNSS performance parameters described in this section. It can be measured by the percentage of time during which the system is available for a specific operation. Availability can also correspond to the time GNSS signals are available to the users, which does not solely depend on the transmitting satellites but also on the user-specified environment, that is multipath, shadowing effects, etc.

4.3 Kinematic Single Point Positioning

4.3.1 Automotive Experiment

In order to validate the proposed approaches of RCM with respect to the results and conclusions of the clock comparisons in chapter 3, a kinematic experiment was carried out at the end of April 2014 on a cart-road in the vicinity of Hannover, Germany. The test track included only few natural obstructions in form of an alley in the southern area as depicted in Figure 4.2. The measurement configuration depicted in Figure 4.3 consisted of four *JAVAD Delta TRE-G3T* receivers and one *JAVAD Delta TRE-G3TH* receiver using the same firmware version (3.4.14). This is very important since different firmware versions could possibly bias the comparisons between the receivers. In addition, a *NovAtel SPAN-SE-D* receiver combined with an *iMAR FSAS* IMU was employed for the purposes of generating a reference solution for each test drive. All receivers were connected to one *NovAtel 703 GGG* antenna on the roof of the motor vehicle (cf. Figure 4.4b) via an active signal splitter, hence recording virtually the same observations. The arrangement of the receivers and clocks in a box inside the vehicle is depicted in Figure 4.4a. This box was lightly cushioned to protect the oscillators from abrupt shocks caused by e.g. pot holes. Four of the five JAVAD receivers were each fed by the 10 MHz signals of one of the external oscillators described and tested in section 3.2. One JAVAD receiver as well as the NovAtel receiver were driven by their respective internal oscillator. Both GPS and GLONASS observations were recorded with a data rate of 1 Hz during several test drives that lasted for roughly eight minutes each.



Figure 4.2: Test track of kinematic car experiment: the yellow ellipse depicts a natural alley with signal obstructions, the blue dot indicates the location of the local reference station, the red arrow indicates starting point and driving direction of each eight-shaped test drive (source of map: Google Maps)

In addition, a local reference station consisting of a *Leica GRX1200+* GNSS receiver and a *Leica AX1202GG* antenna was installed temporarily close to the geographical center of the test track, cf. Figure 4.2. This enables the computation of a reference trajectory for every test drive by using multi-GNSS phase and Doppler observations combined with the IMU data in tightly coupled relative positioning. The coordinates of the local reference station are computed by means of PPP using the *Bernese GNSS Software 5.2* (Dach et al., 2015) based on a two-hour data set of GPS and GLONASS observations with a sampling interval of 15 s. The resulting coordinates exhibit an accuracy of a few centimeters. These values are then introduced as fixed coordinates into the post-processing software *TerraPOS 2.4.0* (Kjørsvik and Brøste, 2009) with which the reference trajectories are finally computed. The SPP analysis with and without RCM based on GPS and GLONASS L1 C/A-code and Doppler observations are conducted as described in sections 3.3 and 4.1. For reasons of consistency, the reference trajectories are computed using the same ESOC satellite orbit and clock products.

The findings presented in the subsequent sections are subdivided into the SPP results of the linearized Kalman filter (section 4.3.2) and those of the sequential least-squares adjustment (section 4.3.3). The latter are discussed in more detail since they are based on the primary method of clock modeling in this thesis as described in section 3.3.2. All results in these sections are computed by means of the software module presented in section 4.1 assuming observation uncertainties of 1 m and 3 cm/s for L1 C/A-code and Doppler observations, respectively, applied with an elevation-dependent weighting:

$$p_i = \sin^2(E), \quad (4.10)$$

with weight p of satellite i at elevation angle E . The results are discussed exemplarily based on one of six test drives. The main reason for multiple test drives was redundancy of measurement data. The analysis of all test drives led to very similar and reproducible results. Therefore, the one test drive presented in the following can be considered representative for all drives of *this* particular experiment.

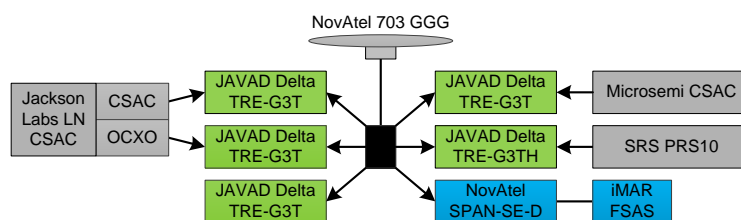
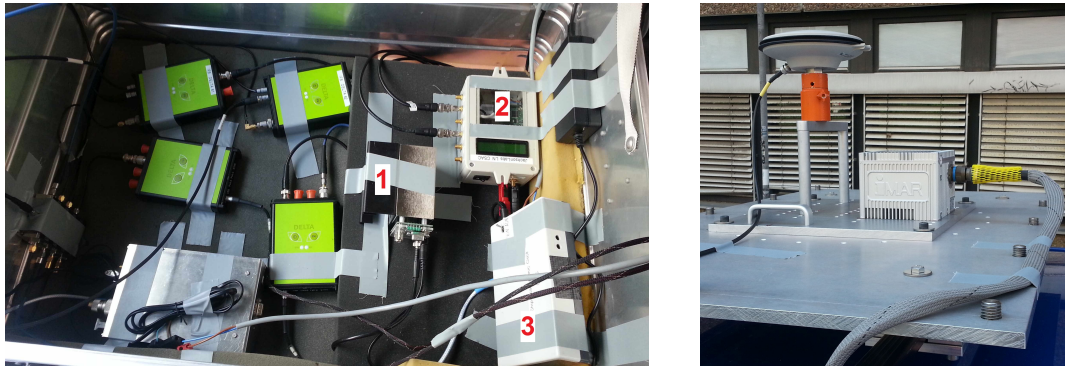


Figure 4.3: Measurement configuration of kinematic car experiment



(a) JAVAD GNSS receivers (left-hand) and miniature atomic clocks (right-hand) in a cushioned box inside the car: (1) SRS PRS10, (2) Jackson Labs LN CSAC, (3) Microsemi CSAC

(b) GNSS antenna and IMU on a platform on the roof of the car

Figure 4.4: Parts of the measurement equipment of the kinematic car experiment

4.3.2 Kalman Filter Results

Position and Velocity Precision

At first, the multi-GNSS PVT solution – relative to the reference solution – of the JAVAD receiver driven by its internal quartz oscillator is shown in Figure 4.5, where epochwise independent clock bias estimation is applied. The mean coordinate and velocity deviations of a few decimeters and centimeters per second, respectively, can be considered typical for such an SPP solution in the light of the fact that geodetic receivers were used in the experiment. The coordinate offsets of up to ± 2 m can be attributed to remaining ionospheric effects since only L1 observations are used, as well as station-

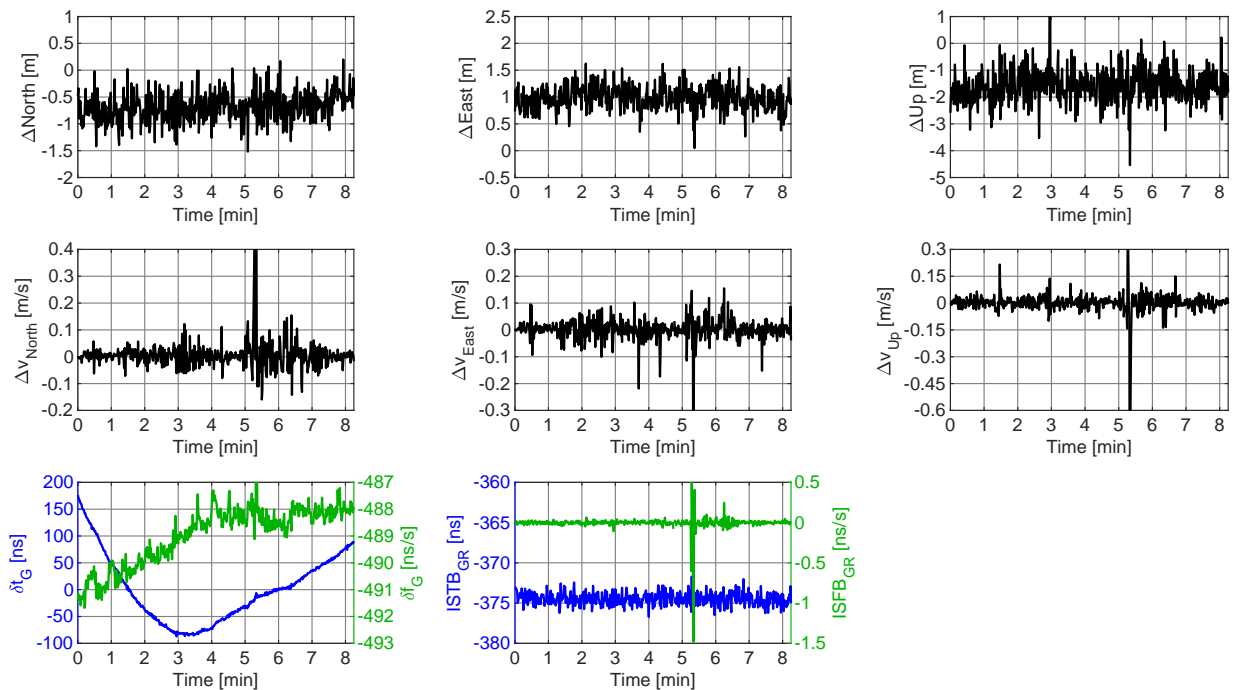


Figure 4.5: Times series of topocentric coordinate (upper row) and velocity (middle row) deviations relative to reference solution, as well as clock time offset after a straight line fit, clock frequency offset, inter-system time and frequency biases (bottom row) of receiver driven by its internal quartz oscillator; analyzed by means of a Kalman filter. Note the different y-axes scalings of the vertical components.

dependent errors such as multipath. The velocity deviations scatter around zero mean. An increase of the deviations, especially in case of the velocity estimates, can be seen from approximately minute five to minute seven, when the vehicle was driving through the alley (cf. Figure 4.2). Concerning the coordinate estimates, hardly any increased deviation is visible.

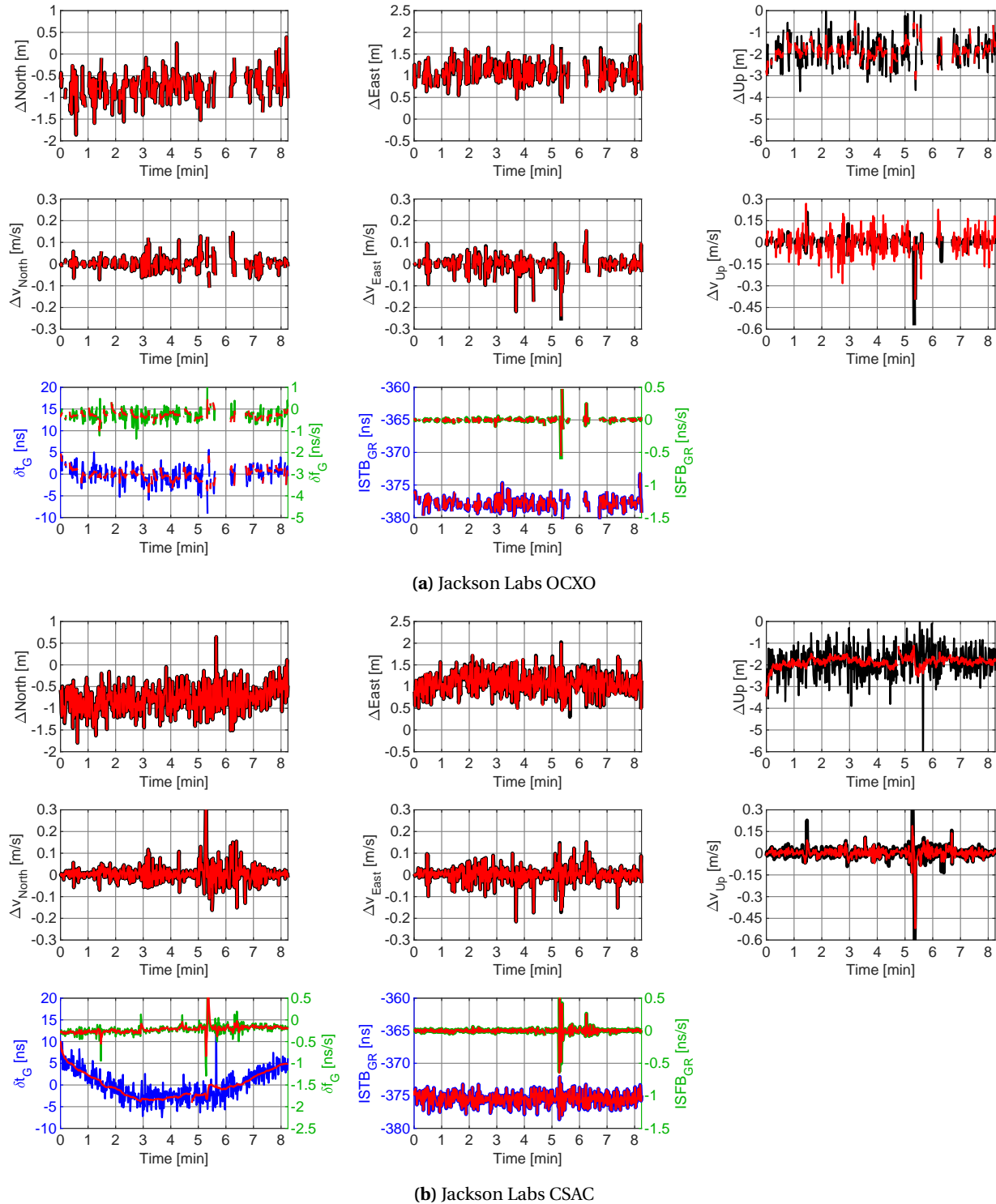
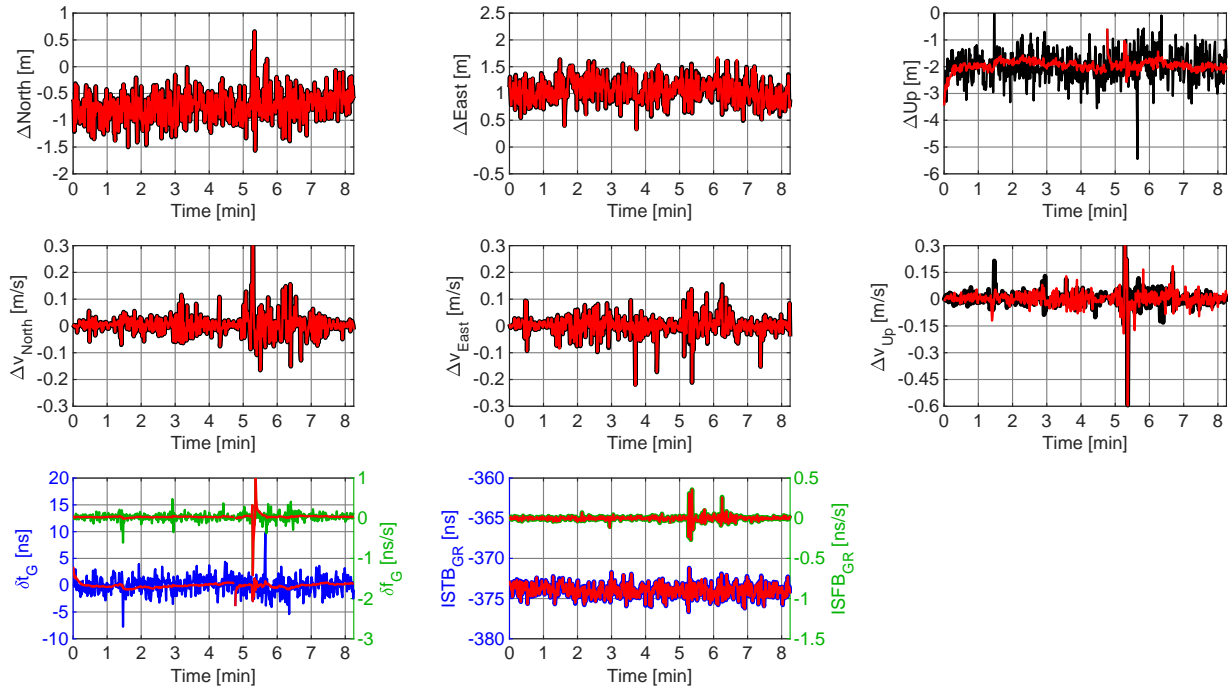
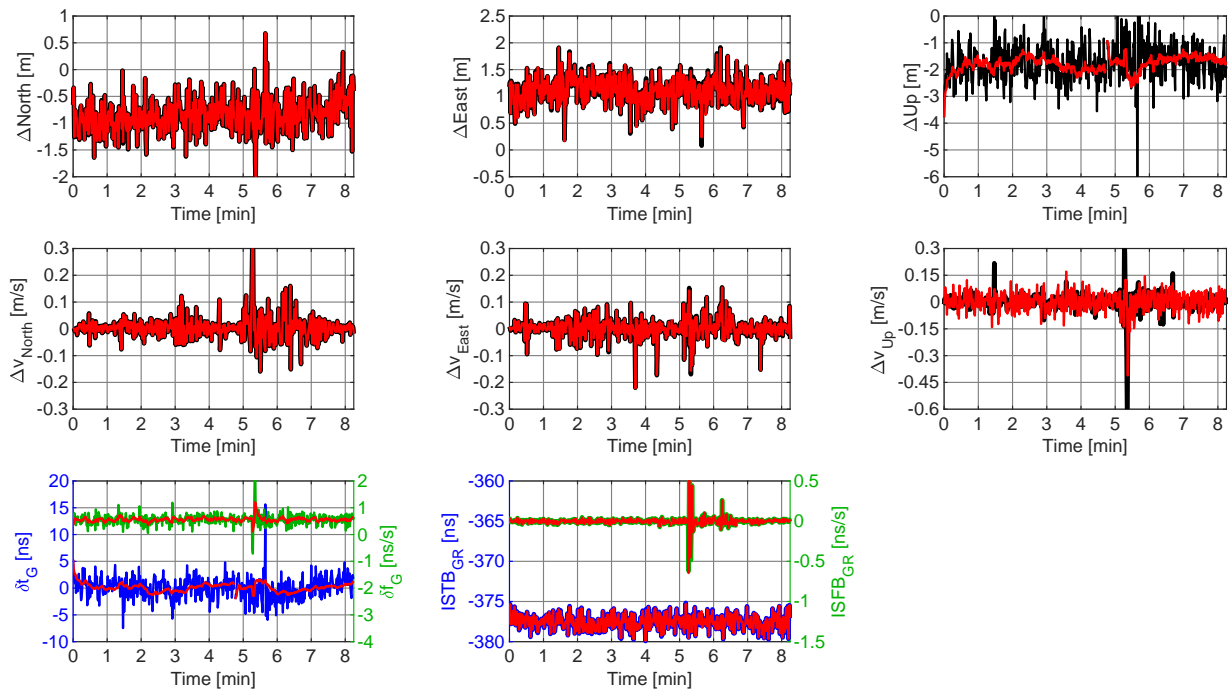


Figure 4.6: Times series of topocentric coordinate (upper row) and velocity (middle row) deviations relative to reference solution, as well as clock time offset after a straight line fit, clock frequency offset, inter-system time and frequency biases (bottom row), depicted without and with receiver clock modeling in black and red, respectively; analyzed by means of a Kalman filter using the clock model of Dierendonck et al. (1984). Note the different y-axes scalings of the vertical components.

Furthermore, the type of oscillator that is driving the receiver can be derived from the clock bias time series, because of the significant frequency drift – superimposed by further higher-order systematic effects – and the relatively large range of estimated values spanning ca. 300 ns in just eight minutes (cf. Figure 4.5). As expected, the inter-system biases do not show any drift behavior over such a short



(a) Stanford Research Systems PRS10



(b) Microsemi CSAC

Figure 4.7: Times series of topocentric coordinate (upper row) and velocity (middle row) deviations relative to reference solution, as well as clock time offset after a straight line fit, clock frequency offset, inter-system time and frequency biases (bottom row), depicted without and with receiver clock modeling in black and red, respectively; analyzed by means of a Kalman filter using the clock model of Dierendonck et al. (1984). Note the different y-axes scalings of the vertical components.

period of time as the eight-minute test drive. In addition, slight correlations between the inter-system frequency biases and the up-velocities exist. However, since they are very small, it has no effect on the up-velocity estimates in case only inter-system time biases and no frequency biases were estimated.

The same analysis is carried out with the observation data of the four JAVAD receivers each connected to a different external clock. The resulting time series are depicted in Figures 4.6 and 4.7. In contrast to the receiver driven by its internal oscillator, this time, also receiver clock modeling is applied by means of the model of Dierendonck et al. (1984) with the values given in Table 3.5. The solutions without RCM show similar behavior to that shown in Figure 4.5, except for the clock biases which are progressing much smoother and exhibit only small frequency offsets in the range of tenths of nanoseconds per second. Just the Jackson Labs CSAC depicted in Figure 4.6b shows a distinct frequency drift.

Furthermore, the high correlations between up-coordinates and clock time bias are reflected exemplarily by the peak after 339 seconds (5.65 minutes). The same applies to the up-velocities and the clock frequency bias as can be seen around epoch 318 (5.3 minutes) in case of the Microsemi CSAC, cf. Figure 4.7b. From another perspective, it can be concluded that the filtering approach does not mitigate short-term peaks in both the clock time and frequency biases. These peaks are more likely induced by the degraded GNSS observations when driving through the alley of the test track, and are not due to sudden changes in the behavior of the respective oscillator.

When clock modeling is applied, the vertical coordinate and velocity estimates are affected exclusively. The precision of the up-coordinates is improved significantly by approximately 80% for all four receivers, whereas the vertical velocities become mostly noisier. Only in case of the receivers connected to the Jackson Labs CSAC and the SRS PRS10, improvements of the up-velocity precision of ca. 28% and 8%, respectively, are obtained. In addition to the high degradation of the precision of the up-velocities, the receiver fed by the signal of the Jackson Labs OCXO also exhibits very frequent data gaps. The latter is probably caused by the high sensitivity of the oscillator to external influences such as vibrations – although it was placed on a cushioned surface during the experiment –, thereby degrading the oscillator performance, i.e. its frequency stability. Furthermore, it is also possible that the L1 Doppler observation noise is smaller than assumed. Thus, velocity determination does not benefit from clock modeling, in fact, it has a negative effect on it in general. However, it still mitigates sudden vertical velocity deviations as can be seen in Figure 4.6a. A summary of the impact of receiver clock modeling on the precision of the vertical coordinate and velocity estimates is given in Table 4.1.

Receiver clock modeling has hardly any effect on neither the code nor Doppler residuals as shown exemplarily for the Jackson Labs CSAC in Figures 4.8a to 4.8h. Only small increases of a few peaks are visible when applying RCM. These increased peaks correspond to the decreased peaks in the vertical coordinate and velocity time series, cf. Figure 4.6b. In other words, the coordinate and velocity peaks

Table 4.1: Impact of receiver clock modeling (RCM) on the precision of vertical coordinate and velocity estimates in terms of their repeatability (1σ standard deviation, SD) relative to the reference solution, computed by means of a Kalman filter using the clock model of Dierendonck et al. (1984). Positive or negative ratios mean an improvement or a degradation, respectively, due to RCM.

Oscillator	Up-coordinate SD			Up-velocity SD		
	w/o RCM [m]	w/RCM [m]	Ratio [%]	w/o RCM [m/s]	w/RCM [m/s]	Ratio [%]
Jackson Labs OCXO	0.524	0.128	76	0.026	0.079	-201
Jackson Labs CSAC	0.610	0.091	85	0.040	0.029	28
SRS PRS10	0.527	0.104	80	0.049	0.046	8
Microsemi CSAC	0.611	0.090	85	0.041	0.048	-16

are absorbed by the residuals. Furthermore, the Doppler residuals are more pronounced than the code residuals, when the car was driving through the alley (cf. Figure 4.2).

The improvements of the overall precision of the kinematic coordinate estimates also shows in the DOP values depicted in Figure 4.9a using the example of the Jackson Labs CSAC. Again, only the vertical component is affected DOP with an improvement of 72% after a short warm-up period of approximately 30 seconds.

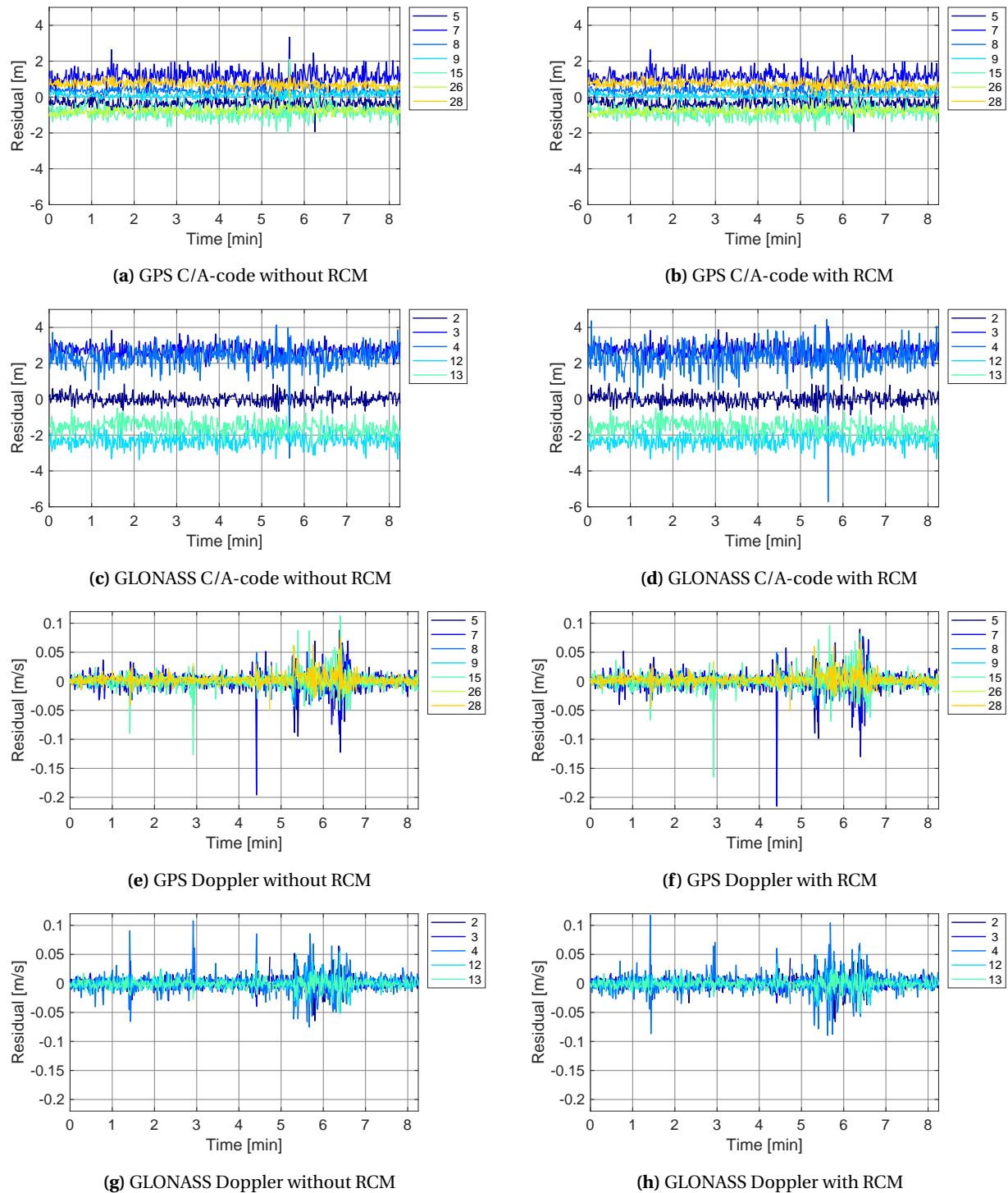


Figure 4.8: Color-coded/satellite-dependent GPS and GLONASS L1 C/A-code and Doppler residuals with and without receiver clock modeling (RCM) of receiver connected to the Jackson Labs CSAC, analyzed by means of a Kalman filter using the clock model of Dierendonck et al. (1984)

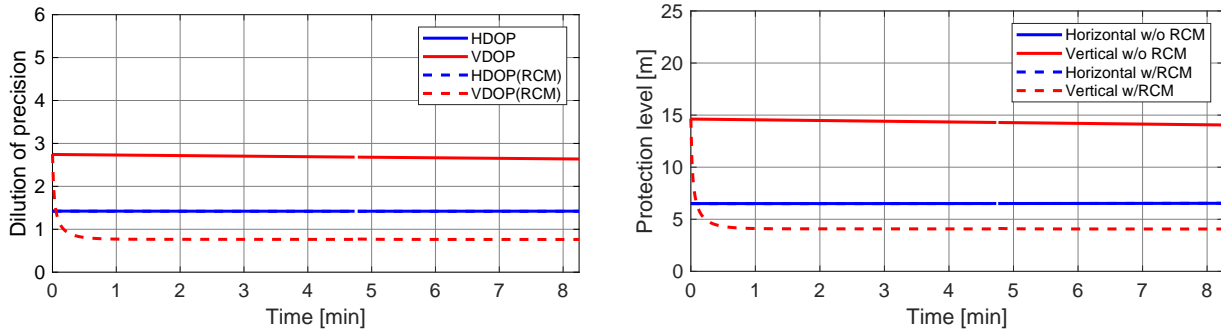


Figure 4.9: Dilution of precision (DOP) values and protections levels with (dashed lines) and without (solid lines) receiver clock modeling (RCM) of receiver connected to the Jackson Labs CSAC, analyzed by means of a Kalman filter using the clock model of Dierendonck et al. (1984). Note that the horizontal values with and without RCM coincide in both depictions.

Integrity and Reliability

The horizontal and vertical protection levels of the receiver connected to the Jackson Labs CSAC are shown in Figure 4.9b. In accordance with the impact of RCM on the DOP values, which reflect the quality of the observation geometry, only the vertical protection levels are improved by approximately 72% on average. The horizontal values remain unchanged when applying clock modeling. The similarities in the effects on the DOP values and protection levels are due to the fact that both kinds of measures are derived from the same source, that is the cofactor matrix of the estimated parameters.

The internal reliability of the PVT solution shown in Figure 4.6b is depicted in terms of minimal detectable biases in Figures 4.10a to 4.10h. Here, the impact of clock modeling is less pronounced than in case of the coordinate and velocity estimates. Whereas some satellites are not affected at all, the maximum improvements on code and Doppler observations amount to approximately 17% and 12%, respectively, for GPS satellite G15 and ca. 15% and 10%, respectively, for GLONASS satellite R04 (cf. Table 4.2). A subtle dependence on the elevation angle can be observed since satellites near the

Table 4.2: Average minimal detectable biases (MDBs) of GPS (G) and GLONASS (R) L1 C/A-code and Doppler observations with and without receiver clock modeling (RCM) of receiver connected to the Jackson Labs CSAC, computed by means of a Kalman filter using the clock model of Dierendonck et al. (1984). Positive or negative ratios mean an improvement or a degradation, respectively, due to RCM.

Satellite	Elevation angle [°]	C/A-code MDB			Doppler MDB		
		w/o RCM [m]	w/RCM [m]	Ratio [%]	w/o RCM [m/s]	w/RCM [m/s]	Ratio [%]
G05	51.4	5.751	5.598	3	0.173	0.170	2
G07	28.7	8.904	7.790	13	0.268	0.245	8
G08	58.3	4.842	4.842	0	0.145	0.145	0
G09	69.4	4.586	4.449	3	0.138	0.135	2
G15	28.1	9.900	8.179	17	0.298	0.262	12
G26	65.9	5.009	4.971	1	0.150	0.150	0
G28	49.9	5.696	5.583	2	0.171	0.169	1
R02	40.4	7.734	7.077	8	0.232	0.219	5
R03	73.8	4.742	4.442	6	0.142	0.137	4
R04	23.1	11.549	9.814	15	0.346	0.312	10
R12	56.5	5.713	5.712	0	0.171	0.171	0
R13	63.4	4.838	4.793	1	0.145	0.144	1

horizon exhibit the largest improvements. This effect is amplified by the applied elevation-dependent weighting of the observations, but also occurs when identity weighting is used. Thus, observations with low elevation angles benefit the most from receiver clock modeling in the case at hand. Overall, smaller MDB values lead to an enhanced detectability of possible outliers and blunder in the observation data, and thereby increase the overall robustness of the parameter estimation.

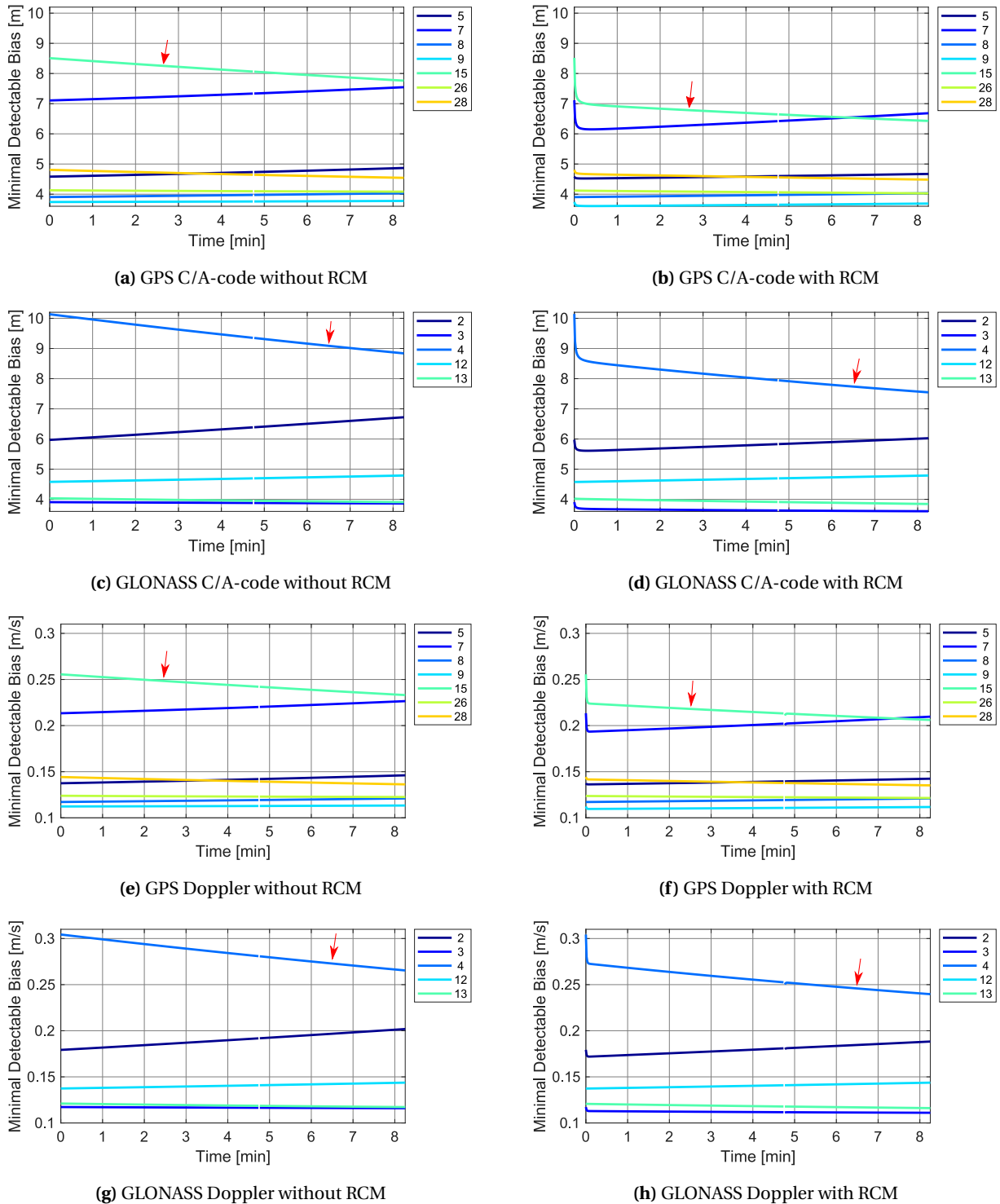


Figure 4.10: Color-coded/satellite-dependent GPS and GLONASS L1 C/A-code and Doppler internal reliability with and without receiver clock modeling (RCM) of receiver connected to the Jackson Labs CSAC, analyzed by means of a Kalman filter using the clock model of Dierendonck et al. (1984); satellites exhibiting maximum improvements are indicated by red arrows

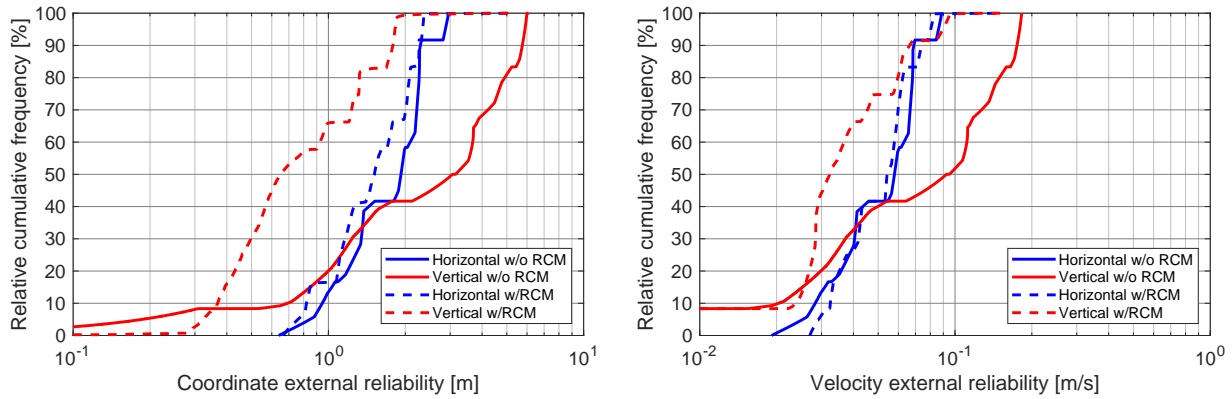


Figure 4.11: External reliability of coordinate and velocity estimates with (dashed lines) and without (solid lines) receiver clock modeling (RCM) of receiver connected to the Jackson Labs CSAC, analyzed by means of a Kalman filter using the clock model of Dierendonck et al. (1984)

It is well known that every single MDB has an effect on *all* parameters. When transferred from the observation domain to the parameter domain, the maximum parameter distortion due to such an MDB can be computed. Since this leads to a huge number of values for external reliability, they are depicted by means of relative cumulative frequency diagrams for the coordinate and velocity estimates. Figure 4.11 shows these values for the receiver connected to the Jackson Labs CSAC separated into horizontal and vertical components. It can be seen that receiver clock modeling has hardly any effect on the horizontal values, which applies to both coordinate and velocity estimates. On the contrary, the values for the vertical components are distinctly decreased when applying RCM. In case of the up-coordinates, the percentage of values smaller than one meter is increased from approximately 20% to 67%. Furthermore, with and without clock modeling 95% of the vertical values are smaller than ca. 1.8 m and 5.9 m, respectively. That is an improvement of about 70%. With regards to the velocity estimates, when clock modeling is applied, 95% of the vertical values do not exceed 0.090 m/s compared to 0.179 m/s without RCM. Conclusively, receiver clock modeling makes the overall PVT filter solution more reliable, i.e. more resilient against large coordinate and velocity deviations.

4.3.3 Sequential Least-squares Results

Position and Velocity Precision

When applying the least-squares approach, the PVT solution of the receiver driven by its internal oscillator is the same as in case of the Kalman filter as presented in section 4.3.2, where very relaxed values were chosen for the process noise models of all parameters, cf. section 3.3.1. Thus, it is neither depicted nor discussed at this point. The sequential solutions of the four receivers each connected to one of the atomic clocks are shown in Figures 4.12 and 4.13, again with receiver clock modeling as well as independent epochwise clock estimation. Due to the relatively short duration of each test drive of approximately 500 s, only one clock segment has to be applied according to Table 3.4. In addition, the proposed concept of clock modeling can be applied to the inter-system biases, referred to as ISBM. However, when doing so, the improvements in the precision of the vertical coordinates and velocities due to RCM are slightly degraded compared to the results without ISBM. Because of this counter-effect, ISBM is not applied in the following.

For all receivers connected to an external clock, results similar to those of Kalman filter analysis are achieved when applying RCM as shown by Figures 4.12 and 4.13. Again, clock modeling does only

affect the vertical components of the coordinate and velocity estimates. It is notable that the improvements in the vertical coordinates are more pronounced, i.e. the smoothing effect of clock modeling is stronger than in section 4.3.2. In case of the Jackson Labs OCXO, the up-coordinates precision is improved by 83%, compared to the Kalman filter improvement of 76%. On the contrary, the precision

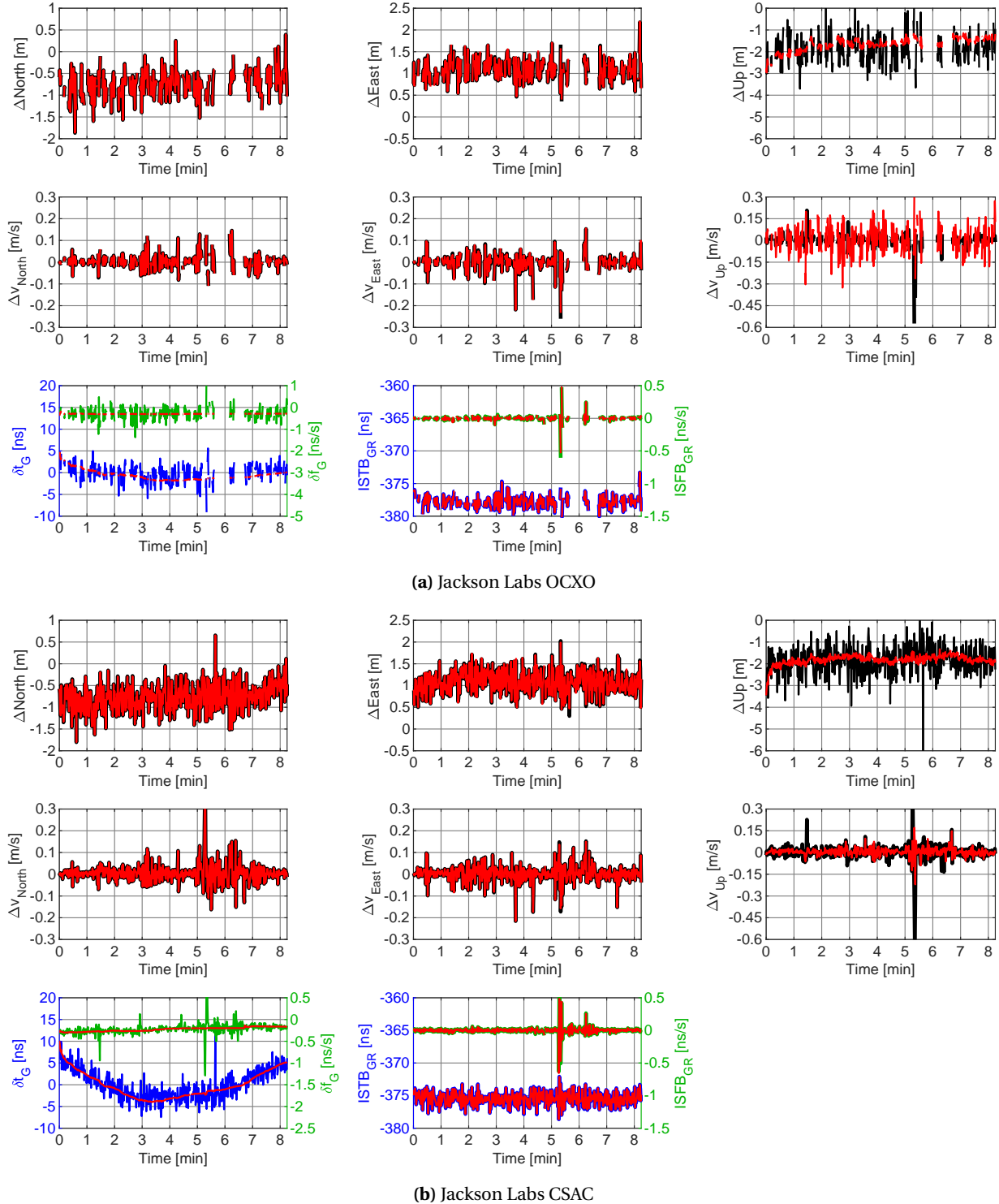
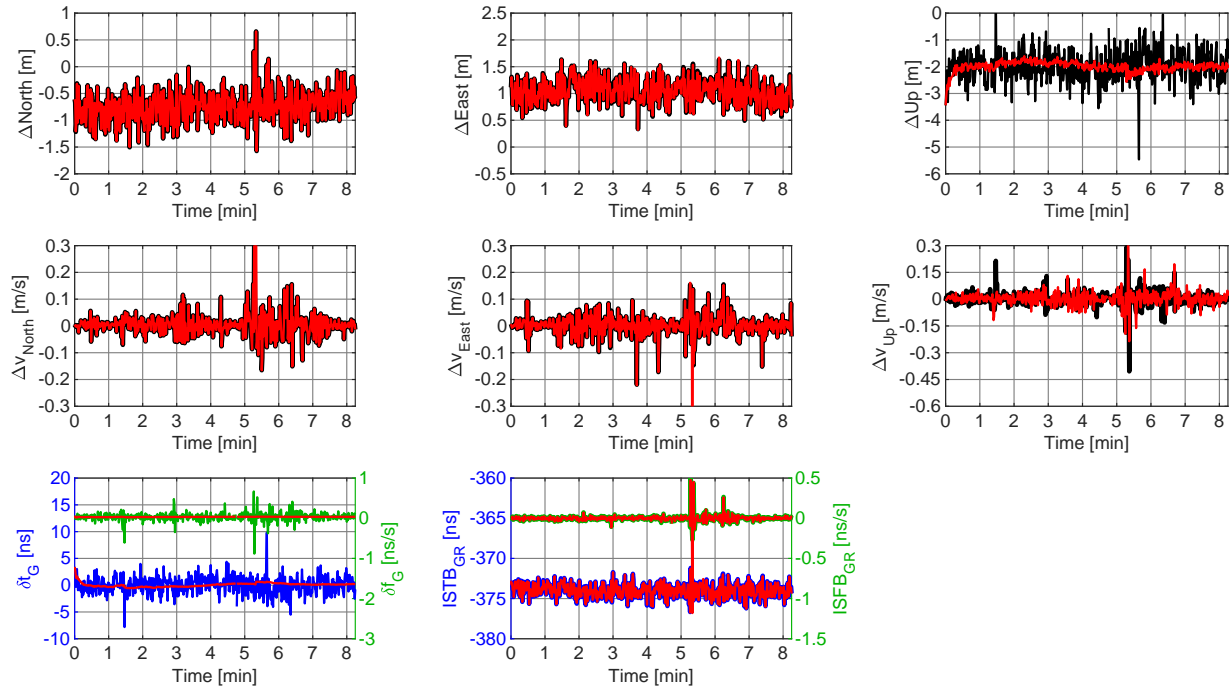
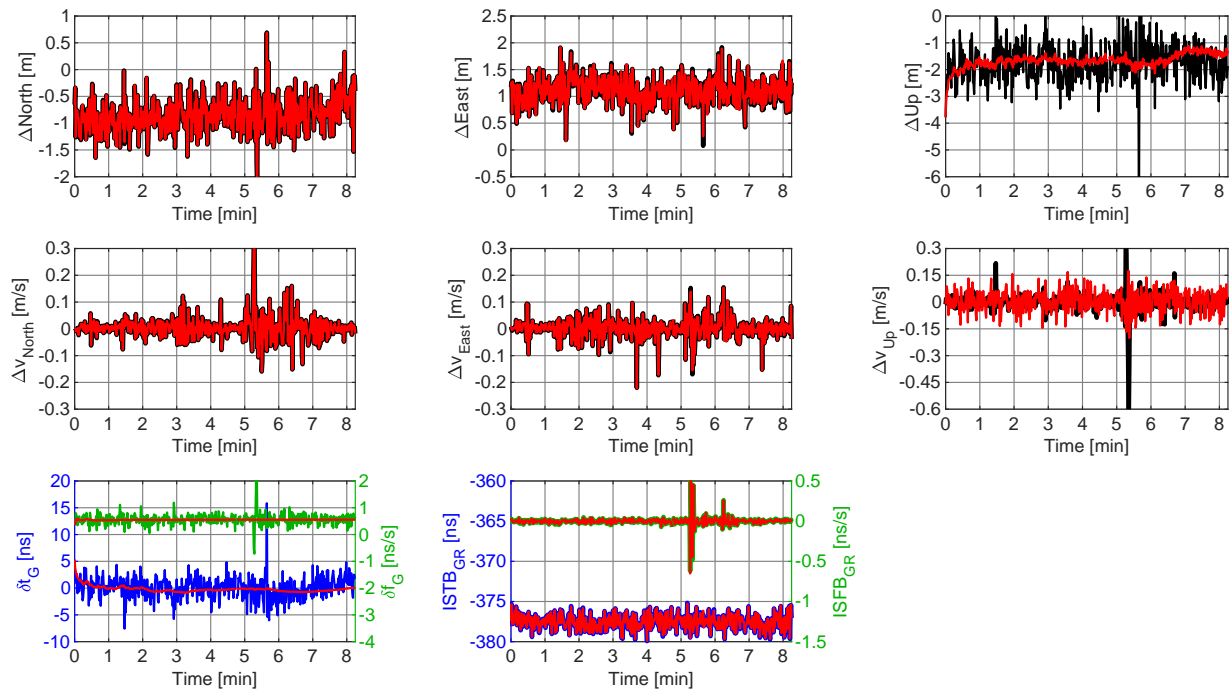


Figure 4.12: Times series of topocentric coordinate (upper row) and velocity (middle row) deviations relative to reference solution, as well as clock time offset after a straight line fit, clock frequency offset, inter-system time and frequency biases (bottom row), depicted without and with receiver clock modeling in black and red, respectively; analyzed by means of a sequential least-squares adjustment using a piecewise linear clock polynomial. Note the different y-axes scalings of the vertical components.

of the vertical velocities is further degraded. This confirms the assumption made in section 4.3.2 that the oscillator frequency stability determined in a laboratory environment (cf. section 3.2.2) is probably distinctly degraded when the oscillator is used under stress in an automotive experiment.



(a) Stanford Research Systems PRS10



(b) Microsemi CSAC

Figure 4.13: Times series of topocentric coordinate (upper row) and velocity (middle row) deviations relative to reference solution, as well as clock time offset after a straight line fit, clock frequency offset, inter-system time and frequency biases (bottom row), depicted without and with receiver clock modeling in black and red, respectively; analyzed by means of a sequential least-squares adjustment using a piecewise linear clock polynomial. Note the different y-axes scalings of the vertical components.

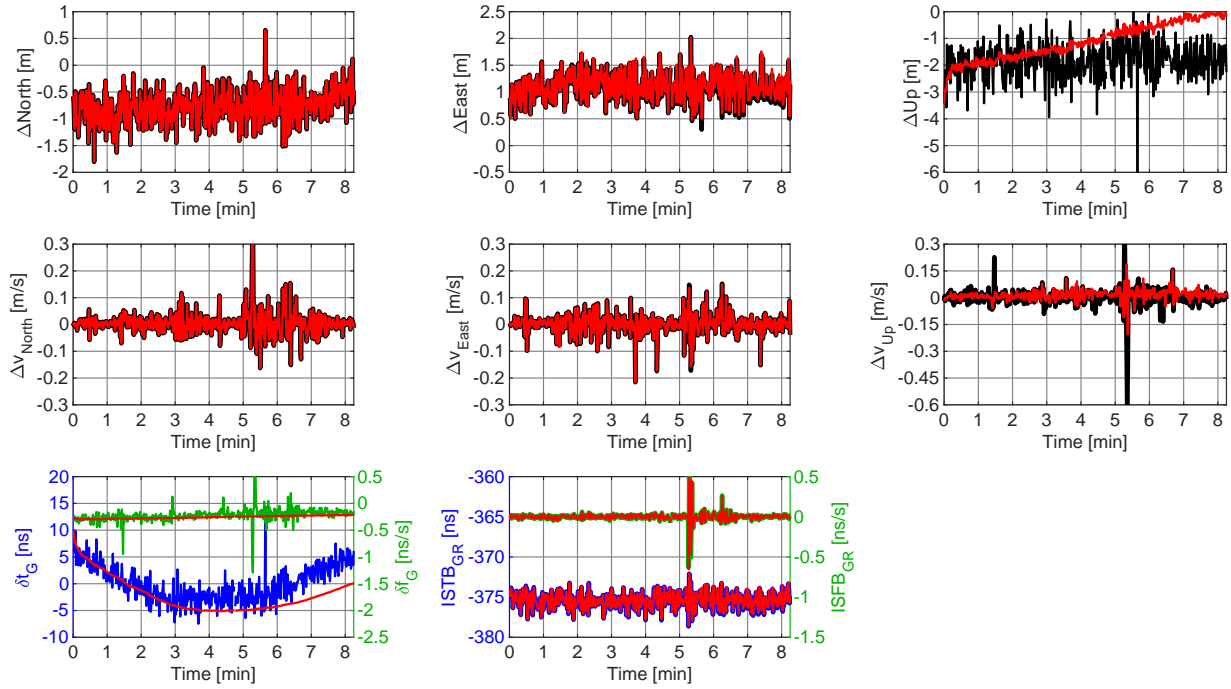


Figure 4.14: Times series of topocentric coordinate (upper row) and velocity (middle row) deviations relative to reference solution, as well as clock time offset after a straight line fit, clock frequency offset, inter-system time and frequency biases (bottom row), depicted without and with receiver clock modeling in black and red, respectively; analyzed by means of a sequential least-squares adjustment using a piecewise linear clock polynomial without considering the clock frequency drift. Note the different y-axes scalings of the vertical components.

The significant frequency drift of the Jackson Labs CSAC offers a good opportunity to validate the approach of hypothesis testing for a new clock modeling segment as proposed in section 3.3.2 using a significance level of 1%. The results shown in Figure 4.12b contain the starts of new modeling segments at epochs 54, 98, 204 and 404. Relative constraining of the slopes of consecutive segments helps to mitigate jumps of the clock bias estimates at the interval boundaries. Note that if such a frequency drift is not accounted for, mismodeling of the receiver clock caused thereof directly translates into the vertical coordinate estimates as shown in Figure 4.14.

An obvious advantage of the sequential clock modeling approach compared to the Kalman filter model is the fact that the peaks in the frequency offset estimates after approximately 5.3 minutes disappear. These deviations are most likely not caused by the oscillator but are a residual effect induced by the correlations with the up-velocity estimate at that time. By appropriately modeling the clock behavior

Table 4.3: Impact of receiver clock modeling (RCM) on the precision of vertical coordinate and velocity estimates in terms of their repeatability (1σ standard deviation, SD) relative to the reference solution, computed by means of a sequential least-squares adjustment using a piecewise linear clock polynomial. Positive or negative ratios mean an improvement or a degradation, respectively, due to RCM.

Oscillator	Up-coordinate SD			Up-velocity SD		
	w/o RCM [m]	w/RCM [m]	Ratio [%]	w/o RCM [m/s]	w/RCM [m/s]	Ratio [%]
Jackson Labs OCXO	0.532	0.091	83	0.026	0.086	-228
Jackson Labs CSAC	0.618	0.088	86	0.040	0.026	35
SRS PRS10	0.533	0.086	84	0.042	0.039	8
Microsemi CSAC	0.619	0.084	86	0.041	0.052	-27

these artifacts are also reduced in the vertical velocity time series. This effect is visible in case of all receivers as depicted in Figures 4.12 and 4.13. A summary of the improvements of sequential clock modeling is given by Table 4.3.

The residuals with and without clock modeling are shown in Figures 4.15a to 4.15h for all GPS and GLONASS satellites visible during the test drive of the experiment. The impact of RCM is very subtle

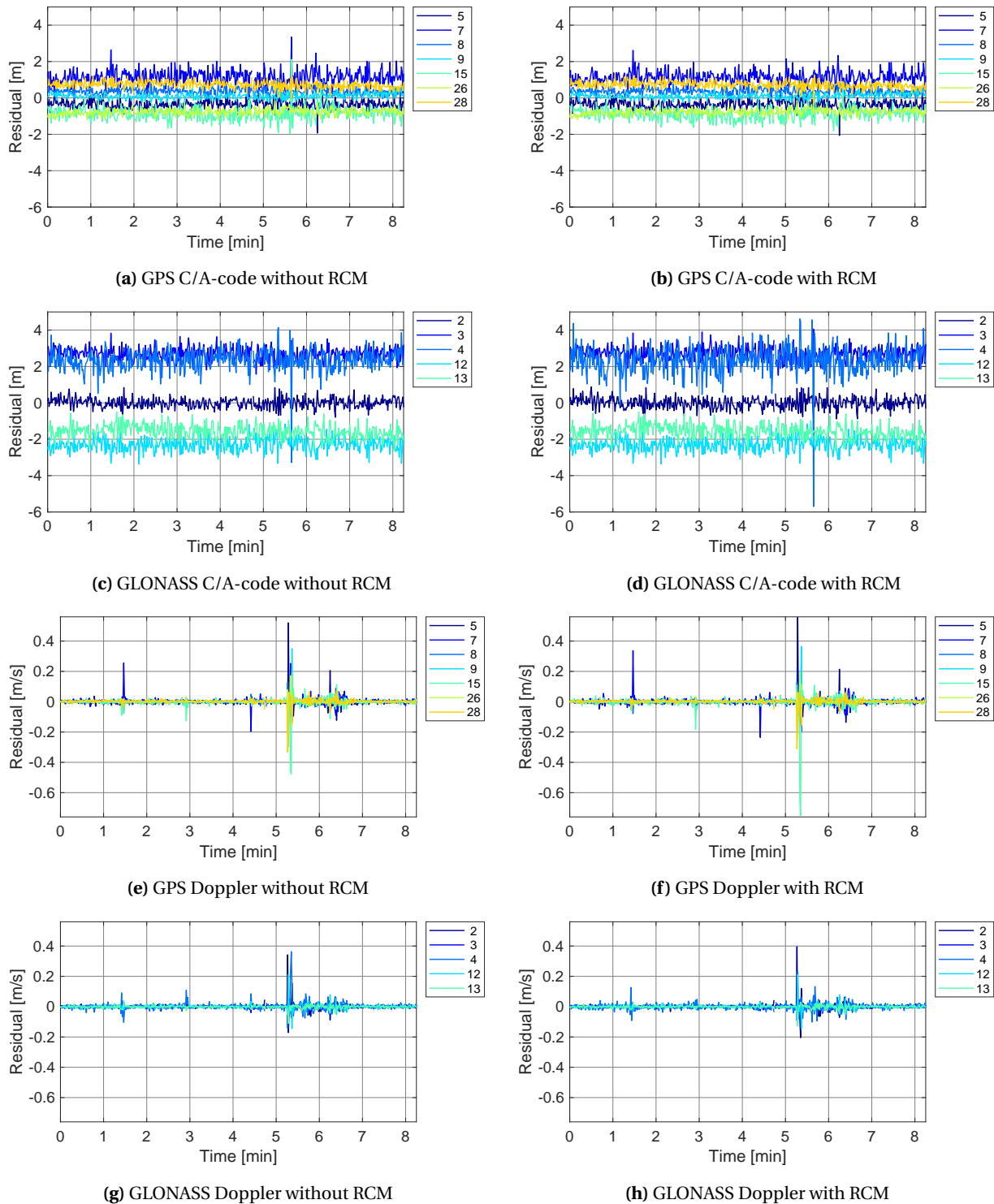


Figure 4.15: Color-coded/satellite-dependent GPS and GLONASS L1 C/A-code and Doppler residuals with and without receiver clock modeling (RCM) of receiver connected to the Jackson Labs CSAC, analyzed by means of a sequential least-squares adjustment using a piecewise linear clock polynomial

and does not differ from the Kalman filter results discussed in section 4.3.2. This also applies to the DOP values depicted in Figure 4.16a.

Another point of discussion or improvement, respectively, is the convergence time at the beginning of sequential clock modeling. The results of RCM shown in Figures 4.12 and 4.13 are computed based on a priori values of the clock coefficients that are set to zero. Now, it can be argued that known values should be used as constraints to improve their convergence time. However, it has to be kept in mind that the coefficient estimates already converge relatively fast within approximately ten epochs. Furthermore, in case out-of-date values – or values that simply do not reflect the current clock behavior – are potentially constrained too tightly, the convergence time will actually be prolonged or even have a divergent effect on the overall PVT solution. Therefore, this approach should only be considered if good a priori values are available.

Integrity and Reliability

The vertical protection levels of the receiver connected to the Jackson Labs CSAC shown in Figure 4.16b are the same as computed by the Kalman filter with and without RCM. Furthermore, each start of a new modeling segment leads to a short increase of the vertical PLs as already discussed with regard to the DOP values which are both computed based on the cofactor matrix of the estimated parameters. The horizontal values are not affected at all by clock modeling.

Internal reliability is computed once more in terms of MDBs and shown in Figures 4.17a to 4.17h. Whereas some satellites are not affected at all, receiver clock modeling has the largest impact on satellites with low elevation angles. More precisely, the L1 C/A-code and Doppler observations of GPS satellite G15 are improved by ca. 18%, those of the GLONASS satellite R04 by approximately 15% and 16%, respectively. The MDBs of all satellites in view with and without RCM are given by Table 4.4. Although the improvements due to clock modeling expressed in percentage terms are almost the same as in case of the Kalman filter, the overall values are slightly increased in the SLSA. The main reason for this are the smaller redundancy numbers of the filter solution. Furthermore, the Doppler observations are particularly sensitive to this approach of clock modeling since the starts of new modeling segments can be seen in the corresponding MDBs, which is especially pronounced in case of the last one after 6.7 minutes.

The impact of sequential RCM on external reliability of the coordinate estimates is virtually the same as discussed for the Kalman filter approach, cf. Figures 4.11a and 4.18a. With regards to the velocity parameters, the impact of clock modeling is distinctly higher than in case of the Kalman filter. When

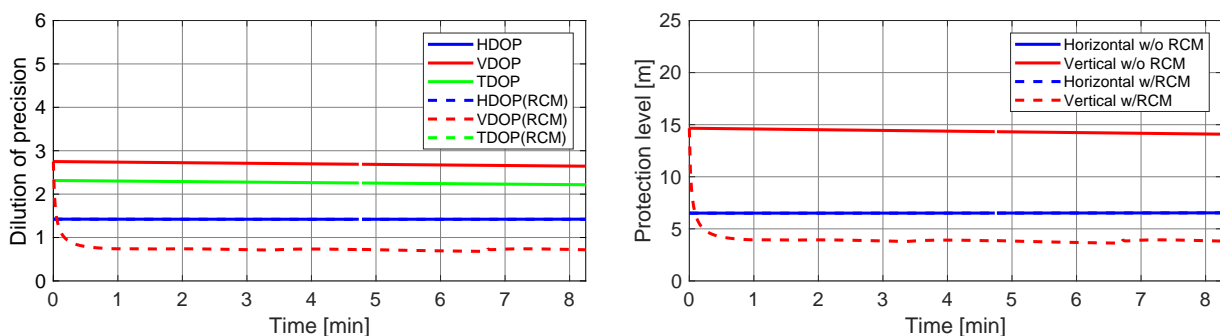


Figure 4.16: Dilution of precision (DOP) values and protections levels with (dashed lines) and without (solid lines) clock modeling (RCM) of receiver connected to the Jackson Labs CSAC, analyzed by means of a sequential least-squares adjustment using a piecewise linear clock polynomial. Note that the TDOP values as well as the horizontal values coincide in both depictions with and without RCM.

compared to the results shown in Figures 4.11b and 4.18b, it can be seen that sequential RCM decreases the external reliability values even more. To be exact, 95% of the values are smaller than 0.053 m/s, which is an improvement of ca. 70% compared to the values computed without RCM.

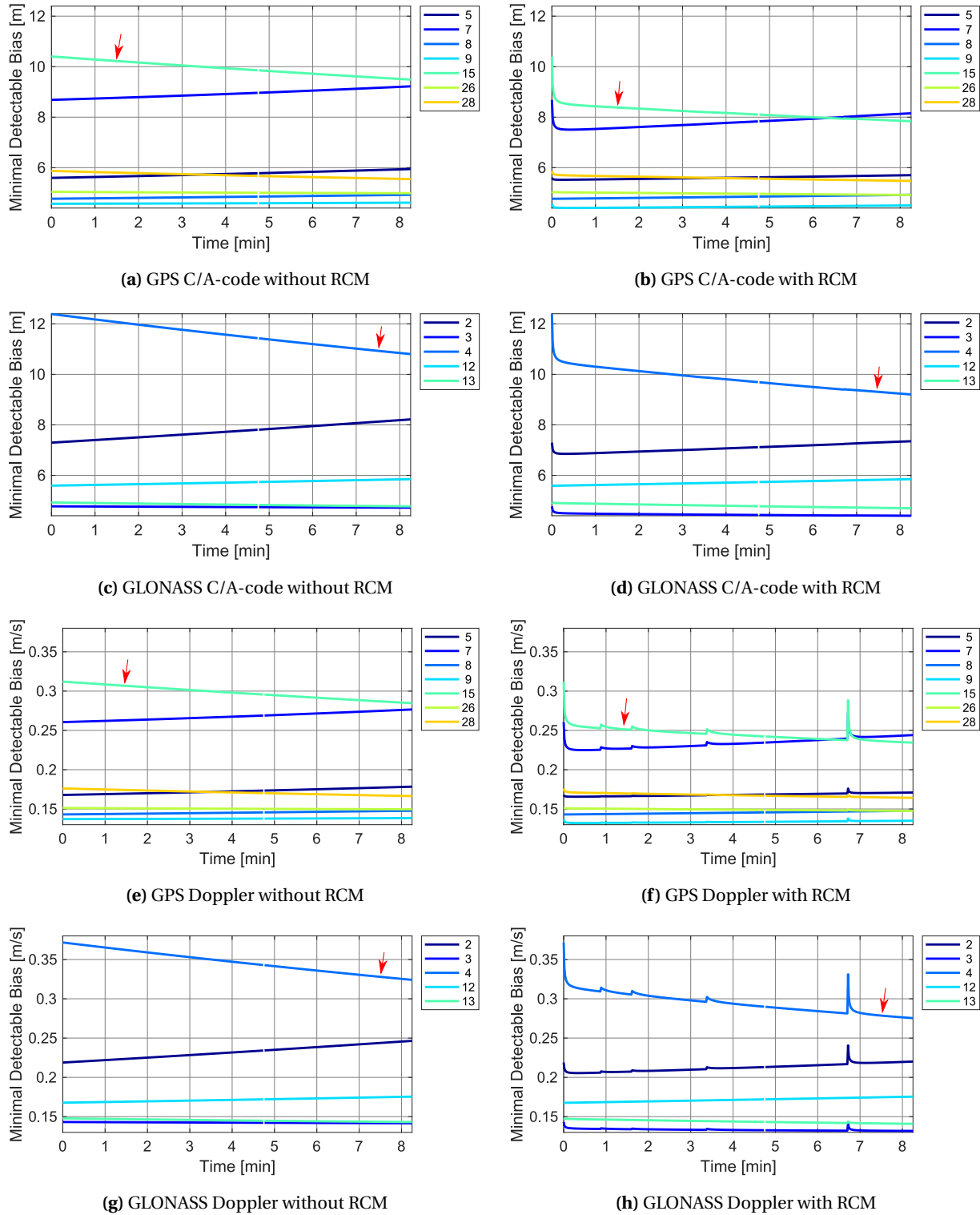


Figure 4.17: Color-coded/satellite-dependent GPS and GLONASS L1 C/A-code and Doppler internal reliability with and without receiver clock modeling (RCM) of receiver connected to the Jackson Labs CSAC, analyzed by means of a sequential least-squares adjustment using a piecewise linear clock polynomial; satellites exhibiting maximum improvements are indicated by a red arrow

Table 4.4: Average minimal detectable biases (MDBs) of GPS (G) and GLONASS (R) L1 C/A-code and Doppler observations with and without receiver clock modeling (RCM) of receiver connected to the Jackson Labs CSAC, computed by a sequential least-squares adjustment using a piecewise linear clock polynomial. Positive or negative ratios mean an improvement or a degradation, respectively, due to RCM.

Satellite	Elevation angle [°]	C/A-code MDB			Doppler MDB		
		w/o RCM [m]	w/RCM [m]	Ratio [%]	w/o RCM [m/s]	w/RCM [m/s]	Ratio [%]
G05	51.4	5.752	5.602	3	0.173	0.168	3
G07	28.7	8.922	7.787	13	0.268	0.233	13
G08	58.3	4.842	4.842	0	0.145	0.145	0
G09	69.4	4.588	4.448	3	0.138	0.133	3
G15	28.1	9.924	8.151	18	0.298	0.244	18
G26	65.9	5.010	4.970	1	0.150	0.149	1
G28	49.9	5.696	5.582	2	0.171	0.167	2
R02	40.4	7.736	7.077	9	0.232	0.212	9
R03	73.8	4.745	4.436	7	0.142	0.133	7
R04	23.1	11.549	9.782	15	0.346	0.293	16
R12	56.5	5.715	5.714	0	0.171	0.171	0
R13	63.4	4.840	4.793	1	0.145	0.144	1

Positioning and Navigation with Three Satellites

GNSS-based positioning usually requires at least four satellites in view. In harsh environments such as urban canyons, this might not be possible since satellites with low elevation angles are either not observable at all or potentially suffer from severe multipath and diffraction effects. Thanks to the high frequency stability of a CSAC its behavior can be predicted over certain time intervals much longer than a couple of seconds. This ultimately enables the computation of a position and velocity solution with only three satellites in view. Such an approach is referred to as *clock coasting* (Knable and Kalafus, 1984; Sturza, 1983), which can also be extended to the highly stable inter-system biases in case multi-GNSS observations are used.

In order to evaluate and validate this method, artificial partial satellite outages are generated so that only two GPS satellites and one GLONASS satellite remain in view. In case a partial satellite outage occurs, additional clock and ISB corrections are computed, i.e. predicted, based on the latest clock

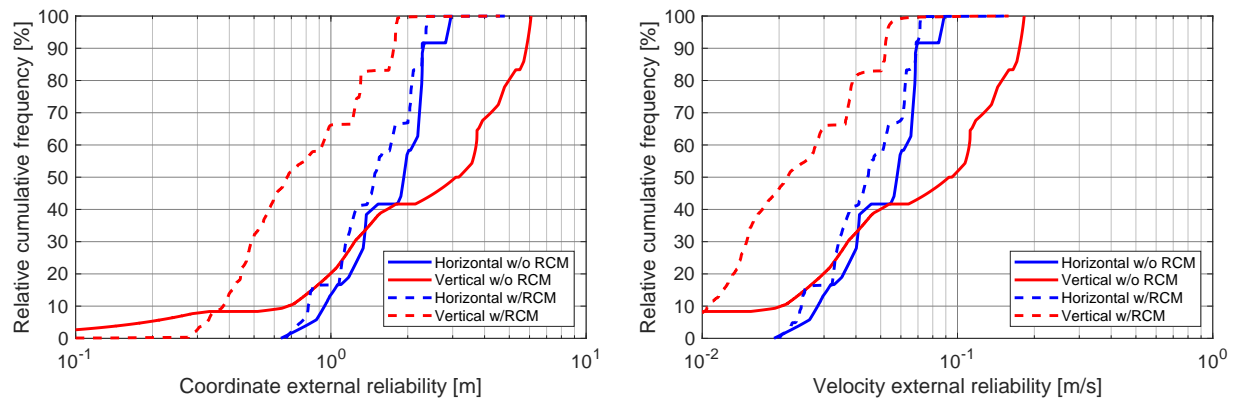


Figure 4.18: External reliability of coordinate and velocity estimates with (dashed lines) and without (solid lines) receiver clock modeling (RCM) of receiver connected to the Jackson Labs CSAC, analyzed by means of a sequential least-squares adjustment using a piecewise linear clock polynomial

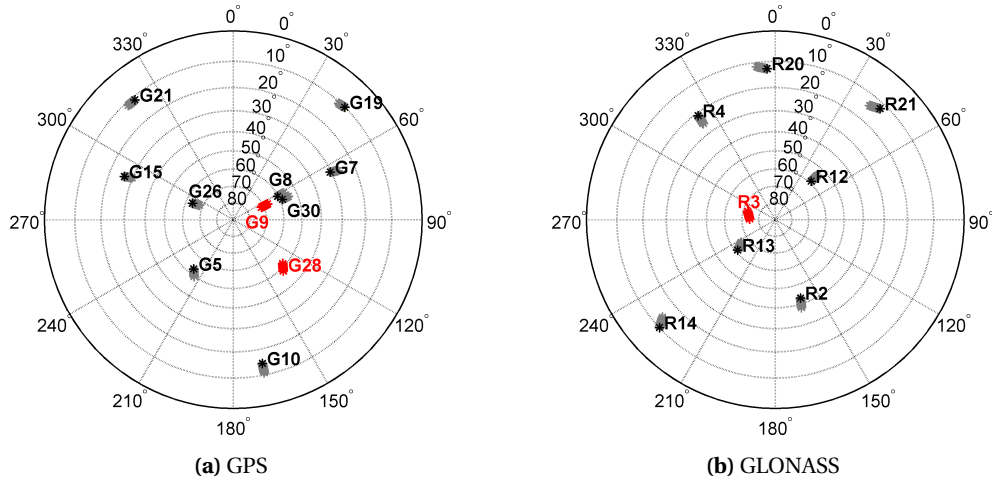


Figure 4.19: Spatial satellite distribution when navigating with only three satellites, where gray satellites are disabled and only red satellites (G9, G28, R3) remain in view.

and ISB coefficients, respectively. Subsequently, these corrections are applied to the respective code and Doppler observations. In other words, the clock and ISB biases of the receiver are treated like "usual" observation errors such as satellite clock corrections, cf. also Equations (2.3) and (2.4). Thus, only three satellites are sufficient to compute a position and velocity solution. Using the example of the receiver connected to the Microsemi CSAC, three such satellite outages are generated from second ten to 60, as well as from minute two to three and minute five to seven. During these periods only

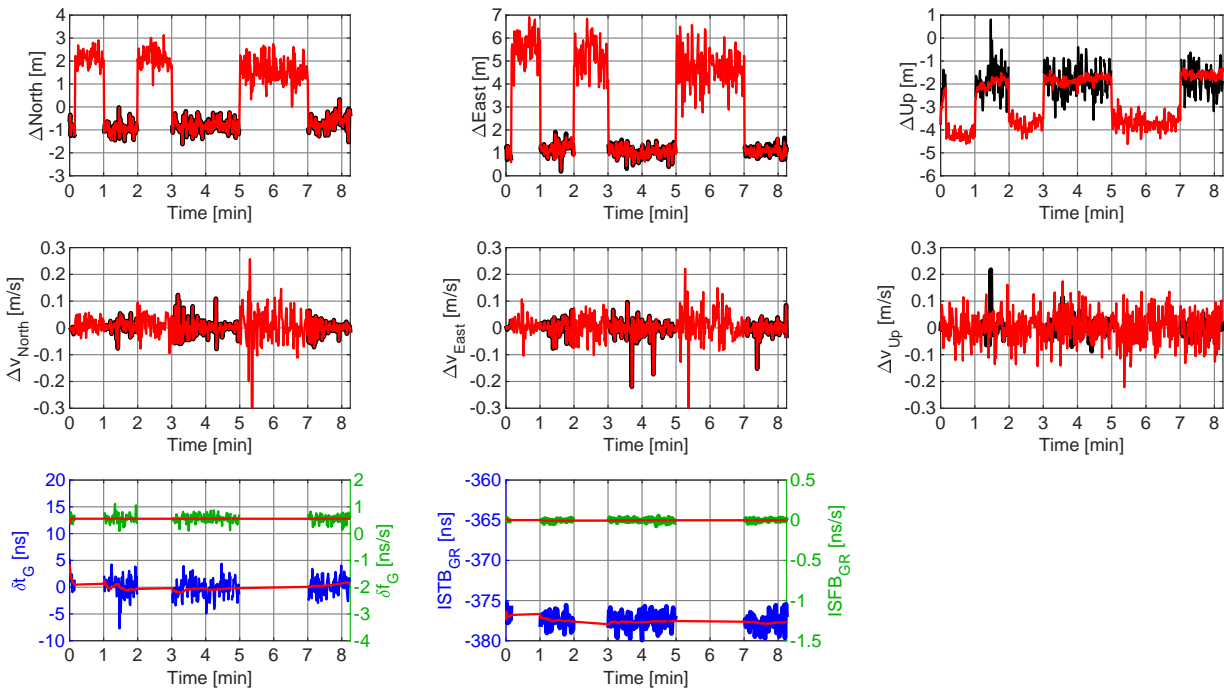


Figure 4.20: Times series of topocentric coordinate (upper row) and velocity (middle row) deviations relative to reference solution, as well as clock time offset after a straight line fit, clock frequency offset, inter-system time and frequency biases (bottom row) of receiver connected to the Microsemi CSAC, depicted without and with receiver clock modeling in black and red, respectively, including three periods of clock coasting and inter-system bias modeling; analyzed by means of a sequential least-squares adjustment using a piecewise linear clock polynomial. Note the different y-axes scalings of the vertical components.

GPS satellites G09 and G28 as well as GLONASS satellite R03 are visible. Each of these satellites has average elevation angles of at least 50° as depicted in Figure 4.19. The three artificial outages not only enable testing of the effects of different outage lengths. Moreover, the convergence behavior of the clock and ISB coefficients can be investigated by means of the first outage that occurs right after the start of navigation. After each satellite outage, new clock and ISB modeling segments are started. The results of the three partial outages are shown in Figure 4.20.

At first, it can be seen that the proposed method of positioning with three satellites works perfectly fine. The overall noise of the coordinate time series is increased during the outages because only three satellites in very high elevation angles are visible. Whereas the horizontal coordinates become two to four times noisier, the vertical coordinate noise is only slightly increased compared to the rest of the clock modeling time series. However, the up-coordinates without RCM are still noisier than the ones during the outages. One reason for this is the fact that during clock coasting the observation geometry gets closer to true ranging since no clock errors are estimated explicitly. In this case, the vertical coordinate is better observable than the horizontal ones (Kuang et al., 1996; Santerre et al., 2017). Furthermore, the availability of only three satellites during the outages causes offsets in the north, east and up coordinates of approximately 2 m, 5 m and -4 m, respectively. The velocity estimates are hardly affected at all, either with or without clock modeling, cf. also Figure 4.13b.

The occurrence of the first artificial outage after ten seconds is handled very well by the proposed method since both clock and ISB coefficients already converged to relatively stable values. There are no significant differences in the coordinate and velocity estimates visible between the three different outage lengths. However, care has to be taken in case the oscillator in use suffers from a frequency drift, so that at some point during clock coasting the additional clock correction – only accounting for time and frequency offset – does not reflect the "true" clock biases anymore. Therefore, it is recommended to apply this approach only for short periods of time, and of course not beyond the theoretical physically meaningful maximum modeling interval.

Impact of a Sliding Window

Since the positive effects of sequential receiver clock modeling do not equally increase with progressing time, it is reasonable to question whether it is necessary to use such long modeling intervals derived from the temporal stability of the oscillators as listed in Table 3.4. Therefore, the application and impact of a sliding window is investigated in the following.

A sliding window restricts the clock modeling interval to the window length – assuming that the theoretical interval is larger than the window length. In other words, the overall memory length of the SLSA is kept at a constant value after initialization and does not increase beyond that. Based on results of sequential RCM already discussed in this section, window lengths of ten, 30 and 60 seconds are chosen. The vertical coordinate and velocity estimates as well as the clock biases of the receiver connected to the Jackson Labs CSAC are depicted in Figure 4.21. Note that the horizontal components are not shown here since clock modeling has no effect on them in the case at hand. The increase of the window length from 10 s to 60 s shown in Figures 4.21a to 4.21c is accompanied by a decrease of the high frequency coordinate deviations. Whereas the differences between the ten-second window and the 30-second window are clearly visible, the 60-second window does not yield any real distinct advantage over the 30-second window. There also appears a slight "delayed" peak in the clock frequency bias at approximately 5.5 minutes due to the relatively short modeling interval, that is the sliding window length. On the part of the velocity estimates, hardly any differences between the three window lengths are noticeable. This comes as no surprise since the clock frequency offset estimate does not depend on the temporal length of the piecewise linear clock model.

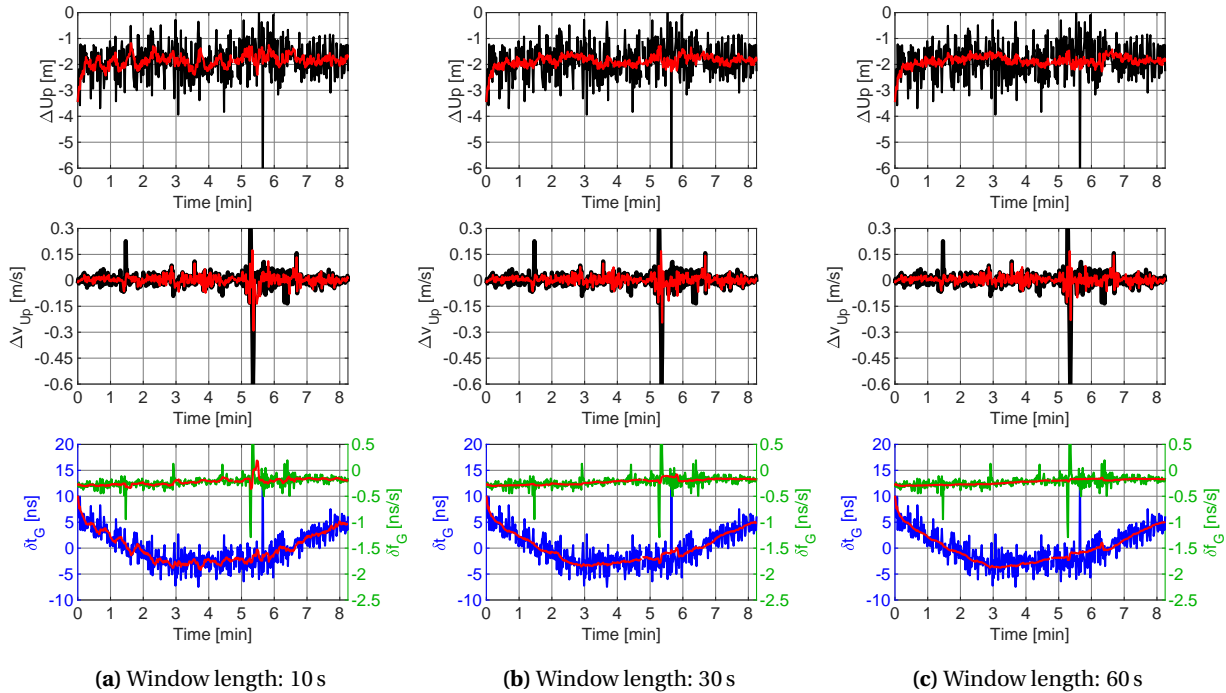


Figure 4.21: Times series of topocentric vertical coordinate and velocity deviations relative to reference solution as well as clock biases of receiver connected to the Jackson Labs CSAC, depicted without and with receiver clock modeling in black and red, respectively; analyzed by means of a sequential least-squares adjustment using a piecewise linear clock polynomial and a sliding window of different lengths. Note the different y-axes scalings of the vertical components.

In conclusion, by insignificantly degrading the effects of RCM, a sliding window with a length of 30 to 60 seconds minimizes some of the drawbacks of the proposed sequential clock modeling approach. On the one hand, the frequency drift of an atomic clock can be accounted for without any additional checks, e.g. a hypothesis test, assuming that such a drift is less pronounced within the length of the sliding window, which typically should be the case for an atomic clock of any kind. The overall computation time, on the other hand, is reduced to a level where clock modeling becomes real-time applicable. More on this topic can be found in section 4.4. Therefore, in case sequential RCM is applied, it is recommended to use a sliding window with a length of 30 s to 60 s instead of a fixed maximum modeling interval with or without hypothesis testing for frequency drifts. Of course, this implies that the theoretical maximum modeling interval is larger than the sliding window. If that is not true, the sliding window length should be shortened accordingly to ensure physically meaningful clock modeling.

4.4 Real-time Applicability

4.4.1 Software Receiver

The analysis shown in section 4.3 has been carried out in post-processing, despite the fact that the approach of RCM in an SLSA was originally designed for real-time applications. In order to proof the real-time applicability of the clock modeling concept as proposed in section 3.3.2, the algorithm has to be implemented into a GNSS receiver. However, this is virtually impossible for a conventional user since there is no easy access to the firmware of a typical commercial receiver; let alone the low-level programming that is necessary for the implementation. This kind of GNSS receiver can be referred

to as *hardware receiver* since all signal processing (down conversion, analog-to-digital conversion, acquisition, tracking, etc.) is based on integrated circuits like field-programmable gate arrays (FPGAs) or application-specific integrated circuits (ASICs) (Pany, 2010). On the one hand, such receivers work highly efficient because they are solely designed for the purposes of a GNSS receiver. On the other hand, however, they are not very flexible in terms of implementing different or new signal processing algorithms. This problem or challenge, respectively, can be overcome by using a software-defined radio (SDR) also referred to as *software receiver*. Developments of such devices started some 20 years ago and ultimately led to first real-time SDRs in the early 2000s (Kibe et al., 1996; Pany, 2010).

The basic architecture of an SDR is depicted in Figure 4.22. The similarities with a hardware receiver extend to down conversion of the GNSS signals from radio frequency to intermediate frequency (IF) level and their analog-to-digital conversion inside the front end. After transferring the digital signal samples to a general-purpose computer – typically via Universal Serial Bus (USB) –, all subsequent processing steps are carried out in software on the computer central processing unit (CPU) and graphics processing unit (GPU) from that point on. In comparison to a hardware receiver, this enables a high degree of flexibility in signal processing. However, since the microprocessors of a typical computer are not designed for a specific purpose but a variety of applications, the hardware and power demands of a software receiver are much higher in order to achieve the same level of performance as a pure hardware receiver. For more information on software receiver technology it is referred to Pany (2010).

In order to test the real-time applicability of the proposed approach of RCM, the IfEN SX3 software receiver, version 3.3.0 is used (IfEN GmbH, 2017), in combination with the IfEN NavPort-4 front end. This software provides several application programming interfaces (APIs) through which user algorithms can be implemented in a relatively easy way. As shown by Figure 4.23, a total of six APIs are available as described by Table 4.5. The *Navigation API* is used for the purposes of this thesis since it gives access to GNSS observations including code and Doppler. Furthermore, both satellite orbits and satellite clock errors (and their respective accuracies), tropospheric and ionospheric corrections are provided. The relativistic correction is already included in the satellite clock correction.

These real-time data are used to implement a PVT algorithm that computes two consistent solutions: (1) a conventional least-squares navigation solution, (2) an SLSA with receiver clock modeling as proposed in section 3.3.2, both based on GPS L1 C/A-code and Doppler observation with an elevation-dependent weighting scheme according to Equation (4.10). Instead of solution 1, the receiver internal solution could also be used. However, this would lead to an inconsistent comparison with the RCM solution since the user has no knowledge about the exact implementation of the internal solution. The SLSA solution applies a parameter pre-elimination scheme and a sliding window to decrease computation time, cf. section 3.3.2. Otherwise the latter would exceed the sampling interval eventually due to the constantly growing parameter vector of the sequential approach. In that case, real-time applicability could not be assured anymore. As already investigated in section 4.3.3, this decrease of the clock modeling interval does not degrade the impact of clock modeling on the PVT solution.

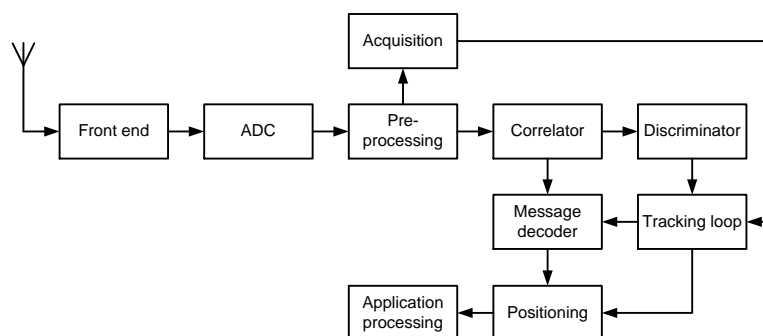


Figure 4.22: Basic architecture of a software-defined radio according to Pany (2010)

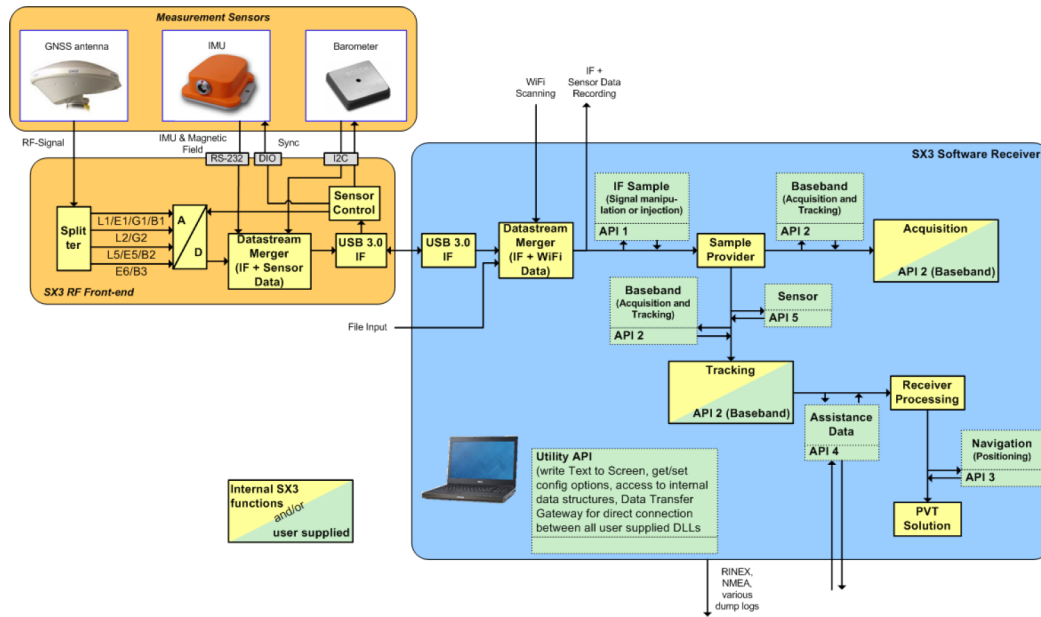


Figure 4.23: Placement of application programming interfaces (APIs) within the IfEN SX3 software receiver architecture (IfEN GmbH, 2017, p. 219)

The algorithm is written in C/C++ using *Microsoft Visual Studio 2017*. After compiling a *dynamic-link library*, it can be activated via the graphical user interface of the software receiver. The user can determine various processing parameters by means of a configuration file. This file covers general settings such as the elevation cutoff angle, a priori standard deviations for the observations, and statistical measures (confidence level, detection power, etc.) for outlier detection. Moreover, the maximum clock modeling interval, relative constraints between consecutive clock segments as well as the length of the sliding window can be configured.

4.4.2 Pedestrian Experiment

The practical validation of the RCM implementation was carried out by means of a pedestrian experiment on the rooftop of the Geodetic Institute at Leibniz Universität Hannover, Germany on June 24, 2016. In contrast to previous experiments presented in section 4.3, only the Microsemi CSAC was used as an external clock due to both power and mobility restrictions. This oscillator was connected to the IfEN NavPort-4 front end, both powered by a USB powerbank. The GNSS signals received by a navXperience 3G+C antenna mounted on a short stick were converted to IF samples by the front end and subsequently streamed to a laptop on which the IfEN SX3 software was running. Apart from true real-time processing during the experiment, the IF data was also recorded by the laptop so that the experiment could be repeated with different settings in post-processing without having to conduct

Table 4.5: IfEN SX3 software receiver application programming interfaces (APIs)

API name	Description
IF Sample	Access to IF samples
Baseband	Control over signal acquisition and tracking
Assisted	Access to navigation data (ephemeris, almanac, etc.)
Utility	Access to receiver internal parameters and functions
Sensor	Retrieval of external sensor data, e.g. from an IMU
Navigation	Access to raw GNSS measurement data

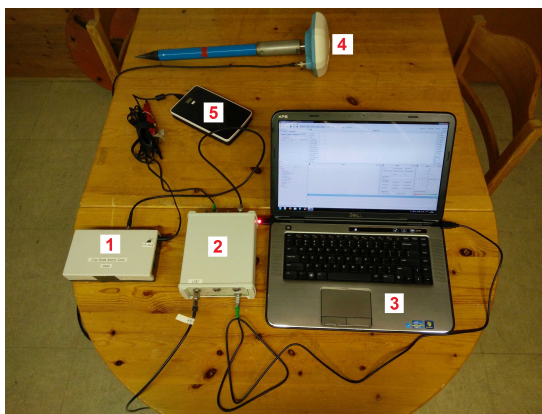


Figure 4.24: Main parts of the measurement configuration of the pedestrian experiment: (1) Microsemi CSAC, (2) IfEN NavPort-4 front end, (3) Laptop running IfEN SX3 software receiver, (4) navXperience 3G+C antenna mounted on a stick, (5) USB powerbank

the experiment again. Due to partly severe shadowing and multipath effects, an elevation cutoff angle of 30° was applied. The length of the sliding window was set to 30 seconds, thus RCM was also limited to that interval.

In addition to the measurement configuration shown in Figure 4.24, a *JAVAD Sigma Qua-G3D* receiver was inserted via an active signal splitter downstream of the GNSS antenna. The data from this receiver were used in combination with those from a nearby local reference station – consisting of a *Leica AR25.R3 LEIT* antenna and a *JAVAD Delta TRE-G3T* receiver – to generate a reference solution for the experiment based on carrier phase observations. The corresponding trajectory depicted in Figure 4.25 is computed based on GPS and GLONASS phase and Doppler observations using *Terratec TerraPOS 2.4.0*. Approximately 80% of the phase ambiguities are fixed. The overall trajectory exhibits mean three-dimensional coordinate and velocity standard deviations of 0.051 m and 0.097 m/s, respectively. These values seem reasonable and expectable since there were severe shadowing effects at times during the experiment.

Both the reference trajectory and the solutions from the software receiver are converted into a topocentric coordinate system which originates in the reference trajectory at each epoch. The resulting coordinate and velocity deviations with and without clock modeling are depicted in Figure 4.26. In general, the SDR solutions are distinctly noisier than the SPP solutions discussed in section 4.3, which is mainly due to the fact that the observations of the software receiver are much noisier than the ones of the geodetic JAVAD receivers. The coordinate offsets of approximately -2 m, 2 m and 5 m in north, east and up, respectively, are most likely caused by remaining ionospheric effects. Similar to the results presented in preceding sections, receiver clock modeling almost exclusively affects the vertical com-



Figure 4.25: Trajectory of the pedestrian experiment, where the reference station is indicated by a red triangle

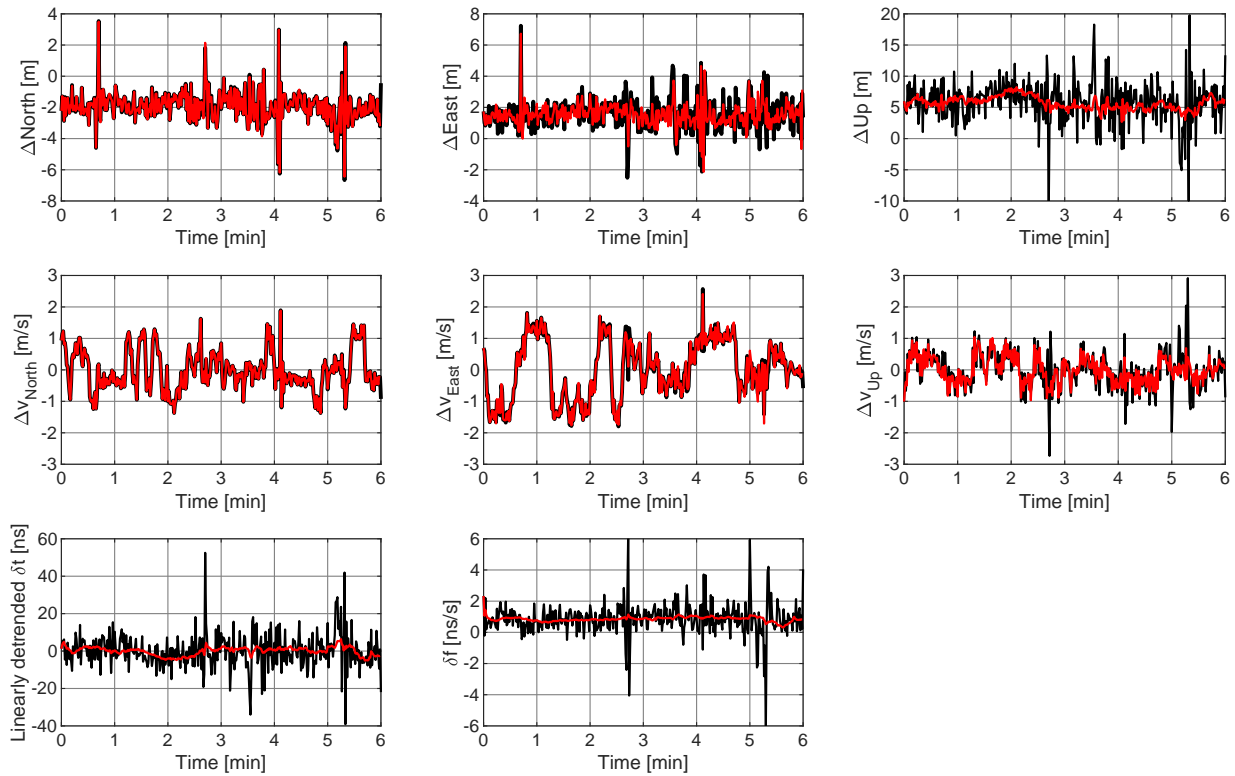


Figure 4.26: Times series of topocentric coordinate (upper row) and velocity (middle row) deviations relative to reference solution, as well as clock time offsets after a straight line fit and clock frequency offsets (bottom row) of software receiver connected to the Microsemi CSAC, depicted without and with receiver clock modeling in black and red, respectively

ponents. In this case, also the east coordinate is slightly affected. The overall precision of the vertical coordinate and velocity estimates is improved by approximately 85% and 45%, respectively, when applying RCM. Furthermore, the largest coordinate and velocity deviations at minutes 2.7 and 5.3 are significantly reduced thanks to receiver clock modeling. The increased noise of the SDR observations is also present in the Doppler measurements. Their noise level is much higher so that velocity estimation also benefits from RCM even when using the Microsemi CSAC.

In order to evaluate its real-time applicability, the runtime of the algorithm was also recorded during the experiment, when the software was running on an Intel Core i7-2600 CPU. The diagram in Figure 4.27 shows an exponential runtime increase up to ca. 70 ms at a processing time of 30 seconds. From that point on, the sliding window prevents a further increase as it was intended for. By improving the source code and using a more powerful computer, the performance of the RCM algorithm could

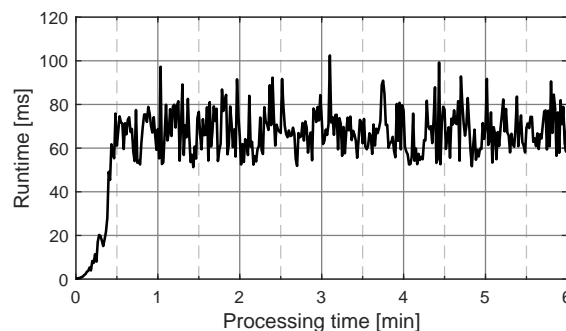


Figure 4.27: Runtime performance of sequential least-squares receiver clock modeling algorithm in IfEN SX3 software receiver (running on an Intel Core i7-2600 processor) during pedestrian experiment

be further enhanced. Nevertheless, its current status already shows its inherent potential. It could be of great value in real-time applications where clock modeling by means of a filter solution – which is usually predestined for real-time applications – is not possible or, indeed, prohibited.

4.5 Spoofing Detection

4.5.1 Introduction

Signal interference caused by jamming and spoofing are major threats to GNSS-based PNT services (Volpe, 2001). This includes spatial applications (positioning, navigation) such as location-based services and fleet management, as well as timing and synchronization applications, e.g. in telecommunication networks, financial transactions and power grid operations. Jamming and spoofing are especially dangerous in safety-critical applications, for example in aviation and seafaring (Günther, 2014). Whereas jamming aims for preventing receivers from acquiring and tracking GNSS signals in a certain area by transmitting signals of sufficiently high power, spoofing intends to capture a receiver so that it locks onto the false signals of a so-called *spoofers* instead of the *authentic* satellite signals, thus pulling it away from its true (position and time) solution. Therefore, spoofing is a much more severe threat than jamming because the target receiver is unaware of the presence (and location) of an interference source. However, spoofing is much more difficult to succeed than jamming. Although these *authentication* issues have been well known since the beginnings of GPS, they have become more severe in recent years due to two reasons: (a) the number of services that rely on accurate GNSS positioning and timing has been greatly increased, thus making them a more profitable target; (b) cheap jamming and spoofing devices are available on the open market for almost everyone. Consequently, the biggest challenge for a so-called *jammer/spoofers* are not the hardware requirements anymore, but the knowledge about how to plan, implement and execute a successful attack.

Although there are only few reported incidents of malicious spoofing attacks, the scientific efforts at the University of Texas resulted in two successful experiments. In 2012 an unmanned aerial vehicle (UAV) was captured and forced to land as intended by the spoofer (University of Texas, 2012). One year later in 2013, this method was extended and applied to an even bigger object by taking over control of the course of a yacht at sea (University of Texas, 2013). Besides such intentional attacks, also unintentional spoofing can take place, for example by means of a GNSS repeater. Such a device simply replays signals inside a building that were received by an outside antenna. A typical application field is the use in an aircraft hangar. Here, they enable testing of on-board GNSS navigation equipment without having to move the aircraft outside. However, in case such a repeater is not properly installed, it can cause an aircraft to lock onto the repeater signals during take-off or touchdown (Steindl et al., 2013), which is a severe threat in aviation safety.

Researchers have addressed the detection and mitigation of GNSS jamming and spoofing years prior to these reported incidents (McDowell, 2007; Montgomery et al., 2009). One important role within such receiver-sided methods is always assigned to the receiver clock. If a very stable oscillator, like e.g., an atomic clock is used instead of the built-in quartz oscillator, the delays induced by a spoofer could be separated from the (integrated) random frequency fluctuation of the oscillator more easily (Jafarnia-Jahromi et al., 2013). On the part of the satellites, GNSS transmit *encrypted* signals, e.g. GPS P(Y)-code and Galileo PRS signals, next to the civil signals, which minimizes unauthorized access to these signals to a large extent. In addition, newer systems use *authenticated* signals such as Galileo E6 CS (Hernández et al., 2015). The difference between these two methods is the fact that encryption requires the receiver to know about the underlying scheme, usually by means of a decryption key. Moreover, once this scheme is decoded or hacked, respectively, the signal can also be spoofed. Signal authentication is especially important with regard to the integrity requirements of safety-critical applications.

4.5.2 Meaconing Experiment

Background and Basic Idea

When a spoofer tries to occupy the signal tracking loops of a target receiver and then pull its PVT solution away from the true/authentic position, a common delay caused by the spoofed signals is injected into the solution and typically absorbed by the receiver clock bias estimates. In order to not be detected by the target receiver, this spoofed delay therefore must not deviate significantly from the authentic receiver clock bias. In other words, the initially injected delay must be as small as possible so it cannot be separated from the (integrated) random frequency fluctuations of the oscillator driving the receiver. This also means that very small injected delays are very hard to be detected by the receiver.

Such a spoofing attack can be simulated in a controlled environment by means of a meaconing experiment using a GNSS repeater. The basic idea of this experiment was proposed by Marnach et al. (2013) but applies a different method of spoofing detection than proposed in the following. Here, the experiment consisted of two JAVAD Delta TRE-G3T receivers, one driven by its internal quartz oscillator and one connected to a Microsemi CSAC. Both receivers were recording the same GNSS signals via a signal splitter. The input signal of the latter comes from an active coaxial switch which allows to switch between two different *static* antennas in an instant. One of them, an active AuCon L1/L2 antenna, was connected to a GNSS repeater (*spoofer antenna*) which generated an additional delay; its output signals are transmitted via cable to the coaxial switch. When switched to the second antenna without repeater (*authentic antenna*), a Leica AR25.R3, both receivers recorded authentic signals. When switched to the repeater, they recorded spoofed signals. The complete measurement configuration is depicted in Figure 4.28.

Whenever the signal path is switched from the authentic antenna to the spoofer antenna, this should result in a jump in the clock bias time series. With the help of the known frequency stabilities of the used oscillators, a hypothesis test for the significance of such a clock bias jump can be established. The distance between the two antennas varied from a minimum of approximately two meters to a maximum of ca. 25 meters in four different setups, where the authentic antenna always stayed in the same location. Thus, delays of different magnitude were introduced into the receivers – in addition to the repeater delay. It can be assumed that a short delay of 2 m (7 ns) is more difficult to be detected by the receivers than a delay of 25 m (83 ns). In each setup, it was alternated between the two antennas every two minutes, recording GNSS data with a sampling rate of 10 Hz.

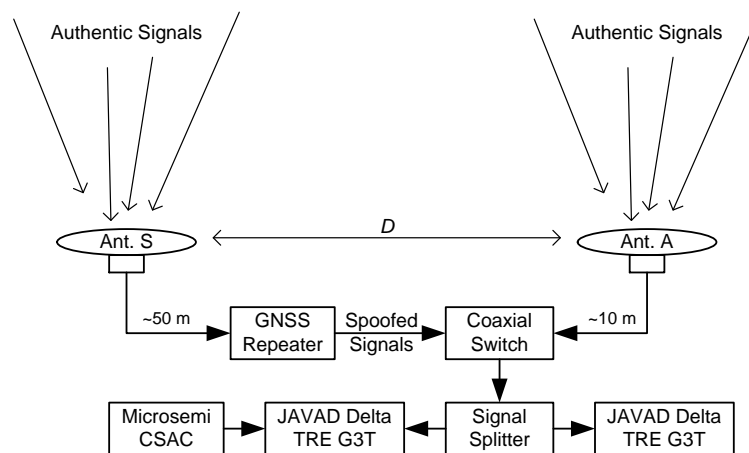


Figure 4.28: Measurement configuration of meaconing experiment, where distance D between the spoofer antenna (Ant. S) and the authentic antenna (Ant. A) amounts to approximately 2 m, 14 m, 25 m and 40 m, respectively

Analysis Strategy

The proposed concept of detecting a meaconing attack is based on monitoring the receiver time offset δt and frequency offset δf in a Kalman filter. As discussed in section 3.3.1, the filter approach enables a simple incorporation of frequency stability measures of the respective oscillator in use by means of an appropriate clock process noise model. In the second recursive step of a Kalman filter, the consistency between the measurements and the system model is checked by means of the innovations and their variances, cf. Equations (2.64) and (2.65). More precisely, the predicted clock states are compared against the measured clock states as provided by the receiver. Subsequently, these innovations are checked for their significance by means of a hypothesis test. If the test fails in three consecutive epochs, a spoofing attack is deemed to be detected – assuming that the receiver was not spoofed until this point. The underlying filter concept is based on state vector

$$\mathbf{x}_k = \begin{bmatrix} \delta t_k \\ \delta f_k \end{bmatrix} \quad (4.11)$$

at a given epoch k . The prediction step uses the state transition matrix

$$\Phi_{k,k+1} = \begin{bmatrix} 1 & \Delta t \\ 0 & 1 \end{bmatrix} \quad (4.12)$$

and the process noise model according to Dierendonck et al. (1984) described by Equation (3.23) with the h_α -coefficients listed in Table 3.5 for the Microsemi CSAC and typical values of an TCXO ($h_0 = 2.0 \cdot 10^{-18}$, $h_{-1} = 7.2 \cdot 10^{-19}$, $h_{-2} = 1.5 \cdot 10^{-19}$) for the internal oscillator, respectively. The observations in the measurement update step are real-time clock biases computed internally by the receiver. Therefore, the design matrix is a 2×2 identity matrix. The receiver internal solution also provides standard deviations for the clock biases which are used to define the observation weight matrix and cofactor matrix, respectively.

The hypothesis test for spoofing detection is based on the assumption that the innovations do not deviate from zero significantly. In other words, if the measured clock biases deviate too much from the system model – which is mainly driven by the clock model –, the hypothesis test will reject this assumption. The corresponding null and alternative hypothesis H_0 and H_A , respectively, read

$$H_0 : E \left\{ d_{\delta t, k}^2 \right\} = 0, \quad (4.13)$$

$$H_A : E \left\{ d_{\delta t, k}^2 \right\} \neq 0. \quad (4.14)$$

The test statistic

$$\mathcal{T}_k = \frac{d_{\delta t, k}^2}{\sigma_{dd, \delta t, k}^2} \sim \chi_{1, 1-\eta/2}^2 \quad (4.15)$$

is computed based on the clock time offset innovation $d_{\delta t}$ and its variance $\sigma_{dd, \delta t}^2$ at each epoch. The χ^2 -distributed confidence level is assessed to 99% for this test, thus $\eta = 0.01$. If the test fails, i.e. H_0 is rejected, in three consecutive epochs, the respective start or end of a spoofing attack is assumed to be detected. Subsequently, the Kalman filter is reinitialized.

Results

The resulting receiver clock bias time series of two measurement setups – with station distances of approximately 2 m and 14 m – are depicted in Figure 4.29 exemplarily. In both setups, the clock bias

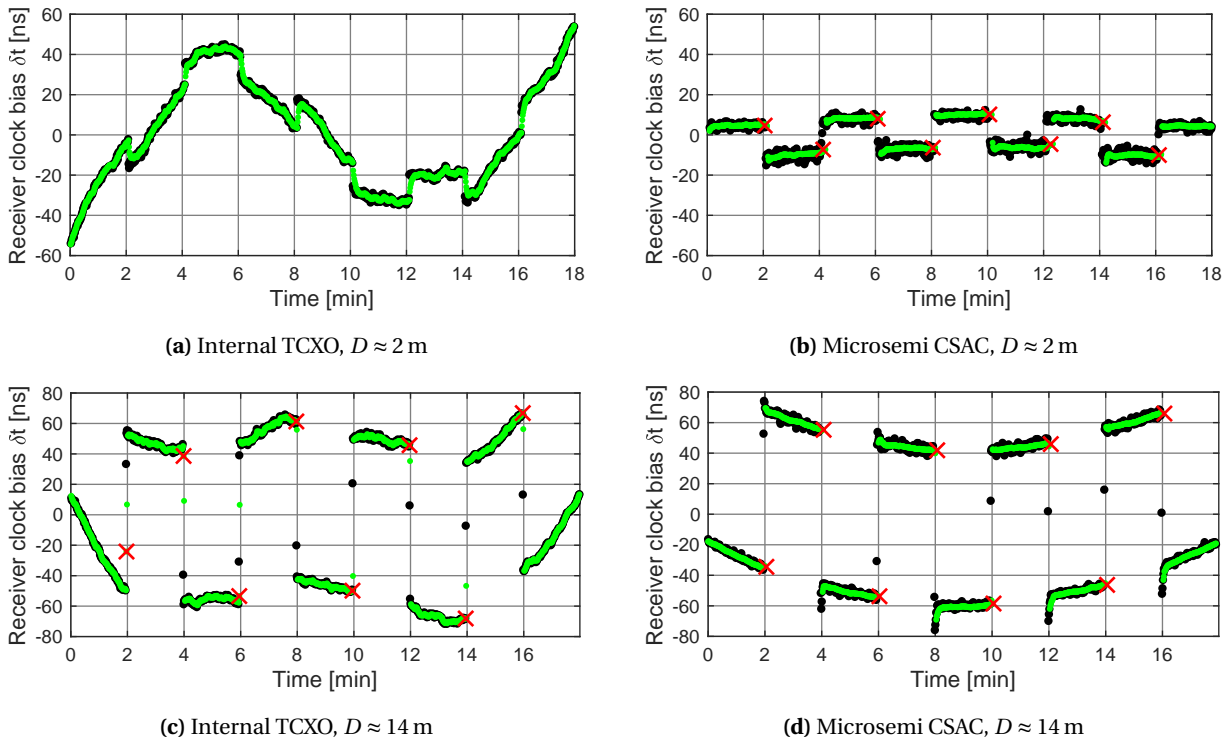


Figure 4.29: Original (black dots) and predicted (green dots) receiver time offset states after a straight line fit from a receiver driven by its internal TCXO and a receiver connected to a Microsemi CSAC. The distance between the spoofer antenna and the authentic antenna is denoted by D . Each red cross indicates a detected start or end of a spoofing attack.

jumps in each time series are visible for both the internal oscillator and the CSAC. This especially applies to the 14-meter baseline of both receivers (Figures 4.29c and 4.29d) and the short two-meter baseline of the receiver connected to the CSAC.

In case of the results of the receiver driven by its internal oscillator on the two-meter baseline, the hypothesis test always accepts the null hypothesis. That means that from a statistical point of view no spoofing attack is detectable. The reason for this is the fact that these small signal delays cannot be properly separated from the random integrated frequency deviations caused by the low frequency stability of the TCXO. The corresponding clock bias jumps could also be attributed to changes of the observation geometry, for example in case the number of visible satellites increases or decreases. On the contrary, thanks to the much higher frequency stability of the CSAC, every start and end of the four simulated spoofing attacks are detectable by the algorithm.

With regard to the station distance of ca. 14 m, the results shown in Figures 4.29c and 4.29d indicate that all meaconing occurrences can be detected by both receivers either connected to the CSAC or driven by the internal oscillator. The seven times increased spatial distance between the two antennas leads to such big clock bias jumps that the spoofing detection algorithm is capable of revealing all of the simulated meaconing attacks – even if no atomic clock is connected to the respective receiver.

Conclusively, it can be stated that the proposed anti-spoofing algorithm improves the detection of small delays injected by a spoofer if a chip-scale atomic clock is used instead of the receiver internal crystal oscillator.

5

Conclusions

5.1 Summary

The advances in clock and oscillator technology resulted in the development and commercial distribution of so-called chip-scale atomic clocks (CSACs) in recent years. Although miniature atomic clocks were available before that, these clocks pushed the limits of miniaturization much further. Their small size and low power consumption combined with an accuracy and a stability far superior to those of conventional quartz oscillators used in commercial GNSS receivers, make them very suitable for kinematic GNSS-based application. The practical evaluation of this relatively new opportunity was the primary purpose of this thesis, subdivided into three main parts or tasks, respectively, that is (a) the discussion of technical requirements, (b) the definition of an appropriate model for clock modeling, and (c) the practical validation of that model. The most important investigations and findings are summarized in the following.

The task of synchronizing the satellite timescales with its own is essential for a single receiver using one-way range measurements in position, velocity and time determination. The technical requirements an oscillator has to meet to be used in such a receiver, are already fulfilled by low-cost crystal oscillators. The major drawback although is the fact that the behavior of such an oscillator cannot be predicted over time intervals greater than roughly one second. However, compared to the requirements for satellite clocks, this is not a necessary feature. Then again, in the simplest case, the receiver clock bias has to be estimated every observation epoch together with the coordinates. If a more stable external clock such as a CSAC, is used instead, its superior stability can be used to constrain the temporal variations of the clock bias, which is referred to as receiver clock modeling (RCM). If the integrated frequency noise of the oscillator in use is smaller than the receiver noise, physically meaningful RCM is possible, which is especially beneficial in kinematic applications. Changes in the receiver hardware delays, e.g. due to changes of ambient temperature, have to be considered theoretically; practically, they should be no limitation for RCM assuming they do not change abruptly.

In order to adequately model the behavior of four different oscillators – namely a Jackson Labs LN CSAC providing a raw and an enhanced OCXO signal, an SRS PRS10 rubidium standard, and a Microsemi CSAC –, in GNSS parameter estimation, their individual frequency stabilities were characterized by means of extensive comparison measurements with an active hydrogen maser. The results of the frequency stability analysis showed an overall good agreement with manufacturer's data in terms of the corresponding time-domain Allan deviations. In the frequency domain, the determined PSD estimates were used to compute spectral coefficients that can be applied in a Kalman filter clock process noise model. By converting the estimated Allan deviations to time prediction errors, theoretical maximum values for receiver clock modeling can be assessed. For the used oscillators, these intervals range from eleven minutes (Jackson Labs CSAC) to 2.3 hours (SRS PRS10), provided that GPS L1 C/A-code and Doppler observations are used in GNSS PVT estimation. These values are denoted as *theoretical* because they reflect upper bounds of clock modeling due to the *stochastic* clock behavior. However,

in GNSS PVT, the *practical* modeling interval also depends on the *deterministic* clock behavior, that is time and frequency offset as well as frequency drift; higher-order effects can be safely neglected for atomic clocks. This also dictates the parametrization of the receiver clock bias to a certain extend.

In the case at hand, the idea of modeling the temporal evolution of the clock biases by means of a piecewise linear polynomial was adapted from Weinbach (2013) and transferred to a real-time applicable approach in a sequential least-squares adjustment (SLSA). Within this recursive approach, the polynomial coefficients are updated and not estimated anew with each new observation epoch. The coordinates, on the other hand, are estimated in an epochwise manner since the algorithm is designed for kinematic applications. In order to ensure continuous clock modeling, consecutive intervals are connected by constraining their slopes (frequency offsets) depending on the temporal stability of the oscillator in use. This is also necessary in case a pronounced frequency drift is present in the oscillator signal since a linear polynomial only accounts for time and frequency offsets. Furthermore, an already existing two-state clock model for use in a Kalman filter is applied using the individually determined spectral coefficients. Due to the shorter recursion length of only one epoch compared to the sequential least-squares approach, such a two-state model, again accounting for time and frequency offset, is sufficient for physically meaningful RCM.

The practical evaluation and validation of the proposed models were mainly carried out by means of a true kinematic automotive experiment, where the zero-baseline measurement configuration consisted of five identical receivers, four of them each connected to one of the previously characterized oscillators, one driven by its internal quartz oscillator. In addition, a local reference station was used to compute reference trajectories based on carrier phase observations for each test drive. Both methods of receiver clock modeling were then applied in an SPP solution using GPS and GLONASS L1 C/A-code and Doppler observations. The benefits of RCM were quantified in terms of the impact on the precision, reliability and integrity of the coordinate and velocity estimates, for both the Kalman filter model and the sequential least-squares approach. It was shown that clock modeling improves the precision of the up-coordinates by approximately 80% in case of all four oscillators, which applies to both the Kalman filter and the SLSA, where the smoothing effect of the latter was slightly more pronounced because its recursion includes more observation epochs, i.e. it has a larger memory length. On the contrary, the frequency stability provided by only two of the oscillators in use was high enough to improve the precision of the vertical velocity estimates. Although this contradicts the findings of the clock characterizations to some extent, it is assumed that some of the oscillators suffered more than the others from dynamic stress induced by vehicle vibrations during the experiment. However, in all four cases, internal reliability – computed in terms of minimal detectable biases (MDBs) – was enhanced, thus making the overall estimation process more robust, which means that the overall detectability of observation outliers is enhanced. These improvements in the MDBs ultimately led to better external reliability. In addition, receiver clock modeling improves the observation geometry by significantly reducing the vertical DOP values of the the SPP solutions. The same applies to the estimated integrity protection levels.

It was also found that the presence of a frequency drift, or more precisely, the point at which such a drift becomes significant over the course of clock modeling, can be detected by means of a hypothesis test. This enables the sequential clock modeling approach to adapt automatically to the deterministic characteristics of the oscillator in use. Within the scope of these studies, the application of a sliding window and its impact were investigated using the example of the Jackson Labs CSAC. Although such an approach shortens the clock modeling interval to the length of the window, it was shown that already a window length of 30 seconds provides virtually the same results, i.e. improvements, as much longer modeling intervals. This greatly enhances the overall real-time applicability of sequential RCM, which was validated by implementing the algorithm into a software receiver and testing it by means of a pedestrian experiment. In that case, the impact of clock modeling was comparable to the results of the automotive experiment.

The possibility or idea, respectively, of computing a navigation solution with only three satellites in view was tested and verified using the example of the automotive experiment in sequential RCM. For this purpose, three artificial partial satellite outages were generated so that only two GPS satellites and one GLONASS satellite remain visible for the receiver. Furthermore, the polynomial approach of clock modeling was extended to inter-system biases (ISBs) in this multi-GNSS application. The knowledge about the stability of the clock *and* ISBs was used to predict/compute additional observation corrections based on the latest estimated clock and ISB polynomial coefficients, respectively.

Lastly, the application of a CSAC in spoofing detection was investigated. A series of spoofing attacks was simulated using a GPS repeater, which simply replays authentic signals and thereby induces an additional delay into the signal path. This artificial delay leads to a jump in the clock bias estimates of a GNSS receiver. Such a spoofing method is also referred to as meaconing. The detection scheme consists of a Kalman filter with a clock model also used during the analysis of the automotive experiment. The filter monitors the clock time and frequency biases and checks if they deviate too much from the system model, which is mainly driven by the clock model. If the corresponding hypothesis test fails three epochs in a row, a meaconing attack is assumed to be detected. It was found that small delays of a few meters could only be detected by the receiver connected to the CSAC. In case of a second receiver driven by its internal oscillator, these clock jumps could also be attributable to the frequency instability of the oscillator according to the clock model. Thus, they were not detected by the hypothesis test.

In conclusion, the impact and benefits of receiver clock modeling when using miniature atomic clocks, primarily chip-scale atomic clocks, in GNSS navigation were investigated both theoretically and practically in various experiments including kinematic as well as static applications. Additionally, this work can also be viewed as a starting point for more in-depth studies in the field of clock modeling and, in general, the use of CSACs in GNSS-based applications.

5.2 Outlook

Despite the fact that significant improvements of clock modeling could be demonstrated under various aspects, there are still multiple open questions that give room for further research. Some of these questions already existed before the beginning of this thesis, others emerged during the course of the presented investigations. Therefore, a couple of topics shall be addressed at this point.

In this thesis, the impact of using an external, much more stable clock instead of the built-in quartz oscillator of a GNSS receiver was investigated, so to speak, at the end of the signal processing chain, that is the estimation of position, velocity and time of the receiver. Therefore, one of the next research steps should focus on the impact of a chip-scale atomic clock on signal processing right after reception. This covers the fields of down conversion of the GNSS signal from radio frequency to intermediate frequency level and analog-to-digital conversion, as well as signal acquisition and tracking (cf. section 2.1.5). Thus, two possible topics or questions, respectively, come to mind:

- Can the superior frequency stability of a CSAC be used to reduce the Doppler range of the search space and/or to prolong the integration time during signal acquisition?
- Positioning with only three satellites was analyzed in post-processing. So, how does a receiver react in real-time if truly only three satellites are available?

With regards to the performance differences between the RCM solution of the Kalman filter and the sequential approach, it would be beneficial if the Kalman filter model had a stronger smoothing effect, because the filter does not mitigate the high frequency peaks in the clock bias estimates. This could be achieved by a longer memory length of the filter, that is the clock model. More precisely, a cascaded filter would enable using different update intervals for different parameter groups, e.g. the coordinates

and clock biases. In addition, a process noise model taking into account the correlations between the clock bias and the vertical coordinate and velocity estimates is an interesting topic for future research.

Another important area that should be subject to further investigations is the sensitivity of miniature atomic clocks to external influences. At this point, vibration sensitivity is of particular interest as could be seen during the analysis of the automotive experiment, where the effects of clock modeling were different from what was expected according to the individually determined frequency stability of some of the oscillators. Although precautions were taken by placing the oscillators in a cushioned box, this kind of oscillators was not built for such dynamic applications in the first place.

The benefits of using a chip-scale atomic clock in spoofing detection were presented by means of a very simple experiment based on a static measurement setup. This should be used as an opportunity or starting point, respectively, for further studies. On the one hand, more realistic scenarios of spoofing attacks should be investigated including kinematic target receivers. On the other hand, similar to the remarks on the impact of a CSAC on signal acquisition and tracking, this approach should also be extended to spoofing detection; for example by enhancing interference mitigation techniques already existing in the receiver or by implementing new algorithms.

Bibliography

- Allan, D. W. (1966): "Statistics of Atomic Frequency Standards". *Proceedings of the IEEE* 54 (2), pp. 221–230. DOI: 10.1109/PROC.1966.4634.
- Allan, D. W. (1987): "Time and Frequency (Time-Domain) Characterization, Estimation, and Prediction of Precision Clocks and Oscillators". *IEEE Transactions on Ultrasonics, Ferroelectrics and Frequency Control* 34, pp. 647–654.
- Allan, D. W. and J. A. Barnes (1981): "A Modified "Allan Variance" with Increased Oscillator Characterization Ability". *Proceedings of the 35th Annual Frequency Control Symposium*. Philadelphia, PA, USA, pp. 470–475. DOI: 10.1109/FREQ.1981.200514.
- Allan, D. W. and H. Hellwig (1978): "Time Deviation and Time Prediction Error for Clock Specification, Characterization, and Application". *Proceedings of the IEEE Position, Location and Navigation Symposium*. San Diego, CA, USA, pp. 22–28.
- Altamimi, Z., P. Rebischung, L. Métivier, and X. Collilieux (2016): "ITRF2014: A new release of the International Terrestrial Reference Frame modeling nonlinear station motions". *Journal of Geophysical Research: Solid Earth* 121.8, pp. 6109–6131. DOI: 10.1002/2016JB013098.
- Arimondo, E. (1996): "Coherent Population Trapping in Laser Spectroscopy". *Progress in Optics*. Ed. by E. Wolf. Vol. 35. Elsevier, pp. 257–354. DOI: 10.1016/S0079-6638(08)70531-6.
- Ashby, N. (2003): "Relativity in the Global Positioning System". *Living Reviews in Relativity* 6 (1). DOI: 10.12942/lrr-2003-1.
- Baarda, W. (1967): "Statistical Concepts in Geodesy". *Publications on Geodesy*. Vol. 2. 4. Delft, The Netherlands: Netherlands Geodetic Commission.
- Baarda, W. (1968): "A Testing Procedure for Use in Geodetic Networks". *Publications on Geodesy*. Vol. 2. 5. Delft, The Netherlands: Netherlands Geodetic Commission.
- Barnes, J. A., A. R. Chi, L. S. Cutler, D. J. Healey, D. B. Leeson, T. E. McGunigal, J. A. Mullen, W. L. Smith, R. L. Sydnor, R. F. C. Vessot, and G. M. R. Winkler (1971): "Characterization of Frequency Stability". *IEEE Transactions on Instrumentation and Measurement* 20.2, pp. 105–120.
- Besson, B., M. Moutrey, S. Galliou, F. Marionnet, F. Gonzalez, P. Guillemot, R. Tjoelker, W. Diener, and A. Kirk (1999): "10 MHz Hyperstable Quartz Oscillators Performances". *Proceedings of the 1999 Joint Meeting of the European Frequency and Time Forum and the IEEE International Frequency Control Symposium*. Vol. 1, pp. 326–330. DOI: 10.1109/FREQ.1999.840773.
- Bevis, M., S. Businger, T. A. Herring, C. Rocken, R. A. Anthes, and R. H. Ware (1992): "GPS Meteorology: Remote Sensing of Atmospheric Water Vapor Using the Global Positioning System". *Journal of Geophysical Research: Atmospheres* 97 (D14), pp. 15787–15801. DOI: 10.1029/92JD01517.
- Bock, H., R. Dach, A. Jäggi, and G. Beutler (2009): "High-rate GPS clock corrections from CODE: support of 1 Hz applications". *Journal of Geodesy* 83 (11), pp. 1083–1094. DOI: 10.1007/s00190-009-0326-1.
- Böhm, J., A. E. Niell, P. Tregoning, and H. Schuh (2006a): "Global Mapping Function (GMF): A new empirical mapping function based on numerical weather model data". *Geophysical Research Letters* 33 (7). DOI: 10.1029/2005GL025546.
- Böhm, J., B. Werl, and H. Schuh (2006b): "Troposphere mapping functions for GPS and very long baseline interferometry from European Centre for Medium-Range Weather Forecasts operational analysis data". *Journal of Geophysical Research: Solid Earth* 111 (B2). DOI: 10.1029/2005JB003629.
- Böhm, J., R. Heinkelmann, and H. Schuh (2007): "Short Note: A global model of pressure and temperature for geodetic applications". *Journal of Geodesy* 81 (10), pp. 679–683. DOI: 10.1007/s00190-007-0135-3.
- Brown, R. G. and P. Y. C. Hwang (1997): *Introduction to Random Signals and Applied Kalman Filtering*. 3rd edition. John Wiley & Sons.
- Brunner, F. K. and M. Gu (1991): "An improved regional ionospheric model for single-frequency GNSS users". *Manuscripta Geodaetica* 16 (3), pp. 205–214.
- Brunner, F. K., H. Hartinger, and L. Troyer (1999): "GPS signal diffraction modelling: the stochastic SIGMA- Δ model". *Journal of Geodesy* 73 (5), pp. 259–267. DOI: 10.1007/s001900050242.
- Brunner, F. K. and W. M. Welsch (1992): "Effect of the troposphere on GPS measurements". *GPS World* 4 (1).
- Bucy, R. S. and P. D. Joseph (2005): *Filtering for Stochastic Processes With Applications to Guidance*.

- American Mathematical Society Chelsea Publishing.
- Cacciapuoti, L. and C. Salomon (2011): "Atomic clock ensemble in space". *Journal of Physics: Conference Series* 327.1. DOI: 10.1088/1742-6596/327/1/012049.
- Caissy, M., L. Agrotis, G. Weber, M. Hernandez-Pajares, and U. Hugentobler (2012): "Coming Soon – The International GNSS Real-Time Service". *GPS World* 23.6. Ed. by R. B. Langley, pp. 52–58.
- Calero, D., E. Fernández, and M. E. Parés (2016): "Positioning performance of Chip-Scale Atomic Clock GNSS augmentation systems". *Proceedings of the 8th ESA Workshop on Satellite Navigation Technologies and European Workshop on GNSS Signals and Signal Processing (NAVITEC)*. Noordwijk, The Netherlands. DOI: 10.1109/NAVITEC.2016.7849326.
- Chatre, E. (2017): "Galileo Programme Status Update". *Proceedings of the 30th International Technical Meeting of the Satellite Division of The Institute of Navigation (ION GNSS+ 2017)*. Portland, OR, USA, pp. 843–864.
- Dach, R., G. Beutler, U. Hugentobler, S. Schaer, T. Schildknecht, T. Springer, G. Dudle, and L. Prost (2003): "Time transfer using GPS carrier phase: error propagation and results". *Journal of Geodesy* 77 (1-2), pp. 1–14. DOI: 10.1007/s00190-002-0296-z.
- Dach, R., S. Lutz, P. Walser, and P. Fridez, eds. (2015): *Bernese GPS Software Version 5.2*. Astronomical Institute, University of Bern.
- Dierendonck, A. J. van, J. B. McGraw, and R. G. Brown (1984): "Relationship Between Allan Variances and Kalman Filter Parameters". *Proceedings of the 16th Precise Time and Time Interval (PTTI) Applications and Planning Meeting*. Greenbelt, MD, USA, pp. 273–292.
- Dow, J. M., R. E. Neilan, and C. Rizos (2009): "The International GNSS Service in a changing landscape of Global Navigation Satellite Systems". *Journal of Geodesy* 83 (3-4), pp. 191–198. DOI: 10.1007/s00190-008-0300-3.
- Einstein, A. (1905a): "Ist die Trägheit eines Körpers von seinem Energieinhalt abhängig?" *Annalen der Physik* 323 (13), pp. 639–641.
- Einstein, A. (1905b): "Zur Elektrodynamik bewegter Körper". *Annalen der Physik* 322 (10), pp. 891–921.
- Einstein, A. (1916): "Die Grundlage der allgemeinen Relativitätstheorie". *Annalen der Physik* 354 (7), pp. 769–822.
- ESOC (2018): *IGS Analysis Strategy*. URL: <http://dgnl7.esoc.esa.int/products/gnss-products/esa.acn> (visited on 04/10/2018).
- European Commission (1999): "Galileo - Involving Europe in a New Generation of Satellite Navigation Services". *COM 54 final*. URL: <http://eur-lex.europa.eu/legal-content/EN/TXT/PDF/?uri=CELEX:51999DC0054&from=EN> (visited on 02/12/2018).
- European Union (2016): *Galileo Open Service Signal In Space Interface Control Document*. URL: https://www.gsc-europa.eu/system/files/galileo_documents/Galileo-OS-SIS-ICD.pdf (visited on 02/19/2018).
- Farrell, J. A. (2008): *Aided Navigation: GPS with High Rate Sensors*. McGraw-Hill Education.
- Felli, M. and R. E. Spencer, eds. (1989): *Very Long Baseline Interferometry. Techniques and Applications*. NATO Science Series C: Mathematical and Physical Sciences, Vol. 283. Kluwer Academic Publishers. DOI: 10.1007/978-94-009-2428-4.
- Fernández, E., D. Calero, and M. E. Parés (2017a): "A Study on PPP Clock Augmentation Using a CSAC". *Proceedings of the 6th Galileo Science Colloquium*. Valencia, Spain.
- Fernández, E., D. Calero, and M. E. Parés (2017b): "CSAC Characterization and Its Impact on GNSS Clock Augmentation Performance". *Sensors* 17.2, 370. DOI: 10.3390/s17020370.
- Fonville, B., E. Powers, A. Kropp, and F. Vannicola (2007): "Evaluation of Carrier-phase GNSS Timing Receivers for UTC/TAI Applications". *Proceedings of the 39th Precise Time and Time Interval (PTTI) Meeting*. Long Beach, CA, USA, pp. 331–338.
- Funcke, G. (1982): "Verfahren zur Parameterelimination im Gauß-Markoff-Modell und deren Einfluß auf ausgeglichene Beobachtungen". *Allgemeine Vermessungsnachrichten* 89, pp. 112–122.
- Günther, C. (2014): "A Survey of Spoofing and Counter-Measures". *NAVIGATION: Journal of The Institute of Navigation* 61.3, pp. 159–177.
- Gardner, A. T. and J. A. Collins (2012): "Advancements in High-Performance Timing for Long Term Underwater Experiments. A Comparison of Chip Scale Atomic Clocks to Traditional Microprocessor-Compensated Crystal Oscillators". *Proceedings of the 2012 Oceans Conference*. Hampton Roads, VA, USA. DOI: 10.1109/OCEANS.2012.6404847.
- Gelb, A., J. F. Kasper, R. A. Nash, C. F. Price, and A. A. Sutherland (1974): *Applied Optimal Estimation*. Ed. by A. Gelb. The M.I.T. Press.
- Gioia, C. and D. Borio (2016): "A statistical characterization of the Galileo-to-GPS inter-system bias". *Journal of Geodesy* 90 (11), pp. 1279–1291. DOI: 10.1007/s00190-016-0925-6.
- Gleason, S. and D. Gebre-Egziabher, eds. (2009): *GNSS Applications and Methods*. Artech House.

- Gleason, S., S. Hodgart, Y. Sun, C. Gommenginger, S. Mackin, M. Adjrad, and M. Unwin (2005): "Detection and Processing of Bistatically Reflected GPS Signals from Low Earth Orbit for the Purpose of Ocean Remote Sensing". *IEEE Transactions on Geoscience and Remote Sensing* 43 (6), pp. 1229–1241. DOI: 10.1109/TGRS.2005.845643.
- GPS Directorate (2006): *Interface Specification IS-GPS-200D*. URL: <https://www.gps.gov/technical/icwg/IS-GPS-200D.pdf> (visited on 04/10/2018).
- GPS Directorate (2013): *Interface Specification IS-GPS-200H*. URL: <https://www.gps.gov/technical/icwg/IS-GPS-200H.pdf> (visited on 04/10/2018).
- GPS World (2018): *Harris Corporation delivers fifth GPS III satellite navigation payload*. URL: <http://gpsworld.com/harris-corporation-delivers-fifth-gps-iii-satellite-navigation-payload/> (visited on 06/14/2018).
- GPS.gov (2018): *GPS: The Global Positioning System*. URL: <https://www.gps.gov/> (visited on 02/08/2018).
- GSC (2018): *European GNSS Service Centre*. URL: <https://www.gsc-europa.eu/> (visited on 03/13/2018).
- Gurtner, W. and L. Estey (2007): *The Receiver Independent Exchange Format. Version 3.00*. URL: <ftp://igs.org/pub/data/format/rinex300.pdf> (visited on 04/12/2018).
- Hamming, R. W. (1983): *Digital Filters*. 3rd edition. Mineola, NY, USA: Dover Publications, Inc.
- Heavner, T. P., E. A. Donley, F. Levi, G. Costanzo, T. E. Parker, J. H. Shirley, N. Ashby, S. Barlow, and S. R. Jefferts (2014): "First accuracy evaluation of NIST-F2". *Metrologia* 51.3, pp. 174–182. DOI: 10.1088/0026-1394/51/3/174.
- Heck, B. (1975): "Die Genauigkeit eliminiertes unbekanntes bei regulären und singulären Ausgleichungsproblemen". *Allgemeine Vermessungsnachrichten* 82, pp. 345–348.
- Hernández, I. E., I. Rodríguez, G. Tobías, J. D. Calle, E. Carbonell, G. Seco-Granados, J. Simón, and R. Blasi (2015): "Testing GNSS High Accuracy and Authentication - Galileo's Commercial Service". *Inside GNSS* 10, pp. 38–48.
- Hernández-Pajares, M., J. M. Juan, and J. Sanz (1999): "New approaches in global ionospheric determination using ground GPS data". *Journal of Atmospheric and Solar-Terrestrial Physics* 61 (16), pp. 1237–1247. DOI: 10.1016/S1364-6826(99)00054-1.
- Hofmann-Wellenhof, B., H. Lichtenegger, and E. Wasle (2008): *GNSS – Global Navigation Satellite Systems. GPS, GLONASS, Galileo, and more*. Vienna: Springer. DOI: 10.1007/978-3-211-73017-1.
- Howe, D. A., D. W. Allan, and J. A. Barnes (1981): "Properties of Signal Sources and Measurement Methods". *Proceedings of the 35th Annual Frequency Control Symposium*, pp. 669–716. DOI: 10.1109/FREQ.1981.200541.
- Huntemann, N., C. Sanner, B. Lipphardt, C. Tamm, and E. Peik (2016): "Single-Ion Atomic Clock with 3×10^{-18} Systematic Uncertainty". *Physical Review Letters* 116 (6). DOI: 10.1103/PhysRevLett.116.063001.
- ICAO (2006): *Convention on International Civil Aviation. Annex 10: Aeronautical Telecommunications. Volume I: Radio Navigation Aids*. 6th edition. URL: https://www.baf.bund.de/SharedDocs/Downloads/DE/ICAO_Docs/ICAO_Annex10.pdf?__blob=publicationFile&v=2 (visited on 04/24/2018).
- Ido, T. (2012): "Optical Lattice Clock". *MAPAN – Journal of Metrology Society of India* 27 (1), pp. 9–12. DOI: 10.1007/s12647-012-0008-y.
- IfEN GmbH (2017): *SX3 Navigation Software Receiver. User Manual, Version: 3.3*. Artech House.
- IGS (2018): *International GNSS Service Products*. URL: <http://www.igs.org/products> (visited on 02/23/2018).
- ITU (1997): *Handbook: Selection and Use of Precise Frequency and Time Systems*. Ed. by R. L. Sydner and D. W. Allan. Geneva, Switzerland: Radiocommunication Bureau of the International Telecommunication Union (ITU-R). DOI: 11.1002/pub/800c94a6-en.
- Jackson Labs (2018): *LN CSAC Datasheet*. URL: http://www.jackson-labs.com/assets/uploads/main/LN_CSAC_specs.pdf (visited on 03/19/2018).
- Jafarnia-Jahromi, A., S. Daneshmand, A. Broumandan, J. Nielsen, and G. Lachapelle (2013): "PVT Solution Authentication Based on Monitoring the Clock State for a Moving GNSS Receiver". *Proceedings of European Navigation Conference (ENC2013)*. Vienna, Austria.
- JAVAD GNSS (2018): *TRE-G3T Datasheet*. URL: http://www.javad.com/downloads/javadgnss/sheets/TRE-G3T_Datasheet.pdf (visited on 03/15/2018).
- Kaiser, J. F. (1974): "Nonrecursive Digital Filter Design Using the I_0 -Sinh Window Function". *Proceedings of the IEEE International Symposium on Circuits and Systems*, pp. 20–23.
- Kalman, R. E. (1960): "A New Approach to Linear Filtering and Prediction Problems". *Journal of Basic Engineering* 82 (1), pp. 35–45. DOI: 10.1115/1.3662552.
- Karutin, S. (2016): "GLONASS Programme Update". *Proceedings of the 29th International Technical Meeting of the Satellite Division of The Institute of*

- Navigation (ION GNSS+ 2016)*. Portland, OR, USA, pp. 2376–2390.
- Kibe, S. V., K. A. Shridhara, and M. M. Jayalalitha (1996): “Software-based GIC/GNSS Compatible GPS Receiver Architecture Using TMS320C30 DSP Processor”. *Proceedings of the 5th International Conference on Satellite Systems for Mobile Communications and Navigation*, pp. 36–39. DOI: 10.1049/cp:19960403.
- Kitching, J., S. Knappe, and L. Hollberg (2002): “Miniature vapor-cell atomic-frequency references”. *Applied Physics Letters* 81.553 (3). DOI: 10.1063/1.1494115.
- Kjørsvik, N. S. and E. Brøste (2009): *Using TerraPOS for efficient and accurate marine positioning*. White paper. Lysaker, Norway: TerraTec AS. URL: <https://www.terratec.no/filarkiv/File/terrapos-whitepaper-2009.pdf> (visited on 05/03/2018).
- Kleusberg, A. and P. J. G. Teunissen, eds. (1996): *GPS for Geodesy*. Springer Berlin Heidelberg.
- Klobuchar, J. A. (1987): “Ionospheric Time-Delay Algorithms for Single-Frequency GPS Users”. *IEEE Transactions on Aerospace and Electronic Systems*. Vol. 23. 3, pp. 325–331.
- Knable, N. and R. M. Kalafus (1984): “Clock Coasting and Altimeter Error Analysis for GPS”. *NAVIGATION: Journal of The Institute of Navigation* 31.4, pp. 289–302. DOI: 10.1002/j.2161-4296.1984.tb00880.x.
- Knappe, S., V. Shah, P. D. D. Schwindt, L. Hollberg, J. Kitching, L.-A. Liew, and J. Moreland (2004): “A microfabricated atomic clock”. *Applied Physics Letters* 85.1460 (9). DOI: 10.1063/1.1787942.
- Koch, K.-R. (1999): *Parameter Estimation and Hypothesis Testing in Linear Models*. 2nd, updated and enlarged edition. Berlin, Heidelberg: Springer. DOI: 10.1007/978-3-662-03976-2.
- Kouba, J. (2004): “Improved relativistic transformations in GPS”. *GPS Solutions* 8 (3), pp. 170–180. DOI: 10.1007/s10291-004-0102-x.
- Krawinkel, T. and S. Schön (2014): “Application of Miniaturized Atomic Clocks in Kinematic GNSS Single Point Positioning”. *Proceedings of the 28th European Frequency and Time Forum (EFTF)*. Neuchatel, CH, pp. 97–100.
- Krawinkel, T. and S. Schön (2015): “Benefits of Chip Scale Atomic Clocks in GNSS Applications”. *Proceedings of the 28th International Technical Meeting of the Satellite Division of The Institute of Navigation (ION GNSS+ 2015)*. Tampa, FL, USA, pp. 2867–2874.
- Krawinkel, T. and S. Schön (2016a): “Benefits of receiver clock modeling in code-based GNSS navigation”. *GPS Solutions* 20 (4), pp. 687–701. DOI: 10.1007/s10291-015-0480-2.
- Krawinkel, T. and S. Schön (2016b): “Enhanced Multi-GNSS PVT Solution When Using Chip Scale Atomic Clocks”. *Proceedings of the 29th International Technical Meeting of the Satellite Division of The Institute of Navigation (ION GNSS+ 2016)*. Portland, OR, USA, pp. 200–208.
- Krawinkel, T. and S. Schön (2016c): “On the Impact of Chip Scale Atomic Clocks on GNSS Signal Processing and Multi-GNSS Navigation”. *Proceedings of the 8th ESA Workshop on Satellite Navigation Technologies and European Workshop on GNSS Signals and Signal Processing (NAVITEC)*. Noordwijk, The Netherlands.
- Kuang, D., B. E. Schutz, and M. M. Watkins (1996): “On the structure of geometric positioning information in GPS measurements”. *Journal of Geodesy* 71 (1), pp. 35–43. DOI: 10.1007/s001900050073.
- Larson, K. M., E. E. Small, E. Gutmann, A. Bilich, P. Axelrad, and J. Braun (2008): “Using GPS multipath to measure soil moisture fluctuations: initial results”. *GPS Solutions* 12 (3), pp. 173–177. DOI: 10.1007/s10291-007-0076-6.
- Laurichesse, D., F. Mercier, J.-P. Berthias, P. Broca, and L. Cerri (2009): “Integer Ambiguity Resolution on Undifferenced GPS Phase Measurements and Its Application to PPP and Satellite Precise Orbit Determination”. *NAVIGATION: Journal of The Institute of Navigation* 56.2, pp. 135–149.
- Lichten, S. M. and J. S. Border (1987): “Strategies for High-Precision Global Positioning System Orbit Determination”. *Journal of Geophysical Research* 92.B12, pp. 751–762.
- Lutwak, R. (2011): “Principles of Atomic Clocks”. Tutorial. *Joint Conference of the IEEE International Frequency Control and the European Frequency and Time Forum (FCS)*. San Francisco, CA, USA. URL: <https://ieeefcc.org/download/principles-of-atomic-clocks/> (visited on 03/12/2018).
- Ma, L., Z. You, T. Liu, and S. Shi (2016): “Coupled Integration of CSAC, MIMU, and GNSS for Improved PNT Performance”. *Sensors* 16.5. DOI: 10.3390/s16050682.
- March, R. E. (1997): “An Introduction to Quadrupole Ion Trap Mass Spectrometry”. *Journal of Mass Spectrometry* 32 (4), pp. 351–369. DOI: 10.1002/(SICI)1096-9888(199704)32:4<351::AID-JMS512>3.0.CO;2-Y.
- Marnach, D., S. Mauw, M. Martins, and C. Harpes (2013): “Detecting Meaconing Attacks by Analysing the Clock Bias of GNSS Receivers”. *Artificial Satellites* 48.2, pp. 63–83.

- Maybeck, P. S. (1982): *Stochastic models, estimation, and control. Volume 2*. Ed. by R. Bellman. Mathematics in Science and Engineering, Vol. 141-2. Academic Press.
- McDowell, C. E. (2007): "GPS spoofer and repeater mitigation system using digital spatial nulling". Pat. US 7250903 B1.
- Melbourne, W. G. (1985): "The Case for Ranging in GPS-based Geodetic Systems". *Proceedings of the First International Symposium on Precise Positioning with the Global Positioning System*. Ed. by C. Goad. Rockville, MD, USA, pp. 373–386.
- Meynadier, F., P. Delva, C. le Poncin-Lafitte, C. Guerlin, and P. Wolf (2018): "Atomic clock ensemble in space (ACES) data analysis". *Classical and Quantum Gravity* 35.3. DOI: 10.1088/1361-6382/aaa279.
- Microsemi (2018a): *5071A Datasheet*. URL: https://www.microsemi.com/document-portal/doc_download/133269-5071a-datasheet (visited on 03/08/2018).
- Microsemi (2018b): *SA.45s CSAC Datasheet*. URL: https://www.microsemi.com/document-portal/doc_download/133305-sa-45s-csac-datasheet (visited on 03/08/2018).
- Microsemi (2018c): *White Paper: Thermally-Improved Microsemi Chip Scale Atomic Clock*. URL: https://www.microsemi.com/document-portal/doc_download/137721-csac-thermally-improved (visited on 04/06/2018).
- Misra, P. (1996): "The role of the clock in a GPS receiver". *GPS World* 7.4, pp. 60–66.
- Misra, P. and P. Enge (2011): *Global Positioning System: Signals, Measurements, and Performance*. Revised second edition. Ganga-Jamuna Press.
- Montenbruck, O. and A. Hauschild (2013): "Code Biases in Multi-GNSS Point Positioning". *Proceedings of the International Technical Meeting (ITM) of The Institute of Navigation*. San Diego, CA, USA, pp. 616–628.
- Montenbruck, O., E. Gill, and R. Kroes (2005): "Rapid orbit determination of LEO satellites using IGS clock and ephemeris products". *GPS Solutions* 9 (3), pp. 226–235. DOI: 10.1007/s10291-005-0131-0.
- Montenbruck, O., A. Hauschild, and P. Steigenberger (2014): "Differential Code Bias Estimation using Multi-GNSS Observations and Global Ionosphere Maps". *NAVIGATION: Journal of The Institute of Navigation* 61 (3). DOI: 10.1002/navi.64.
- Montenbruck, O., P. Steigenberger, L. Prange, Z. Deng, Q. Zhao, F. Perosanz, I. Romero, C. Noll, A. Stürze, G. Weber, R. Schmid, K. MacLeod, and S. Schaer (2017): "The Multi-GNSS Experiment (MGEX) of the International GNSS Service (IGS) - Achievements, prospects and challenges". *Advances in Space Research* 59 (7), pp. 1671–1697. DOI: 10.1016/j.asr.2017.01.011.
- Montgomery, P., T. Humphreys, and B. Ledvina (2009): "A Multi-Antenna Defense – Receiver Autonomous GPS Spoofing Detection". *Inside GNSS, March/April 2009*, pp. 40–46.
- Murphy, J. and T. Skidmore (1994): "A Low-Cost Atomic Clock: Impact on the National Airspace and GNSS Availability". *Proceedings of the 7th International Technical Meeting of the Satellite Division of The Institute of Navigation (ION GPS 1994)*. Salt Lake City, UT, USA.
- Nicholson, T. L., S. L. Campbell, R. B. Hutson, G. E. Marti, B. J. Bloom, R. L. McNally, W. Zhang, M. D. Barrett, M. S. Safronova, G. F. Strouse, W. L. Tew, and J. Ye (2015): "Systematic evaluation of an atomic clock at 2×10^{-18} total uncertainty". *Nature Communications* 6. DOI: 10.1038/ncomms7896.
- Niell, A. E. (1996): "Global mapping functions for the atmosphere delay at radio wavelengths". *Journal of Geophysical Research* 101 (B2), pp. 3227–3246.
- Niemeier, W. (2008): *Ausgleichsrechnung. Statistische Auswertemethoden. 2., überarbeitete und erweiterte Auflage*. Berlin, New York: Walter de Gruyter.
- Odiijk, D. (2003): "Ionosphere-Free Phase Combinations for Modernized GPS". *Journal of Surveying Engineering* 129 (4), pp. 165–173.
- Orliac, E., R. Dach, K. Wang, M. Meindl, M. Rothacher, T. Romanyuk, U. Hugentobler, E. Schönemann, and W. Enderle (2016): "ESA Project on Improving GNSS-Based Precise Orbit Determination by Using Highly Accurate Clocks". *International GNSS Service (IGS) Workshop*. Sydney, Australia. URL: <http://www.igs.org/assets/pdf/W2016%20-%20PS1304%20-%20Orliac.pdf> (visited on 02/08/2018).
- Pany, T. (2010): *Navigation Signal Processing for GNSS Software Receivers*. Artech House.
- Paul, W. and H. Steinwedel (1956): "Verfahren zur Trennung bzw. zum getrennten Nachweis von Ionen verschiedener spezifischer Ladung". Pat. DE944900 (C).
- Peil, S., J. Hanssen, T. B. Swanson, J. Taylor, and C. R. Ekstrom (2016): "The USNO rubidium fountains". *Journal of Physics: Conference Series* 723.1. DOI: 10.1088/1742-6596/723/1/012004.
- Percival, D. B. (2003): "Stochastic models and statistical analysis for clock noise". *Metrologia* 40.3, pp. 289–304. DOI: 10.1088/0026-1394/40/3/308.
- Petit, G. and B. Luzum, eds. (2010): *IERS Conventions (2010). IERS Technical Note No. 36*. Frankfurt am Main: Verlag des Bundesamts für Kartographie und Geodäsie.

- Ramlall, R., J. Streeter, and J. F. Schnecker (2011): "Three Satellite Navigation in an Urban Canyon using a Chip-Scale Atomic Clock". *Proceedings of the 24th International Technical Meeting of the Satellite Division of The Institute of Navigation (ION GNSS 2011)*. Portland, OR, USA, pp. 2937–2945.
- Ray, J. and K. Senior (2005): "Geodetic techniques for time and frequency comparisons using GPS phase and code measurements". *Metrologia* 42.4, pp. 215–232. DOI: 10.1088/0026-1394/42/4/005.
- Riehle, F. (2004): *Frequency Standards. Basics and Applications*. Weinheim: Wiley-VCH.
- Ries, L., F. Legrand, L. Lestarquit, W. Vigneau, and J.-L. Issler (2003): "Tracking and Multipath Performance Assessments of BOC Signals Using a Bit-Level Signal Processing Simulator". *Proceedings of the 16th International Technical Meeting of the Satellite Division of The Institute of Navigation (ION GPS/GNSS 2003)*. Portland, OR, USA, pp. 1996–2010.
- Riley, W. J. and C. A. Greenhall (2004): "Power Law Noise Identification Using the Lag 1 Autocorrelation". *Proceedings of the 28th European Frequency and Time Forum (EFTF)*, pp. 576–580. DOI: 10.1049/cp:20040932.
- Riley, W. J. (2008): *Handbook of Frequency Stability Analysis*. Special Publication (NIST SP) 1065. U.S. Department of Commerce, National Institute of Standards and Technology. URL: http://ws680.nist.gov/publication/get_pdf.cfm?pub_id=50505 (visited on 02/07/2018).
- Rothacher, M. and G. Beutler (1998): "The Role of GPS in the Study of Global Change". *Physics and Chemistry of the Earth* 23.9–10, pp. 1029–1040.
- Rothacher, M. and R. Schmid (2010): *ANTEX: The Antenna Exchange Format, Version 1.4*. URL: <ftp://igs.org/pub/station/general/antex14.txt> (visited on 04/11/2018).
- Rutman, J. (1978): "Characterization of Phase and Frequency Instabilities in Precision Frequency Sources: Fifteen Years of Progress". *Proceedings of the IEEE*. Vol. 66. 9, pp. 1048–1075.
- Saastamoinen, J. (1973): "Contributions to the Theory of Atmospheric Refraction". *Bulletin Géodésique* 107.1, pp. 13–34. DOI: 10.1007/BF02521844.
- Salzmann, M. (1991): "MDB: A Design Tool for Integrated Navigation Systems". *Kinematic Systems in Geodesy, Surveying, and Remote Sensing*. Ed. by K.-P. Schwarz and G. Lachapelle. International Association of Geodesy Symposia, Vol. 107. Springer New York, pp. 218–227.
- Salzmann, M. (1993): *Least Squares Filtering and Testing for Geodetic Navigation Applications*. Publications on Geodesy, New Series 37. Netherlands Geodetic Commission.
- Santerre, R., A. Geiger, and S. Banville (2017): "Geometry of GPS dilution of precision: revisited". *GPS Solutions* 21 (4), pp. 1747–1763. DOI: 10.1007/s10291-017-0649-y.
- Schaer, S., W. Gurtner, and J. Feltens (1998): "IONEX: The IONosphere Map EXchange Format Version 1". *Proceedings of the IGS Analysis Center Workshop*, pp. 233–247. URL: <ftp://igs.org/pub/data/format/ionex1.pdf> (visited on 04/12/2018).
- Seeber, G. (2003): *Satellite Geodesy*. 2nd completely revised and extended edition. Berlin, New York: Walter de Gruyter.
- Sesia, I. and P. Tavella (2008): "Estimating the Allan variance in the presence of long periods of missing data and outliers". *Metrologia* 45.6, pp. 134–142.
- SRS (2018a): *FS725 Datasheet*. URL: <http://www.thinksrs.com/downloads/PDFs/Catalog/FS725c.pdf> (visited on 03/08/2018).
- SRS (2018b): *PRS10 Datasheet*. URL: <http://www.thinksrs.com/downloads/PDFs/Catalog/PRS10c.pdf> (visited on 03/19/2018).
- Steeb, W.-H. (1991): *Kronecker Product of Matrices and Applications*. B.I. Wissenschaftsverlag.
- Steigenberger, P. and O. Montenbruck (2017): "Galileo status: orbits, clocks, and positioning". *GPS Solutions* 21 (2), pp. 319–331. DOI: 10.1007/s10291-016-0566-5.
- Steindl, E., W. Dunkel, A. Hornbostel, C. Hättich, and P. Remi (2013): "The impact of interference caused by GPS Repeaters on GNSS receivers and services". *Proceedings of the European Navigation Conference (ENC)*. Vienna, Austria.
- Sturza, M. A. (1983): "GPS Navigation Using Three Satellites and a Precise Clock". *NAVIGATION: Journal of The Institute of Navigation* 30.2, pp. 146–156. DOI: 10.1002/j.2161-4296.1983.tb00831.x.
- Susnik, A., R. Dach, K. Wang, M. Meindl, M. Rothacher, D. Koch, T. Romanyuk, I. Selmke, U. Hugentobler, E. Schönemann, and W. Enderle (2017): "Improved GNSS-Based Precise Orbit Determination by using highly accurate clocks". *IGS Workshop*. Paris, France.
- Terrien, J. (1968): "News from the International Bureau of Weights and Measures". *Metrologia* 4.1, pp. 41–45.
- Teunissen, P. J. G. (1990): "Quality Control in Integrated Navigation Systems". *IEEE Aerospace and Electronic Systems Magazine* 5 (7), pp. 35–41. DOI: 10.1109/62.134219.
- Teunissen, P. J. G. (1997): "Minimal detectable biases of GPS data". *Journal of Geodesy* 72, pp. 236–244.
- Tossaint, M., J. Samson, F. Toran, J. Ventura-Traveset, J. Sanz, M. Hernandez-Pajares, and J. Juan (2006):

- “The Stanford – ESA Integrity Diagram: Focusing on SBAS Integrity”. *Proceedings of the 19th International Technical Meeting of the Satellite Division of The Institute of Navigation (ION GNSS 2006)*. Fort Worth, TX, USA, pp. 894–905.
- Ucar, A., Y. Adane, B. Bardak, C. Paparo, R. Berry, and I. Kale (2013): “A Chip Scale Atomic Clock Driven Receiver for Multi-Constellation GNSS”. *The Journal of Navigation* 66 (3), pp. 449–464. DOI: 10.1017/S037346331300009X.
- University of Texas (2012): *Todd Humphreys' Research Team Demonstrates First Successful GPS Spoofing of UAV*. URL: <http://www.ae.utexas.edu/news/504-todd-humphreys-research-team-demonstrates-first-successful-uav-spoofing> (visited on 05/11/2018).
- University of Texas (2013): *Spoofing a Superyacht at Sea*. URL: <https://news.utexas.edu/2013/07/30/spoofing-a-superyacht-at-sea> (visited on 05/11/2018).
- Vectron (2018): *MX-060 Datasheet*. URL: <https://www.vectron.com/products/ocxo/mx-060.pdf> (visited on 03/08/2018).
- Volpe, J. A. (2001): *Vulnerability Assessment for the Transportation Infrastructure Relying on the Global Positioning System*. Final report. National Transportation Systems Center.
- Vremya-CH (2018a): *VCH-1003A*. URL: <https://www.vremya-ch.com/english/product/indexd57c.html?Razdel=9&Id=47> (visited on 03/08/2018).
- Vremya-CH (2018b): *VCH-1008*. URL: <https://www.vremya-ch.com/english/product/indexbf96.html?Razdel=13&Id=42> (visited on 03/08/2018).
- Wang, K. (2016): “Advanced Modeling and Algorithms for High-Precision GNSS Analysis”. PhD thesis. ETH Zürich. DOI: 10.3929/ethz-a-010610972.
- Wang, K. and M. Rothacher (2013): “Stochastic modeling of high-stability ground clocks in GPS analysis”. *Journal of Geodesy* 87 (5), pp. 427–437. DOI: 10.1007/s00190-013-0616-5.
- Wang, K., M. Rothacher, M. Meindl, E. Schönemann, and W. Enderle (2017): “Improvement in the estimation of troposphere zenith delays using high-accuracy clocks”. *IGS Workshop*. Paris, France.
- Wang, N., Y. Yuan, Z. Li, O. Montenbruck, and B. Tan (2016): “Determination of differential code biases with multi-GNSS observations”. *Journal of Geodesy* 90 (3), pp. 209–228. DOI: 10.1007/s00190-015-0867-4.
- Ward, P. W., J. W. Betz, and C. J. Hegarty (2006): “Satellite Signal Acquisition, Tracking, and Data Demodulation”. *Understanding GPS: Principles and Applications*. Ed. by E. D. Kaplan and C. J. Hegarty. 2nd edition. Artech House.
- Weinbach, U. (2013): “Feasibility and impact of receiver clock modeling in precise GPS data analysis”. PhD thesis. Leibniz Universität Hannover.
- Weinbach, U. and S. Schön (2011): “GNSS receiver clock modeling when using high-precision oscillators and its impact on PPP”. *Advances in Space Research* 47, pp. 229–238. DOI: 10.1016/j.asr.2010.06.031.
- Weinbach, U. and S. Schön (2013): “Improved GRACE kinematic orbit determination using GPS receiver clock modeling”. *GPS Solutions* 17 (4), pp. 511–520. DOI: 10.1007/s10291-012-0297-1.
- Weinbach, U. and S. Schön (2015): “Improved GPS-based coseismic displacement monitoring using high-precision oscillators”. *Geophysical Research Letters* 42, pp. 3773–3779. DOI: 10.1002/2015GL063632.
- Welch, P. D. (1967): “The Use of Fast Fourier Transform for the Estimation of Power Spectra: A Method Based on Time Averaging Over Short, Modified Periodograms”. *IEEE Transactions on Audio and Electroacoustics* 15.2, pp. 70–73. DOI: 10.1109/TAU.1967.1161901.
- Wübbena, G. (1985): “Software Developments for Geodetic Positioning with GPS Using TI 4100 Code and Carrier Measurements”. *Proceedings of the First International Symposium on Precise Positioning with the Global Positioning System*. Ed. by C. Goad. Rockville, MD, USA, pp. 403–412.
- Wübbena, G. (1991): “Zur Modellierung von GPS-Beobachtungen für die hochgenaue Positionsbestimmung”. PhD thesis. Leibniz Universität Hannover.
- Zhang, V. and M. Lombardi (2010): “Evaluation of a GPS Receiver for Code and Carrier-Phase Time and Frequency Transfer”. *Proceedings of the 42nd Precise Time and Time Interval (PTTI) Meeting*, pp. 275–283.
- Zumberge, J. F., M. B. Heflin, D. C. Jefferson, M. M. Watkins, and F. H. Webb (1997): “Precise point positioning for the efficient and robust analysis of GPS data from large networks”. *Journal of Geophysical Research* 102, pp. 5005–5017.

Acknowledgments

This thesis was developed during my employment at the Institut für Erdmessung (IfE) at Leibniz Universität Hannover. During that time, a lot of people have contributed to this work.

First of all, I would like to thank Prof. Dr.-Ing. Steffen Schön. Without his efforts to attract funding for a project on the topic of receiver clock modeling in GNSS navigation, this thesis would not have been possible. Moreover, I am grateful for the constant support and casting seeds of new ideas whenever they were needed, but also giving me the freedom to work on this thesis by keeping me free of any major obligations in the last couple months of writing. With that being said, I also thank my two co-reviewers, Prof. Dr. phil. nat. Urs Hugentobler and Prof. Dr.-Ing. Ingo Neumann for taking the time as well as providing critical feedback on this work and giving valuable causes for thought.

Furthermore, I would like to thank my colleagues at IfE for their help and support during my time at the institute so far. Special thanks go to Dr.-Ing. Tobias Kersten for his helpful advice on how to write a PhD thesis.

Further important contributors to this thesis are Dr. Andreas Bauch and his colleagues at PTB. Their help and support during the preparation, execution and analysis of the clock comparisons is very much appreciated.

Since a major part of the work on this thesis was carried out within the scope of a project named "Verbesserte Positionierung und Navigation durch Uhrmodellierung" funded by the Federal Ministry of Economics and Technology (BMWi), also many thanks go out to the responsible people at BMWi and DLR.

Last but not least, I would like to thank my family for supporting me mentally and financially without asking from the day I decided to start studying back in 2007. I will always be grateful for that.

Zuletzt möchte ich mich bei meiner Familie bedanken, die mich über all die Jahre ohne Wenn und Aber sowohl mental als auch finanziell unterstützt hat. Insbesondere nachdem ich mich im Jahr 2007 dazu entschlossen hatte, das in meiner Berufsausbildung zum Vermessungstechniker gewonnene Wissen durch ein Studium weiter zu vertiefen. Danke für alles.

Curriculum Vitae

Personal Information

Name Thomas Krawinkel
Date of Birth April 14, 1983
Place of Birth Bad Driburg, Germany

Course of Education

08/1989 – 07/1993 Elementary school
08/1993 – 06/2002 High school
07/2002 – 03/2003 Obligatory military service
08/2003 – 06/2006 Vocational training: *Surveying Technician*
10/2007 – 10/2012 Study of Geodesy and Geoinformatics at Leibniz Universität Hannover:
Bachelor of Science (2010), Master of Science (2012)

Work Experience

07/2006 – 06/2007 *Surveying Technician*, Amt für Agrarordnung, Warburg
since 11/2012 *Research Assistant*, Institut für Erdmessung, Leibniz Universität Hannover

